Kodak Color Control Patches
Blue
Cyan
Green
Yellow
Red
Magenta
White
3/Color
Black
Kodak Gray Scale
A
M
B
C
Y
M
© Kodak, 2007 TM: Kodak

Spectra and Large-scale Isotropy

学位論文

Spectra and Large-scale Isotropy of the Cosmic X-ray Background from ASCA observations

「あすか」による宇宙X線背景放射の
スペクトルと一様性の研究

平成8年3月 博士（理学）申請

東京大学　大学院　理学系研究科
物理学専攻

石崎欣尚

Spectra and Large-scale Isotropy of the Cosmic X-ray Background from ASCA observations

Yoshitaka ISHISAKI

Abstract

We have studied the average spectra of the Cosmic X-ray Background (CXB) and the field-to-field difference of the CXB spectral parameters, mainly utilizing the ASCA GIS. We created the average CXB spectrum from the ASCA Large Sky Survey (LSS) observations, which was carried out at the region around $(l, b) = (75.4°, 83.4°)$ covering the large continuous sky of $\sim 1° \times 5°$ with 76 pointings and 515 ks exposure. In the 2–10 keV energy band, the spectrum is well fitted with the power-law model ($PL^{\rm hard}$) which is almost consistent with the HEAO-1 A2. However, there exists a clear soft-excess below $\sim$ 1.2 keV, which can be fitted with the steep power-law ($PL^{\rm soft}$) of $\Gamma \sim 6$ or the 1-solar Raymod-Smith model of $kT \sim 0.3$ keV. Although this model appears to resembles the ROSAT measurements in the 0.5–1.5 keV energy band when unfolded, we cannot find the component of $\Gamma = 2.1$ which ROSAT reported. We also created the CXB spectra in 13 fields at high Galactic latitude with eliminating the discrete sources brighter than $\sim 2 \times 10^{-13}$ erg s^{-1} cm^{-2}, and fitted them with the $PL^{\rm hard} + PL^{\rm soft}$ model. The 2–10 keV fluxes of $PL^{\rm hard}$ are consistent with constant within the 90%-confidence upper-limit of 9%, while the 0.5–2 keV fluxes of $PL^{\rm soft}$, most part of which is probably the Galactic origin, vary from field to field.

CONTENTS

1 Introduction *I* - 1

1.1 The Cosmic X-ray Background (CXB) . . . *I* - 1

1.2 Problems with the CXB . . . *I* - 2

1.3 CXB investigations with ASCA . . . *I* - 3

1.4 Outline of the present thesis . . . *I* - 3

2 Review of the Cosmic X-ray Background *II* - 1

2.1 Spectral properties of the CXB . . . *II* - 1

2.1.1 CXB spectrum above 2 keV . . . *II* - 1

2.1.2 Lack of inerse-Compton effects . . . *II* - 1

2.1.3 CXB spectrum below 2 keV . . . *II* - 3

2.2 Brightness distribution of the CXB . . . *II* - 5

2.2.1 Small-scale fluctuations . . . *II* - 5

2.2.2 Global isotropy and dipole anisotropy . . . *II* - 6

2.3 Contribution of known classes of discrete sources . . . *II* - 7

2.3.1 Log$N$ - Log$S$ relations above 2 keV . . . *II* - 7

2.3.2 Log$N$ - Log$S$ relations below 2 keV . . . *II* - 7

2.3.3 The spectral paradox . . . *II* - 9

3 Instrumentation *III* - 1

3.1 The ASCA satellite . . . *III* - 1

3.1.1 Launch of the ASCA satellite . . . *III* - 1

3.1.2 Attitude control and attitude determination system . . . *III* - 3

3.1.3 Satellite operation and data transfer . . . *III* - 3

3.1.4 Early operations and observation program . . . *III* - 4

3.2 X-ray telescope (XRT) . . . *III* - 5

3.2.1 Principle of X-ray telescopes . . . *III* - 5

3.2.2 Design and structure of the XRT . . . *III* - 6

3.2.3 Alignments of four XRTs to each focal plane detector . . . *III* - 8

3.3 Solid-state Imaging Spectrometer (SIS) . . . *III* - 10

3.3.1 Design and structure of the SIS . . . *III*- 10
3.3.2 Data processing of the SIS . . . *III*- 12
3.4 Gas Imaging Spectrometer (GIS) . . . *III*- 14
3.4.1 Design and structure of the GIS . . . *III*- 14
3.4.2 Onboard data processing of the GIS . . . *III*- 18
3.4.3 Background rejection of the GIS . . . *III*- 19
3.4.4 Monitor counts and house keeping (HK) data of the GIS . . . *III*- 22
3.4.5 Basic event conversion for the GIS . . . *III*- 23

4 In Orbit Calibration of the GIS *IV* - 1
4.1 Overview . . . *IV*- 1
4.2 Response of the XRT+GIS system . . . *IV*- 1
4.2.1 Formulation of the ASCA response and an ARF builder . . . *IV*- 1
4.2.2 XRT part of ARF . . . *IV*- 5
4.2.3 GIS part of ARF . . . *IV*- 7
4.2.4 GIS part of RMF . . . *IV*- 8
4.2.5 Verification of the XRT+GIS response for a point source . . . *IV*- 11
4.3 Stray light effect to the CXB analysis . . . *IV*- 14
4.3.1 What is stray light? . . . *IV*- 14
4.3.2 Evaluation of stray light effects by ray-tracing . . . *IV*- 15
4.3.3 Comparison of ray-tracing with Crab stray obserbations . . . *IV*- 18
4.3.4 The ARF builder for the CXB spectrum . . . *IV*- 20
4.4 Residual non X-ray background (RNXB) of the GIS . . . *IV*- 22
4.4.1 Importance of RNXB in the CXB analyses . . . *IV*- 22
4.4.2 Rough properties of RNXB . . . *IV*- 22
4.4.3 Flare events and the GIS monitor counts . . . *IV*- 26
4.4.4 RNXB reproducibility by H02-sorting method . . . *IV*- 29

5 Observations *V* - 1
5.1 Selection of observed fields . . . *V*- 1
5.2 Description of Individual Fields . . . *V*- 2
5.2.1 LSS . . . *V*- 2
5.2.2 SA57 . . . *V*- 4
5.2.3 Draco Field . . . *V*- 4
5.2.4 NEP . . . *V*- 4
5.2.5 QSF3 . . . *V*- 5
5.2.6 z-system . . . *V*- 5

5.2.7 Braccesi Field . . . *V*- 5
5.2.8 Jupiter, Arp 220, and 3C368 . . . *V*- 6
5.3 Data processing . . . *V*- 6
5.3.1 Basic event selection . . . *V*- 6
5.3.2 Handling of multiple pointings . . . *V*- 7
5.3.3 Image smoothing . . . *V*- 8

6 Average CXB spectrum in the LSS field *VI* - 1
6.1 CXB data sampling and data analysis method . . . *VI*- 1
6.2 Ring-sorted CXB spectra . . . *VI*- 2
6.3 Spectral fits to the average CXB in the LSS field . . . *VI*- 4
6.3.1 Results in the 2–10 keV range . . . *VI*- 4
6.3.2 Results in the 0.6–10 keV range . . . *VI*- 6
6.4 Systematic error of the CXB spectrum . . . *VI*- 9
6.4.1 RNXB uncertainty . . . *VI*- 9
6.4.2 GIS low energy response uncertainty . . . *VI*- 10
6.4.3 XRT stray light uncertainty . . . *VI*- 11
6.4.4 XRT effective area uncertainty . . . *VI*- 12
6.4.5 Summary of the systematic errors . . . *VI*- 14

7 Field to field properties of the CXB *VII* - 1
7.1 CXB spectra of individual fields including point sources . . . *VII*- 1
7.2 How to eliminate point sources . . . *VII*- 3
7.2.1 Outline of the source-finding . . . *VII*- 3
7.2.2 Determination of the CXB base level . . . *VII*- 5
7.2.3 Point-source images . . . *VII*- 7
7.2.4 Source-masking . . . *VII*- 10
7.3 Threshold flux of the source-masks . . . *VII*- 11
7.4 CXB properties of individual fields . . . *VII*- 13
7.4.1 Strategy to study individual fields . . . *VII*- 13
7.4.2 Field-to-field variation of the CXB base level . . . *VII*- 13
7.4.3 CXB spectra of individual fields excluding point sources . . . *VII*- 15
7.4.4 Field-to-field variation of $\Gamma^{\rm hard}$ . . . *VII*- 17
7.4.5 Field-to-field variation of $F_{\rm X}^{\rm hard}$ . . . *VII*- 19
7.4.6 Effects of the soft component . . . *VII*- 23
7.5 Average CXB spectra excluding point sources . . . *VII*- 25

8 Discussion and conclusion VIII - 1
8.1 Average CXB spectrum . . . . VIII - 1
8.1.1 Summary of the observation . . . . VIII - 1
8.1.2 Comparison with previous observations . . . . VIII - 2
8.1.3 Effects of discrete sources . . . . VIII - 6
8.1.4 Constraints on the AGN mixture models of the CXB . . . . VIII - 8
8.2 Field to field fluctuation of the CXB . . . . VIII - 10
8.2.1 Summary of the observation . . . . VIII - 10
8.2.2 Comparison with previous measurements . . . . VIII - 10

A Log of the observed fields A - 1

B Contour-map images of the observed fields B - 1

C Flat field images and source-masks C - 1

D Spectra of the CXB observations D - 1

E Fitting results processed through source-masking at the threshold of 0.06 E - 1

F Hardness-map images of the observed fields F - 1

G All-sky maps of the X-ray observations G - 1

H CXB fluctuation due to unresolved sources H - 1
H.1 Formulation of the CXB fluctuation . . . . H - 1
H.2 Effective beam size for the XRT+GIS . . . . H - 2

List of Figures

2.1 The 3–50 keV CXB spectrum observed with HEAO-1 A2, adopted from Boldt (1987). The ratio (R) of the observed CXB counts to that predicted by convolving, with the detector response, power-law spectra of photon indices $\Gamma = 1.4$ (upper panel) and $\Gamma = 1.7$ (lower panel) are plotted against energy. . . . . II - 2

2.2 The 0.1–2 keV CXB spectrum observed with ROSAT PSPC, adopted from Hasinger (1992); three-component fit to the total background in the HZ43P field: a 10^6 K thermal plasma, a $2\text{–}3 \times 10^6$ K thermal plasma, and a power-law of $\Gamma \sim 2.2$ for the higher energies. . . . . II - 4

2.3 The dipole anisotropy of the CXB observed with HEAO-1 A2 all-sky survey, adopted from Boldt (1987); percentage deviations from isotropy (represented by the circle) for the average surface brightness near the ecliptic plane ($\beta = -24° \rightarrow +24°$) as a function of ecliptic longitude (λ). The 1σ error bar shown corresponds to photon counting statistics. Special directions indicated are for the CMB anisotropy results of (a) Smoot et al. (1977), (b) Cheng et al. (1979), and (c) the longitude where the supergalactic plane crosses the ecliptic equator. Surface brightness deviations for those ecliptic longitudes close to the galactic equator (i.e. near $\lambda = 89°$ and $\lambda = 269°$) are indicated with dashed lines. . . . . II - 6

2.4 The integral log N-log S relation in the 2–10 keV energy band normalized to that expected in a Euclidean universe, adopted from the review by Fabian & Barcons (1992). The filled circles are from the direct counts of Piccinotti et al. (1982). The dotted contour is the 1σ region from the HEAO-1 A2 fluctuation analysis (Shafer & Fabian 1983), the solid contour from the Ginga fluctuation analysis (Hayashida 1990). The lines marked MSS show the results from the Extended Medium Sensitivity Survey (Gioia et al. 1990) after converted into the 2–10 keV range assuming several spectral indices. The cross represents direct counts from Ginga scans (Kondo 1990). The solid line labeled XRB indicates the level at which 100% of the CXB brightness can be explained. *II*-8

2.5 The integral log N-log S relation in the 0.5–2 keV energy band, adopted from Hasinger (1992); ROSAT log N-log S relation (histogram and solid line) compared to the EMSS (two crossing solid lines) and the data of Shanks et al. (filled circles). Note that the contribution of brighter fluxes has not been added to the latter data. *II*-9

2.6 Type 2 Seyfert galaxy Mkn3 spectrum (crosses) observed with Ginga LAC, adopted from Awaki et al. (1990). The histograms show the best-fit model (absorbed power-law; $\Gamma = 1.3 \pm 0.3$, $N_{\rm H} = 6^{+3}_{-2} \times 10^{23}$ cm^{-2}, $L_{\rm X}^{2-10\,\rm keV} = 4 \times 10^{43}$ erg s^{-2} at a distance of 79 Mpc with $z = 0.0132$) and the intrinsic spectrum of Mkn3 without absorption. *II*-10

3.1 In orbit configration of the ASCA satellite *III*-2

3.2 Onboard instruments of the ASCA satellite *III*-2

3.3 Walter type I optics *III*-5

3.4 One quadrant of the ASCA XRT. The XRT is built up in four quadrants; 120 foils are ajusted by alignment bars running radially. *III*-6

3.5 Effective area of the ASCA XRT (4 XRTs summed up, on-axis) compared with that of polished mirrors used in previous missions. *III*-7

3.6 Alignment of the four focal plane detectors. Optical axes are shown by "⊙" and their positions are expressed in unit of pixel of the corresponding detectors. Detector centers are shown by "×" and their positions in reference to the center of SIS0 are given in unit of mm. Nominal positions for various observation modes (1CCD nominal, 2CCD nominal, 4CCD nominal, and SIS prior) are shown by "◇" and their positions in reference to the "Origin of Operation" are given in unit of arcmin. The gaps between the CCD chips of SIS0 and SIS1, and the support grids on the entrance windows of GIS2 and GIS3, are also superposed. *III*-9

3.7 Cross section view of the SIS camera *III*-10

3.8 (a) Detection efficiency of the SIS as a function of incoming X-ray energy. K-edges of O (0.53keV), Al (1.56keV), and Si (1.84keV) are clearly seen in the figure. This efficiency does not includes optical blocking filter. (b) Energy resolutions of the SIS as a function of incoming X-ray energy for the single event. Energy resolutions with different read-out noise N are plotted ($N \sim 5$ for the SIS). The read-out noise levels are given as the equivalent number of electrons. *III*-12

3.9 Cross section view of the GIS sensor *III*-15

3.10 Schematic view of the GIS sensor system *III*-16

3.11 Data flow chart of the GIS electronics *III*-18

3.12 (a) An example of *RAWX*-*RAWY* image of a celestial X-ray point source, obtained with GIS2 in a very early observation (in fact, this is the first light target for the GIS). No background rejection was applied, except the pulse-height UD. An event concentration near the detector rim is partly due to the background enhancement, and partly due to the position non-linearity. (b) The X-ray events contained in the image of panel (a), displayed on the plane of *PH* vs. *RT*. Two horizontal lines represent the standard onboard RTD window (RTLD–RTUD). *III*-20

3.13 (a) Almost the same as figure 3.12a except strict *RT* mask applied. A bright spot near the center is the target source, while another spot to the lower right is the ^{55}Fe calibration isotope. (b) The X-ray events contained in the image of panel (a), displayed on the plane of *PH* vs. *RTI*. *III*-20

3.14 A scatter plot of events of a blank sky displayed on the plane of squared radial distance from the center in $RAWX$-$RAWY$ image vs. SP. A nearly horizontal branch is formed by signal X-rays of the CXB, while a nearly vertical branch, which means a large scatter in the spread of UV light, originates from background near the detector wall. Two slant lines indicate the standard SPD window. III-21

3.15 X-ray images of the sunlit earth in the 1–3 keV energy band from GIS2 (panel a) and GIS3 (panel b), presented in the $RAWX$-$RAWY$ coordinates. Images are rotated and Y-fliped so that the coordinates match the direction of the $DETX$-$DETY$ coordinates. Panels (c) and (d) are the same images from GIS2 and GIS3 respectively, after converted to the $DETX$-$DETY$ coordinates. III-23

3.16 The position linearlization maps in $RAWX$-$RAWY$ coordinates for GIS2. (a) ($RAWX$, $RAWY$) to $DETX$, and (b) ($RAWX$, $RAWY$) to $DETY$. Contour levels are −22.5–25 mm in 2.5 mm step. The map versions are `xflf_s2.table` and `yflf_s2.table`. III-24

3.17 The gain maps in ($RAWX$,$RAWY$) coordinates for GIS2 (left panel) and GIS3 (right panel). Contour levels are every 10 step from 350. The gain map versions are `phfl_s2_v3.table` and `phfl_s3_v3.table` for GIS2 and GIS3, respectively. III-25

3.18 (a) Peak PH channels of the ^{55}Fe calibration isotope, plotted against the detector temperature measured in orbit on the side wall of IPMT. (b) Long-term gain history since the launch till April 1994, expressed in terms of the temperature-corrected ^{55}Fe PH. Upper and lower panels are for GIS2 and GIS3, respectively. III-25

3.19 Relative GIS gains plotted as a function of the incident source count rate ($LDHIT$). A slight gain increase is seen in high counting rates. Two lines superposed on the data points show the the best line of

$$\begin{cases} y = 0.9993 + 0.27438 \times 10^{-4} LDHIT \\ y = 1.0002 + 0.17559 \times 10^{-4} LDHIT \end{cases}$$

for GIS2 and GIS3, respectively. III-26

4.1 Properties of the XRT effective area. (a) Energy dependence at $\theta = 0$, 10, and 20 arcmin, for $\phi = 0°$. (b) θ-dependence (vignetting) at E =1, 2, 4, and 8 keV, for $\phi = 0°$ (solid lines) and 45° (dashes). The effective area shown here are based on the calibration data base file : `xrt_ea_110494.fits`. . . IV-6

4.2 Examples of the XRT PSF taken by GIS2. (a) 1.8′ offset, (b) 8′ offset, and (c) 17′ offset Cyg X-1 images (upper panels) in the 0.5 – 12 keV band and the radial profiles (lower panels) in the 1–2 keV (solid lines), 3–4 keV (dashed), 5–6 keV (dotted), and 8–12 keV (dot-dashed) energy bands. For upper panel images, contour levels are every factor of 2, and origins of the coordinates are the optical axis of GIS2. All radial profiles in lower panels are scaled so that the volume in $r \leq 6$ mm are equal to 1.0. . . . . IV-6

4.3 Energy dependence of the thermal shield transmission (thin solid line), 10.5 μm thick Be window transmission (dashed line), and total GIS quantum efficiency including thermal shield, plasma shield, Be window, and meshes (thick solid line). This plot is based on the version 4.0 GIS response. . . . IV-9

4.4 (a) Berylium thickness map for GIS2 on the detector coordinates based on the calibration data base file `s2bev1.fits`. (b) Upper panel shows a contour map of the GIS2 support grid transmission on the detector coordinates, based on the calibration data base file `s2gridv3.fits`, smoothed by the position resolution of GIS at 2.0 keV. Contour levels are 0.75, 0.85, and 0.95. Lower panel shows a cross section at $DETY = 0.0$. IV-9

4.5 Energy dependence of the position resolution (FWHM) of the GIS with (thick line) and without (thin line) the effect of parallax. This plot is based on the version 4.0 GIS response. IV-9

4.6 Upper panel shows a contour map of the GIS RMF `gis2v4_0.rmf`. Contour levels are every factor of 2. Lower panel shows the slices at 1 (thin solid line), 2 (dash), 4 (dot-dash), and 8 (thick solid line) keV. IV-10

4.7 Energy dependence of the energy resolution (FWHM) of the GIS. This plot is based on the version 4.0 GIS response. IV-10

4.8 Pointing positions of the Crab nebula (•) overlayed on the grid maps of GIS2 and GIS3. Open circle labeled "q1" shows the 1CCD nominal position, and '×' shows the optical axis. IV-11

4.9 The Crab nebula spectrum fitted in the entire 0.6–10 keV energy band with an absorbed power-law model. The observation was conducted at the 1CCD nominal position on 28 Sep 1994. The spectrum is dead-time corrected and the CXB + NXB spectrum is subtracted. Deadtime corrected effective exposure is 14,466 s. The best fit parameters are shown in table 4.4. Upper panel shows the GIS2+3 spectrum (crosses) and the best fit model (solid line). Middle panel shows residuals plotted in unit of σ. Lower panel shows ratios of the data to the model. IV-12

4.10 Offset angle dependence of the best fit parameters for the Crab nebula spectra, observed at different positions on the detector plane. (a) Absolute flux in the 2–10 keV energy band, (b) photon index, (c) column density. Open circles show GIS2, and triangles GIS3. Note that the results shown here are based on a slightly older version of the XRT response, which gives some inconsistensy with the value shown in table 4.4. . . . . *IV* - 13

4.11 Four examples of XRT light paths: (a) normal path, (b) reflection only by primary mirrors, (c) reflection only by secondary mirrors, (d) multiple reflections by front and back surfaces of mirrors. . . . . *IV* - 14

4.12 Three of the Crab stray light images taken by GIS3 in the 0.7–10 keV band, shifted and superposed on the detector plane so as to reproduce correct angular relations with respect to the Crab nebula. The location of the Crab is indicated with a filled circle, and the optical axis for each observation is offset by 60′ from the Crab. . . . . *IV* - 16

4.13 Ray-tracing image of the stray light pattern at 1 keV for the offset angle $\theta =$ 60′ and the azimuthal angle $\phi = 225°$. A filled circle shows a position of the optical axis. A superposed circle of $r = 25$ mm on the image corresponds to the GIS f.o.v. . . . . *IV* - 16

4.14 (a) Calculated ratios of the CXB photons which come from the offset angle $\theta > \Theta$, to the total CXB photons integrated within the radius of 20 mm from the optical axis, at 1 (thick solid line), 2 (dashed), 4 (dot-dashed), and 8 (thin solid line) keV. (b) The averaged CXB spectrum (crosses) and the NXB spectrum (filled circles), plotted with calculated contributions from $\theta =$ 0–20′, 20–40′, 40–60′, 60–80′, and 80–150′. . . . . *IV* - 17

4.15 Azimuthally averaged radial profiles of the CXB image (thick solid lines) calculated by ray-tracing at the energies of 1, 2, 4, and 8 keV. Contributions of the normal reflection (dashed), the primary only reflection (dotted), the secondary only reflection (dot-dashed), and the multiple reflection (thin solid lines) are also plotted. . . . . *IV* - 17

4.16 (a) Spectra of the Crab stray observations taken by GIS2 (upper panel) and GIS3 (lower panel) integrated in the radius of 20 mm from the optical axis of each sensor. The Crab has been placed at various offset angles as specified in the figure. The CXB+RNXB spectra are subtracted after dead time correction. (b) Simulated spectra of the Crab stray observations. The Crab nebula is assumed to have an absorbed power-law spectrum of $\Gamma = 2.10$, $N_{\rm H} = 3.0 \times 10^{21}$ cm^{-2}, and the power-law normalization of 9.7 c s^{-1} cm^{-2} keV^{-1} at 1.0 keV. . . . . *IV* - 19

4.17 Upper panels show counting rates of the Crab stray observations and the ray-tracing simulations in (a) 0.7–10 keV, (b) 1.2–2.0 keV, and (c) 2.0–4.0 keV energy band, plotted versus offset angle of the Crab nebula. Lower panels show the ratios of observation to simulation. . . . . *IV* - 20

4.18 Plot of the ARFs for GIS2 (thick line) and GIS3 (thin line). Left panel shows the point source ARFs at 1CCD nominal position with integration radius 6 mm. Right panel shows the CXB ARFs with integration radius 20 mm from the optical axis. . . . . *IV* - 21

4.19 Integrated spectra of the day-earth (smooth line), the CXB (crosses), and the night-earth (filled circles) observations taken by the GIS2+3 on the whole detector area as shown in figure 4.20. Each of exposure time is given in the parentheses. The CXB and the day-earth spectra contains RNXB. Possible origin of the line feature with the energy in keV are also given in the figure. The flare-cut (table 4.6) is NOT applied. . . . . *IV* - 23

4.20 Integrated images taken by GIS2 (left panel) and GIS3 (right panel) for the entire night-earth observations with exposure time of 1,202 ks in the 0.6–10 keV energy band. The white spot in the figure shows the optical axis of each detector. Both images are masked by the standard image masking, i.e. selection of $r \leq 25$ mm from the detector center and elimination of the calibration isotope. The flare-cut (table 4.6) is applied. . . . . *IV* - 24

4.21 Energy sorted radial profiles of the GIS counts during the night-earth observations. GIS2 and GIS3 data are summed up. The mark of '+' shows 0.6–1.0 keV, 'o' 1.0–2.0 keV, '•' 2.0–4.0 keV, and '×' 4.0–8.0 keV. The flare-cut (table 4.6) is applied. . . . . *IV* - 25

4.22 Band profiles during the CXB and night-earth observations in -5 mm $\leq$ XRTY $\leq +5$ mm for GIS2. Upper panel shows a profile in the 1–2 keV energy band, and lower panel 4–8 keV. The origin of the coordinates for $XRTX$-$XRTY$ is the optical axis. Filled circles, crosses, and diamonds represents the raw CXB including RNXB, the residual night-earth, and the CXB after subtracting the residual night-earth, respectively. The flare-cut (table 4.6) is applied for both the CXB and the residual night-earth data. . . . . *IV* - 25

4.23 Correlation between COR and $LDHIT$ during the night-earth observations. $LDHIT$ is integrated for every 32 s. The flare-cut (table 4.6) is NOT applied . . . . *IV* - 26

4.24 Long term (June 1993 – June 1995) variations of the GIS2+GIS3 counting rate during the night-earth observations in the 0.6–1.0 (open circle), 1.0–2.0 (diamond), 2.0–4.0 (filled circle), and 4.0–8.0 (crosses) keV energy bands, integrated within the radius of 20 mm from the optical axis. A solid line on the data of 4.0–8.0 keV band shows the best fit line of $y = 0.00257x + 0.414$. The flare-cut (table 4.6) is applied. . . . . *IV* - 26

4.25 Distribution map for three types of phenomena on the Earth surface. The mark "·" represents a position when $H02$ is less than the lower solid line in figure 4.26, where the COR-map is thought to be inaccurate. The mark "•" represents a position when $H02$ is greater than the upper solid line in figure 4.26 (the hard-flares). The mark "+" represents a position when $H02 < 1000$ c/32 s = 31.25 c/s and $RNTE > 15$ c/32 s = 0.46875 c/s in figure 4.27a (the soft-flares). Two regions surrounded by solid lines define the dangerous areas where we should be cautious of the hard- and the soft-flares. . . . . *IV* - 27

4.26 Correlation between COR and $H02$ counts during the night-earth observations. $H02$ is integrated for every 32 s. A dashed line means a function $f(x) = (109.3 - 17.05x + 1.127x^2 - 0.02627x^3)/32$ derived from fitting. Two solid lines below and above show $f(x)$ scaled by 0.9 and 1.5 times, respectively. The flare-cut (table 4.6) is NOT applied. . . . . *IV* - 28

4.27 (a) A correlation between $H02$ and $RNTE$, and (b) a correlation between COR and $RNTE$. $H02$ and $RNTE$ are integrated for every 32 s. $RNTE$ is integrated in $r \leq 17$ mm in the 0.3–11 keV energy band. Crosses superposed on the figure show averages (upper) and standard deviations (lower) in each $H02$ or COR bins. The flare-cut (table 4.6) is NOT applied. . . . *IV* - 28

4.28 $RBMCNT$ distribution for the entire night-earth observations (thin solid line) and during the soft-flares. . . . . *IV* - 29

4.29 Almost the same as figure 4.27 except that the flare-cut (table 4.6) is applied. . . . . *IV* - 30

4.30 $H02$ sorted spectra (upper panel) and radial profiles (lower panel) of the GIS counts during the night-earth observations in the 0.6–7.0 keV energy band. The mark '+' represents the data when $H02$ is in the range 50–80 c/s, 'o' 40–45 c/s, '•' 30–35 c/s, and '×' 20–25 c/s. $H02$ are integrated for every 16 s. The flare-cut (table 4.6) is applied. . . . . *IV* - 31

4.31 $H02$ distribution for the entire night-earth observations. Net exposure time (sec) in each $H02$ 5 c/s bin is given in the figure. The flare-cut (table 4.6) is applied. . . . . *IV* - 32

4.32 Figures to check the RNXB reproducibility by H02-sorting method. Upper panel shows the actual $RNTE$ (crosses) and the H02-sorting method prediction (solid line), in the 0.7–7.0 keV energy band, for every 10 ks exposure. Middle panel shows ratios of the $RNTE$ to the prediction. The solid line shows the best fit line, and fitting results are indicated in the figure inset. Lower panel shows a distribution of the ratios. The mean value and the standard deviation for the distribution are indicated in the inset. . . . . *IV* - 33

5.1 Galactic positions of the observed fields in table 5.1. "Lynx Field" and "Lockman Hole" are also included. . . . . *V* - 2

5.2 LSS pointing positions . . . . *V* - 3

5.3 Images of (a) M^{EXP}, (b) M^{OBS}, and (c) M^{CCF} for the four pointing observations in the Braccesi Field. Coordinates superposed on the images are J2000. (a) Gray scale image of M^{EXP}. White and black pixels correspond to 0 s and 138,954 s exposure, respectively. (b) Dot-map image of M^{OBS} in the 0.7–7.0 keV energy band. (c) Contour-map image of M^{CCF} in the 0.7–7.0 keV energy band. Contour levels are (5, 10, ..., 95, 100) $\times 10^{-6}$ c s^{-1} pixel^{-1}. . . . . *V* - 10

6.1 Ring-sorted spectra of (a) CXB and (b) day-earth, integrated in the radius of 0–5 mm (•), 5–10 mm (○), 10–15mm (◇), 15–20 mm (+), and 20–25 mm (△), centered on the optical axis on each detector plane. Panel (c) shows ratios of (b) to (a). GIS2 and GIS3 spectra are summed up. . . . . *VI* - 2

6.2 (a) The ring-sorted CXB spectra of figure 6.1a, fitted with a power-law plus *RS* model of one solar abundances. Top panel shows each spectrum (markers) and the best fit model (solid lines). Lower five panels show residuals from each spectrum. All the fit parameters except normalization are common to all the spectra. (b) The model normalization for each spectrum plotted versus radius of the rings. Normalization of the inmost ring is defined to be 1.0. . . . . *VI*-3

6.3 The average CXB spectrum fitted with (a) power-law and (b) thermal bremsstrahlung model, both with galactic absorption, in the 2–10 keV band. Upper panel of each figure shows GIS2+3 spectrum (crosses) and the best fit models (solid lines). Although the fitting ignored the energy range below 2 keV, the best-fit model is extended to < 2 keV to illustrate the soft-excess. *VI*-5

6.4 Changes of χ^2/d.o.f (upper panel) and the CXB photon index (lower panel) when the lower limit of the fitting energy range is shifted down from 2.0 keV to 0.6 keV, with upper limit fixed to 10 keV. Error bars of photon indices at 0.6–0.8 keV are not plotted becase χ^2 is too big to evaluate the errors. *VI*-6

6.5 The average CXB spectrum in the LSS field, fitted in the entire 0.6–10 keV energy band with an absorbed power-law models plus a soft component. The soft component is represented by (a) a steep power-law or (b) a low temperature *RS* model of 1 solar abundances. Upper panel of each figure shows GIS2+3 spectrum (crosses), the best fit models (solid lines), the absorbed power-law component (dashed lines) and the soft component (dot-dashed lines). Lower panels show residuals plotted in the unit of σ. *VI*-7

6.6 Confidence contours of the fitting parameters to the average CXB spectrum in the LSS field with the absorbed power-law ($PL^{\rm hard}$) + steep power-law ($PL^{\rm soft}$) model shown in figure 6.5a. Contours (from inner to outer) represent 68, 90 and 99% confidence levels. Crosses show the best fit position. (a) Photon index of $PL^{\rm hard}$ ($\Gamma^{\rm hard}$) vs. 2–10 keV band flux of $PL^{\rm hard}$ ($F_{\rm X}^{\rm hard}$). (b) $\Gamma^{\rm hard}$ vs. 0.5–2 keV band flux of $PL^{\rm soft}$ ($F_{\rm X}^{\rm soft}$). (c) $\Gamma^{\rm hard}$ vs. Photon index of $PL^{\rm soft}$ ($\Gamma^{\rm soft}$). (d) $\Gamma^{\rm soft}$ vs. $F_{\rm X}^{\rm soft}$. *VI*-8

6.7 Same as figure 6.7, but for the absorbed power-law ($PL^{\rm hard}$) + Raymond-Smith (*RS*) model shown in figure 6.5b. (a) $\Gamma^{\rm hard}$ vs. $F_{\rm X}^{\rm hard}$. (b) $\Gamma^{\rm hard}$ vs. *RS* normalization. (c) $\Gamma^{\rm hard}$ vs. *RS* temperature. (d) *RS* temperature vs. *RS* normalization. *VI*-8

6.8 Confidence contour of *RS* temperature vs. *RS* abundance, when fitting the average CXB spectrum in the LSS field with $PL^{\rm hard}$ + *RS* model. Contours (from inner to outer) represent 68, 90 and 99% confidence levels. Cross shows the best fit position. *VI*-9

6.9 Changes of the CXB hard power-law component photon index ($\Gamma^{\rm hard}$; upper panel) and the soft power-law component flux ($F_{\rm X}^{\rm soft}$; lower panel) when the RNXB level is scaled to 0.95–1.05 from the nominal value. *VI*-9

6.10 Changes of the CXB hard power-law component photon index ($\Gamma^{\rm hard}$; upper panel) and the soft power-law component flux ($F_{\rm X}^{\rm soft}$; lower panel) when GIS beryllium window have adittional thickness of -0.5 – $+0.5$ μm from the nominal value. *VI*-10

6.11 Changes of the CXB hard power-law component photon index ($\Gamma^{\rm hard}$; upper panel), the soft power-law component flux ($F_{\rm X}^{\rm soft}$; middle panel), and the hard power-law component flux ($F_{\rm X}^{\rm hard}$; lower panel), when stray light (filled circles for secondary only reflection, open circles for multiple reflection) level is scaled to 0.7–1.1 from the nominal value derived in §4.3. . . . . . . *VI*-11

6.12 (a) Flux and (b) photon index of the ring-sorted CXB spectra plotted versus the radius of each ring. Filled circles show the fiting results with the nominal XRT response, and open circles show the results with the modified XRT response. *VI*-13

6.13 Ratio of the observed Crab counts to that predicted by the ray-tracing calculation in (a) 1.2–2.0 keV and (b) 6.0–8.0 keV plotted against the offset angle from the XRT optical axis. Integration radius is 6 mm centered on the Crab nebula. Filled circles represent GIS2 and open circles GIS3. The point with an arrow show the observation at the 1CCD nominal position. Smooth solid lines show the function of equation (6.1). We assume that the Crab nebula has a constant spectrum of an absorbed power-law, i.e. $\Gamma = 2.1$, $norm = 9.7$ c s^{-1} cm^{-2} keV^{-1}, and $N_{\rm H} = 3.0 \times 10^{21}$ cm^{-2}. *VI*-13

7.1 The NEP spectrum fitted with the $PL^{\rm hard}$ + $PL^{\rm soft}$ model in the 0.6–10 keV energy band. $PL^{\rm hard}$ is modified with Galactic absorption of $N_{\rm H} = 4.2 \times 10^{20}$ cm^{-2}. Upper panel shows GIS2+3 spectrum (corosses), the best fit models (solid lines), the absorbed $PL^{\rm hard}$ component (dashed lines), and the $PL^{\rm soft}$ component (dot-dashed lines). Lower panel shows residuals plotted in the scale of σ. *VII*-3

7.2 Gray scale image of $M^{RAW} = \sum_j T_j\, ccf\left[B_j^{OBS} - B_j^{RNXB}\right]$ for the entire LSS observations. White and black pixel corresponds to 0.0 and 10.0 c pixel^{-1}, respectively. *VII*-6

7.3 Gray scale image of $M^{\overline{CXB}} = \sum_j T_j\ ccf\left[B_j^{\overline{CXB}}\right]$ for the entire LSS observations. White and black pixels correspond to 0.0 and 10.0 c pixel^{-1}, respectively. *VII*-6

7.4 Gray scale image of $M^{RATIO}(SKYX, SKYY)$ for the entire LSS observations. White pixel corresponds to 0.0 and black pixel corresponds to 3.0. Values of pixels where $M^{\overline{CXB}} < 1.0$ c pixel^{-1} are set to 0.0. . . . . *VII*-7

7.5 Distribution of pixel values in figure 7.4. Left panel shows the distribution in the range of 0–5, and right panel shows in the range of 0.55–2.0. In right panel, the distribution (crosses) is fitted with the function of equation (7.10) and the best fit line (solid line) and each component (two dashed lines) are overlaied. *VII*-8

7.6 Gray scale image of $M^{FLAT}(SKYX, SKYY)$ for the entire LSS observations. White pixel corresponds to -0.1 and black pixel corresponds to 0.4. . . . . *VII*-9

7.7

Distribution of pixel values in figure 7.6. *VII*-9

7.8 Radial profile of 8′ offset Cyg X-1 image taken by GIS2 in the 5–6 keV energy band (histogram). Smooth solid line superposed on the histogram shows the function of $f(x) = 528.5\ \exp(-0.96\ x) + 4.95\ \exp(-0.1$
VII-10

7.9 The source-mask for the entire LSS observations. White and black pixels correspond to 0.0 and 1.0, respectively. *VII*-11

7.10 Correlation between the source flux in the 2–10 keV energy band listed by Ueda (1996) vs. the pixel value of $M^{FLAT}(SKYX, SKYY)$ from our analysis at each source position. The source-list flux plotted on left panel assumes $\Gamma = 1.7$. On right panel, photon index is derived from the five-energy-band spectrum fitting by Ueda (1996). *VII*-12

7.11 CXB base levels ($= \alpha$) in the 0.7–7.0 keV energy band (open circles), plotted against the field ID. Error bars represent 90% confidence levels. Filed circles represent the results after the point sources have once been excluded at the threshold of 0.1 on M^{FLAT}, and M^{RATIO} was calculated again on the remaining region. *VII*-14

7.12 $\Gamma^{\rm hard}$, $F_{\rm X}^{\rm hard}$ (2–10 keV), and $F_{\rm X}^{\rm soft}$ (0.5–2 keV) of table 7.1 (no source-masking; open circles), table 7.1 (threshold 0.1; filled circles), and table E.1 (threshold 0.06; diamonds), plotted against the field ID. Error bars represent 90% confidence level. *VII*-17

7.13 Correlations of $\Gamma^{\rm hard}$ vs. $F_{\rm X}^{\rm hard}$ (2–10 keV) in each sample field for (a) no source-masking, (b) after processed through the source-maskings at the threshold of 0.1, and (c) after processed through the source-maskings at the threshold of 0.06. Error bars represent the 90% confidence levels independently derived for $\Gamma^{\rm hard}$ and $F_{\rm X}^{\rm hard}$. *VII*-20

7.14 Confidence contours of $\Gamma^{\rm hard}$ vs. $F_{\rm X}^{\rm hard}$, in each sample field after processed through the source-masking at the threshold of 0.1. Contours (from inner to outer) represent 68, 90 and 99% confidence levels. Crosses show the best fit position in the labeled fields. *VII*-20

7.15 The remaining fraction (%) of $F_{\rm X}^{\rm hard}$ plotted against the remaining fraction (%) of the integration area on the sky in each sample field, for (a) after processed through the source-maskings at the threshold of 0.1 and (b) at the threshold of 0.06. Both (a) and (b) are relative ratios to those with no source-masking. *VII*-21

7.16 Same as middle and lower panels in figure 7.12, but $\Gamma^{\rm hard}$ are fixed to 1.44. *VII*-22

7.17 The CXB base level α without the source-maskings, plotted against $F_{\rm X}^{\rm hard}$ for (a) no source-masking with $\Gamma^{\rm hard}$ left free, (b) after processed through the source-maskings at the threshold of 0.1 with $\Gamma^{\rm hard}$ left free, and (c) after processed through the source-maskings at the threshold of 0.1 with $\Gamma^{\rm hard}$ fixed to 1.44. Error bars represent the 90% confidence levels independently derived for α and $F_{\rm X}^{\rm hard}$. *VII*-22

7.18 $F_{\rm X}^{\rm hard}$ of each sample field plotted against (a) $\Gamma^{\rm hard}$, (b) $F_{\rm X}^{\rm hard}$ with $\Gamma^{\rm hard}$ left free, and (c) $F_{\rm X}^{\rm hard}$ with $\Gamma^{\rm hard}$ fixed to 1.44. All of them are processed through the source-maskings at the threshold of 0.1. Error bars represent the 90% confidence levels independently derived for $F_{\rm X}^{\rm hard}$, $\Gamma^{\rm hard}$, and $F_{\rm X}^{\rm hard}$. *VII*-24

7.19 Average CXB spectra for (a) LSS with no source-masking, (b) LSS processed through source-masking at the threshold of 0.1, (c) LSS processed through source-masking at the threshold of 0.06, (d) ALL (SA57+LSS+Draco+NEP+QSF3+ZSYS+BF) processed through source-masking at the threshold of 0.10, fitted with the absorbed power-law model in the 0.6–10 keV energy band. The Galactic absorptions are fixed as given in table 7.5, and $\Gamma^{\rm soft}$ are left free. Upper panels show GIS2+3 spectrum (corosses) and the best fit model (solid line). Lower panels show residuals plotted in the unit of σ. . . . *VII*-26

7.20 Confidence contour of $\Gamma^{\rm hard}$ vs. $F_{\rm X}^{\rm hard}$, for the spectra shown in figure 7.19. The Galactic absorptions are fixed as given in table 7.5, and $\Gamma^{\rm soft}$ are fixed to 6.0. Contours (from inner to outer) represent 68, 90 and 99% confidence levels, and crosses show the best fit position. . . . *VII*-27

8.1 Unfolded 0.6–10 keV energy spectra of the average CXB in LSS including point sources. Thick lines and crosses in upper (lower) panel represent the best fit $PL^{\rm soft} + PL^{\rm hard}$ ($RS + PL^{\rm hard}$) model shown in figure 6.5a (figure 6.5b), respectively. Hard- and soft-components are also shown individually in thick lines. Results from ROSAT PSPC (Hasinger 1992), Einstein IPC (Wu et al. 1991), HEAO-1 A2 (Marshall et al. 1980), and ASCA SIS (Keith et al. 1995) are overlaied. . . . *VIII*-4

8.2 Same as upper panel of figure 8.1, except that three GIS spectra in LSS, NEP, and ZSYS after processed through the source-masking at the threshold of 0.10 are instead plotted, separately. . . . *VIII*-5

8.3 The $\log N$-$\log S$ relation in the 2–10 keV energy band. Solid line with a slope of -1.5 represents the extension of the HEAO-1 A2 result expressed in equation 2.5. Dashed line with a slope of -1.0 represents the 100% CXB limit, assuming the CXB intensity as 6.2×10^{-8} erg s^{-1} cm^{-2} str^{-2} (2–10 keV). The 90% confidence contour from Ginga fluctuation analysis (Hayashida 1990), the point from Ginga source survey (Kondo 1991), and the preliminary results from ASCA Large Sky Survey (Ueda, private communication) are overlaid. Photon index of 1.7 is assumed to calculate the flux. This figure is kindly provided by Y. Ueda. . . . *VIII*-7

8.4 The fractional residuals, i.e. (Data − Model) / Model, of the total CXB spectrum shown in figure 7.19d to a power-law of $\Gamma = 1.4$. The data excess just below ~ 2 keV is due partly to the energy resolution (~ 20% FWHM at 1 keV) of the GIS. . . . *VIII*-8

8.5 The fractional residuals of various Seyfert 1 and Seyfert 2 mixture 2–10 keV CXB spectra to a power-law of $\Gamma = 1.4$, adopted from Matt and Fabian (1994). The solid lines show the model without no line emission. The dotted lines include the iron line emission from the intervening matter, while the dashed lines show the further intrinsic line emission. The fraction of Seyfert 2 galaxies is ranging 0.6–0.8. Seyfert 1 (unabsorbed) and Seyfert 2 (absorbed) are assumed to have the same intrinsic spectrum and evolve in the same way, in terms of the unified model of the AGN (e.g. Antonucci & Miller 1985). The model A1 is the unevolved model, while the evolution of the volume emissivity as $(1+z)^{2.5}$, $(1+z)^{4.5}$ and $(1+z)^{6}$ are assumed for A8/A10, A13/A16, and A17, respectively. The difference between A8 (A13) and A10 (A16) is the lower-limit $N_{\rm H1}$ of the intrinsic absorption; $N_{\rm H1} \sim 10^{23}$ cm^{-2} for A8, A13, and A17, while $N_{\rm H1} = 10^{24}$ cm^{-2} for A13 and A16. . . . *VIII*-9

8.6 Positions of the HEAO-1 A2, Ginga LAC, and ASCA XRT+GIS on the Ω_e-S_c plane. Contours labeled 1%, 2%, …, 10% represents the expected fractional CXB fluctuation, i.e., σ_{CXB}/I_{CXB}. . . . *VIII*-12

B.1 LSS . . . *B*-2
B.2 SA57 . . . *B*-3
B.3 Draco Field . . . *B*-3
B.4 NEP . . . *B*-4
B.5 QSF3 . . . *B*-4
B.6 z-system . . . *B*-5
B.7 Braccesi Field . . . *B*-6
B.8 Jupitar . . . *B*-7
B.9 Arp 220 . . . *B*-7
B.10 3C368 . . . *B*-7

C.1 LSS . . . *C*-2
C.2 SA57 . . . *C*-3
C.3 Draco Field . . . *C*-3
C.4 NEP . . . *C*-4
C.5 QSF3 . . . *C*-4
C.6 z-system . . . *C*-5
C.7 Braccesi Field . . . *C*-6
C.8 Jupiter . . . *C*-7

C.9 Arp220 . . . . C-7
C.10 3C368 . . . . C-7

D.1 SA57 . . . . D-1
D.2 a-LSS D-2
D.3 b-LSS D-2
D.4 c-LSS D-2
D.5 d-LSS D-3
D.6 Draco Field D-3
D.7 NEP D-3
D.8 QSF3 . . . . D-4
D.9 z-system D-4
D.10 Braccesi Field D-4
D.11 Jupiter D-5
D.12 Arp 220 . . . . D-5
D.13 3C368 . . . . D-5

E.1 LSS E-2
E.2 SA57 . . . . E-2
E.3 Draco Field E-2
E.4 NEP E-2
E.5 QSF3 . . . . E-3
E.6 z-system E-3
E.7 Braccesi Field E-4
E.8 Jupiter E-4
E.9 Arp 220 . . . . E-4
E.10 3C368 . . . . E-4

F.1 LSS F-2
F.2 SA57 . . . . F-2
F.3 Draco Field F-2
F.4 NEP F-2
F.5 QSF3 . . . . F-3
F.6 z-system F-3
F.7 Braccesi Field F-4
F.8 Jupiter F-4
F.9 Arp 220 . . . . F-4
F.10 3C368 . . . . F-4

G.1 Map of the total number of hydrogen atoms in different directions on the sky, adopted from the NRAO Radio CD-ROM. Seven different 21 cm HI surveys are combined, and averaged over 1 square degree intervals. Most of the arcs and circular structures outline huge regions created by supernova explosions (Dickey, and Lockman 1990). G-2
G.2 The X-ray sky from HEAO-1 A2 in Galactic coordinates at 3° resolution, adopted from the WWW service of NASA/GSFC at *http://heasarc.gsfc.nasa.gov*. Bright sources and diffuse emission from the Galaxy dominate at low Galactic latitudes. Besides it, X-ray sky is dominated by the CXB, and fluctuations in the CXB are seen in at high Galactic latitude (Allen, Jahoda, and Whitlock in article Vol. 5 of Legacy, journal of the HEASARC). G-2
G.3 ROSAT PSPC all sky survey X-ray intensity Galactic coordinates map in (a) 0.25 keV, (b) 0.75 keV, and (c) 1.50 keV energy band, adopted from Snowden et al. (1995). G-3
G.4 Brief descriptions of the main features seen in figure G.3, adopted from the same paper. G-4
G.5 (a) C-band (~ 160–284 eV) and (b) M-band (~ 490–~ 1090 eV) maps from the Wisconsin sky survey (McCammon et al. 1983), adopted from the review by McCammon & Sanders (1990). G-4

H.1 (a) The observed Crab counting rate in the 0.7–10 keV energy band plotted against the offset angle from the XRT optical axis. Filled circles represent GIS2 and open circles GIS3. (b) Same as upper panel of figure 4.17a. Solid line represents equation (H.10). H-2
H.2 Calculation of Ω_e for the XRT+GIS. H-3

List of Tables

3.1 Design parameters and performance of the ASCA XRT . . . . III - 7
3.2 Design parameters and performance of the SIS . . . . III - 11
3.3 Design parameters and performance of the GIS . . . . III - 14
3.4 NXB count rate of the GIS in the 0.17–11 keV range under various rejection conditions . . . . III - 21
3.5 Summary of the GIS monitor counts . . . . III - 22

4.1 Summary of the coordinates . . . . IV - 2
4.2 Summary of factors constituting the response function . . . . IV - 3
4.3 Summary of the calibration files of XRT and GIS for jbldarf . . . . IV - 4
4.4 An absorbed power-law fits to the 0.6–10 keV spectrum of the Crab nebula IV - 12
4.5 Log of the Crab stray observations . . . . IV - 18
4.6 Summary of the flare-cut conditions . . . . IV - 30
4.7 Systematic errors of the RNXB counts in the 0.7–7.0 keV energy band . . . IV - 33

5.1 Summary of the observed fields to be employed in this thesis. . . . . V - 1

6.1 Model fits to the 2–10 keV spectrum of the CXB . . . . VI - 5
6.2 Model fits to the 0.6–10 keV spectrum of the average CXB . . . . VI - 7
6.3 Summary of the systematic errors for the CXB spectrum in the LSS field . VI - 14

7.1 ($PL^{\rm hard}$+$PL^{\rm soft}$) fits to the 0.6–10 keV spectrum of each field including point sources. All errors are 90% confidence level. $\Gamma^{\rm soft}$ is fixed to 6.0. . . VII - 2
7.2 Fitting results of M^{RATIO} pixel values distribution for each sample field . VII - 14
7.3 ($PL^{\rm hard}$+$PL^{\rm soft}$) fits to the 0.6–10 keV spectrum of each field masking point sources at the threshold of 0.1 on M^{FLAT}. All errors are 90% confidence level. $\Gamma^{\rm soft}$ is fixed to 6.0. . . . . VII - 16
7.4 Mean values and standard deviations of $\Gamma^{\rm hard}$, $F_{\rm X}^{\rm hard}$, and $F_{\rm X}^{\rm soft}$. . . . . . . VII - 18
7.5 ($PL^{\rm hard}$+$PL^{\rm soft}$) fits to the 0.6–10 keV spectrum of the total CXB (SA57+LSS+ Draco+NEP+QSF3+ZSYS+BF) and the whole LSS. All errors represent 90% confidence levels. . . . . VII - 25

8.1 Summary of the previous results and the present work (ASCA XRT+GIS) *VIII* - 11
8.2 Rough estimations of the effective beam size Ω_e (deg^2) for each CXB observation . . . . . *VIII* - 12

A.1 Pointing list of the LSS observations in GO-1 and GO-2 . . . . . *A* - 2
A.2 Pointing list of the LSS observations in GO-3 . . . . . *A* - 3
A.3 Pointing list of the observations . . . . . *A* - 4

E.1 ($PL^{\rm hard}$+$PL^{\rm soft}$) fits to the 0.6–10 keV spectrum of each field with point sources being masked at the threshold of 0.06 on M^{FLAT}. All errors are the 90% confidence level. $\Gamma^{\rm soft}$ is fixed to 6.0. . . . . . *E* - 1

G.1 Summary of the X-ray images in this chapter . . . . . *G* - 1

Chapter 1

Introduction

1.1 The Cosmic X-ray Background (CXB)

It is not too much to say that the X-ray astronomy began with the cosmic X-ray background (CXB), a diffuse X-ray radiation coming from all directions of the sky (for reviews, see Boldt 1987; Fabian & Balcons 1992). Discovery of the CXB precedes that of cosmic microwave background (CMB) by Penzias and Wilson (1965), and goes back to the rocket experiment made in 1962 which was intended to study fluorescence X-rays from the Moon. The observers did not detect lunar X-rays, but instead they discovered the first extra-solar X-ray source which we call today Scorpius X-1, as well as the CXB (Giacconi et al. 1962).

The CXB dominates the energy density of the entire X-ray sky. Its spectrum has a canonical photon index $\Gamma = 1.4$ (photon number flux $\propto E^{-\Gamma}$ where E is the X-ray photon energy) in the 2–10 keV range, gradually steepening up to a few hundreds keV (see §2.2.1). The CXB brightness is highly isotropic, except for a small dipole anisotropy (§2.2) which arises from solar system's proper motion with respect to the Hubble flow. Only a week correlation (13±5%) was detected with bright galaxy counts for the 2–10 keV CXB (Jahoda et al. 1991). These properties make us confident that the CXB undoubtedly has a cosmological origin, except in the energy range below ~ 2 keV where contributions from various Galactic components are significant. Indeed, this fact has been the prime motive force for the huge amount of effort spent in the CXB studies, for more than 30 years since its first discovery. Nevertheless, the exact origin of the CXB is still unclear.

So far, two categories of explanations were proposed for the CXB. One of them regard the CXB as a thermal radiation from hot diffuse plasmas permiating the universe, inspired by the apparently thermal shape of the CXB spectrum (see §2 for detail). However, this possibility has been ruled out (at most 0.01% of the total CXB brightness), because of the lack of the inverse-Compton effect expected in the CMB spectrum (§2). Therefore, presently we are left with only the other category of models, which regard the CXB as a superposition of unresolved faint X-ray sources (mostly active galactic nuclei, or AGNs) distributed up to cosmological distances ($z \sim 1$–4).

As the cosmic X-ray observations made a rapid progress, a progressively larger farction of the CXB has been resolved into discrete X-ray sources (Boldt 1987). Particularly, deep observations with ROSAT have resolved ~ 70 % of the CXB below ~ 2 keV into discrete sources (Shanks et al. 1991; Hasinger et al. 1993). The faintest point sources thus resolved are by more than 8 orders of magnitude X-ray fainter than the first discovered Scorpius X-1, and most of them have subsequently been identified with dsitant AGNs. The ROSAT observations have also shown that the CXB spectrum steepens to $\Gamma \sim 2.1$ below 2 keV, and suggested that, in this energy band, the faint AGNs have similar spectral slopes.

1.2 Problems with the CXB

The ROSAT results on the CXB, though remarkable, are limited to the soft energy reange below ~ 2 keV where ordinary X-ray telescopes can work. This is a very minor portion of the vast energy region over which the CXB phenomenon is seen. Furthermore below ~ 2 keV, the CXB begins to be strongly affected by soft X-rays from Milky-Way plasmas and from local environment (Hot Bubbles) around the solar system (§2), both of which are diffuse but highly anisotropic. Below ~ 1 keV, photoelectric absorption of the CMB photons by our Galaxy's interstellar medium becomes significant, too. These facts urge us to carry on the CXB investigations in harder energy ranges.

In fact, when we turn our eyes to the energy region above 2 keV, the CXB mystery is far from being solved. Among several problems, the most serious one is so called "spectral paradox" (Boldt 1987); as described in §2.3.3, most known X-ray sources have too soft (steep) spectra to account for the observed CXB spectral slope of $\Gamma = 1.4$. Therefore, when a contribution of known objects is subtracted from the CXB spectrum, we are left with unusually hard spectral component. There is a possibility that highly absorbed AGNs, such as type 2 Seyfert galaxies, can provide the required hard spectral component (§2.3.4). However this view needs examinantion from X-ray observations above ~ 2 keV, where their spectral contribution is expected to be significant.

The CXB isotropy makes an outstanding contrast to the enormous inhomogeneities observed in the local universe, such as voids, great walls, and superclusters. The CXB isotropy provides a strong constraint on the lumpiness of spatial distributions of X-ray objects (mainly AGNs) contributing to the CXB, presumably in redshift ranges of $z \sim$ 0.5–3. At present, we do not know wheter the CXB isotropy can be reconciled with the inhomogeneities of the present-day universe, in terms of scenarios for the AGN luminosity evolution and for the evolution of large-scale structures.

1.3 CXB investigations with ASCA

With the ASCA observatory (Tanaka et al. 1994) launched on 20 February 1993, the CXB study is expected to make a big progress. ASCA is the first X-ray satellite covering an energy range of 0.5–10 keV, as realized by the four units of co-aligned X-ray Telescopes (XRTs; §3.2); importance of the sensitivity up to ~ 10 keV in the CXB study may need no explanation. Furthermore, ASCA for the first time combines the *classical* energy range above ~ 2 keV explored by non-imaging experiments, and the soft X-ray range below ~ 2 keV where Einstein and ROSAT missions have made important contributions.

The XRT onboard ASCA provides several more advantages in the CXB study. It gives an imaging capability with a moderate angular resolution of order ~ 3 arcmin. This enables us to detect and exclude point sources in the field of view, hence to study the genuine *unresolved* CXB for the first time above 2 keV. The ASCA field of view of ~ 40′ diameter is also ideal, because the large-scale structures seen in the present-day universe has a typical scale length of 100 Mpc, which translates to an angular scale of 0.5°–1° at redshift ranges of $z = 1$–3 where the CXB may originate. Yet another advantage is that the XRT has a very high throughput, achieving a photon collecting area three times that of ROSAT at 1 keV when the four modules are combined. Accordingly we can collect much larger number of CXB photons than ROSAT.

The XRT focal plane is equiped with two types of imaging X-ray detectors, the Solid-State Imaging Spectrometer (SIS; §3.3) and the Gas Imaging Spectrometer (GIS; §3.4). Both SIS and GIS have two particular advantages for the CXB study. One is their superior energy resolutions, which enable us to quantify the CXB spectrum with a high accuracy. The other is their extremely low level of non X-ray background, which is an essential feature when we investigate a diffuse emission with imaging optics.

1.4 Outline of the present thesis

In the present thesis, we attempt to derive the best estimates ever obtained for the spectrum and large-scale isotropy of the 0.7–10 keV CXB. Preliminary ASCA results on the CXB, using the SIS data, have already been published by Gendreau et al. (1995), in which the author of the present thesis is included as a co-author. In this thesis, on the contrary, we concentrate on the GIS data for the two reasons. One is that the GIS covers the entire XRT field of view of ~ 40′ diameter, whereas the SIS has a smaller field of view of 20′ × 20′. The other reason is that the author belongs to the GIS team, and has deeply contributed to the development, pre-launch tests, in-orbit calibration, and software development for the GIS project. All these efforts provide a valuable basis for the CXB investigation, and will constitute an important part of the present thesis.

The present thesis is arranged in the following way. In Chapter 2, we review essential properties of the CXB, and in Chapter 3 we describe the ASCA spacecraft and its instruments. Chapter 4 summarizes those efforts of instrumental calibrations that are relevant to the CXB study, and that have been contributed significantly by the auther himself. We give in Chaper 5 a brief description of how the 10 sample fields were observed. In Chapter 6 we carry out a pilot study of the average CXB spectrum for one of the sample fields called LSS, although the effect of point sources is still included. Chapter 7 is devoted to our main effort of removing point sources and quantifying the properties of the remaining CXB for all the sample fields. There, we show that the CXB spectrum in the 1.5-10 keV range can be described with a single power-law of $\Gamma = 1.44 \pm 0.06$, and the field-to-field brightness anisotropy is at most 9.2% (90% confidence level) after removing point sources with 2–10 keV fluxes above $\sim 2 \times 10^{-13}$ erg cm^{-2} s^{-1}. Finally, we discuss these results in Chapter 8.

In closing this chapter, we remark that two related thesis works are in progress using the ASCA data. These are the thesis work by Ueda (1996) who is studying the source number counts in the laregest continuous sky area (called LSS) covered with ASCA, and that of Ogasaka (1996) who analyzes source counts in the deepest sky region (caled SA57) observed with ASCA. The three thesis works utilize partially overlapping ASCA data base, but are fully independent of, and complementary to, one another.

Chapter 2

Review of the Cosmic X-ray Background

2.1 Spectral properties of the CXB

2.1.1 CXB spectrum above 2 keV

In early days of the X-ray astronomy, the CXB energy-flux specrum $I(E)$ was expressed with a broken power-law as (Schwartz and Gursky 1974)

$$I(E) = \begin{cases} 1.36 \times 10^{-8}\, E^{-0.40} & (1 \le E \le 21 \text{ keV}) \\ 2.68 \times 10^{-7}\, E^{-1.38} & (21 < E \text{ keV}) \end{cases} \quad \text{erg cm}^{-2}\,\text{s}^{-2}\,\text{str}^{-1}\,\text{keV}^{-1}, \tag{2.1}$$

where E is the X-ray photon energy in unit of keV. The energy index of 0.4 below 21 keV is equivalent to the photon index $\Gamma = 1.4$ mentioned in §1.1.

Later, observations with the HEAO-1 mission showed that the CXB spectrum in the 3–100 keV range can be expressed in a single form as

$$I(E) = 9.0 \times 10^{-9} \left(\frac{E}{3\text{ keV}}\right)^{-0.29} \exp\left(-\frac{E}{40\text{ keV}}\right) \quad \text{erg cm}^{-2}\,\text{s}^{-2}\,\text{str}^{-1}\,\text{keV}^{-1} \tag{2.2}$$

(figure 2.1; Marshall et al. 1980; Rothschild et al. 1983; Boldt 1987) which is essentially identical to the thermal bremsstrahlung spectrum with temperature $kT = 40$ keV. In the 2–10 keV range, equation (2.1) and equation (2.2) are consistent within measurement errors.

By integrating these equations, the 2–10 keV CXB surface brightness becomes

$$F_{\text{X}}^{2\text{–}10\,\text{keV}} = 5.6 \times 10^{-8} \quad \text{erg cm}^{-2}\,\text{s}^{-1}\,\text{str}^{-1}\,. \tag{2.3}$$

Therefore, by integrating over the whole sky, the 2–10 keV CXB energy flux becomes 7×10^{-7} erg cm^{-2} s^{-1}, a value quite close to that of Scorpius X-1 that is usually by far the brightest object on the X-ray sky.

2.1.2 Lack of inerse-Compton effects

As already mentioned in §1.1, the agreement of the CXB spectrum of equation (2.2) with the $kT = 40$ keV bremsstrahlung has naturally inspired a set of theoretical models

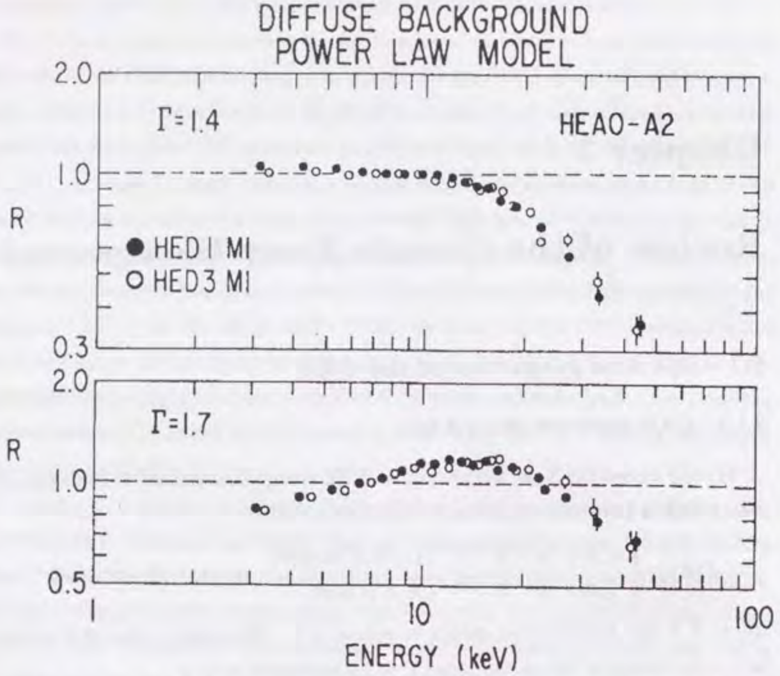

Figure 2.1: The 3–50 keV CXB spectrum observed with HEAO-1 A2, adopted from Boldt (1987). The ratio (R) of the observed CXB counts to that predicted by convolving, with the detector response, power-law spectra of photon indices $\Gamma = 1.4$ (upper panel) and $\Gamma = 1.7$ (lower panel) are plotted against energy.

which consider the CXB as thermal emission from hot diffuse plasmas of cosmological scales (Hoyle 1963; Cowsik & Kobetich 1972; Field & Perrenod 1977). Such hot plasmas, if distributed with a uniform density n_e which is high enough to account for the CXB brightness, would distort the CMB spectrum to a measurable degree. This occurs when the CMB photons, while traveling to us along a path lenght s, get inverse-Compton scattered off the high energy electrons in such plasmas (Zeldovich and Sunyaev 1969). The degree of this Zeldvich-Sunyaev effect can be parameterized by so-called Compton y-parameter, i.e., a dimension-less quantity defined as

$$y = \int d\tau_e \cdot \frac{k(T_e - T_\gamma)}{m_e c^2}, \tag{2.4}$$

where T_e, T_γ and $\tau_e = \int n_e \sigma_e ds$ are the electron temperature of the plasma, the CMB photon temperature, and the optical depth for the inverse-Compton scattering; σ_e denotes the cross section of inverse-Compton scattering.

The high-precision measurements with the Absolute Microwave Spectrometer onboard the Cosmic Background Explorer (COBE) showed that the CMB spectum agrees with a blackbody spectrum of 2.74 K with an amazing accuracy (up to 0.01%; Mather et al. 1990, 1994). The derived limit on the Comptonization effiect is as stringent as $y < 2.5 \times 10^{-5}$, and the implied high-temperature plasma density can account for at most 0.01% of the CXB brightness. Thus, the hot plasma model for the CXB has apparently ruled out.

We must however keep in mind that the story becomes quite different when the plasma is distributed inhomogeneously, in the form of blobs or filaments. When the volume filling factor of the assumed hot plasma is as small as $< 10^{-3}$, there is a solution for the plasma density that is consistent with both the COBE limit and the CXB brightness (Mineshige and Tajima, private communication).

2.1.3 CXB spectrum below 2 keV

The diffuse X-ray background below 2 keV has been studied with ROSAT, as well as with previous rocket experiments by many groups including Leiden-Nagoya, ISAS (Institute of Space and Astronautical Science; Inoue et al. 1979), and University of Wisconsin. These results are summarized by Tanaka and Bleeker (1977), McCammon et al. (1983), and McCammon and Sanders (1990). Among these experiments, the Japanese K-10-13 rocket experiment (Inoue et al. 1979) is of particular meaning for us, because it provided the startpoint for the gas scintillation proportional counter technique in Japan, which later developed into Tenma GSPC (Koyama et al. 1984) and finally into the ASCA GIS.

In contrast to the simple CXB spectrum above 2 keV (§2.1.1), the CXB properties are much more complex below 2 keV, since there are strong contributions from various Galactic emission components (of mostly thermal nature) as well as effects by the Galactic photoelectric absorption; naturally, the brightness becomes highly anisotropic (appendix G). In so called Carbon band below 0.28 keV, which is the lowest window of the cosmic X-ray observations, the sky is dominated by thermal emission from "Hot Bubble" surrounding the solar system, i.e. an ionized region of temperature (1–2) × 10^6 K (0.1–0.2 keV) presumably created by an ancient supernova explosion.

In the energy range between 0.28 keV and ~ 1 keV, Galactic emission components of somewhat larger scales becomes dominant. These include the $kT \sim 0.2$ keV emission associated with a high-latitude Galactic structure called Loop I or North Polar Spur (figure G.4), and the $kT \sim 0.6$ keV soft component (Kaneda et al. 1996, private communication) of so-called Galactic ridge emission (Koyama et al. 1986) which is seen along the Galactic plane.

In adition to these Galactic components and the truly *cosmic* hard ($\Gamma = 1.4$) emission,

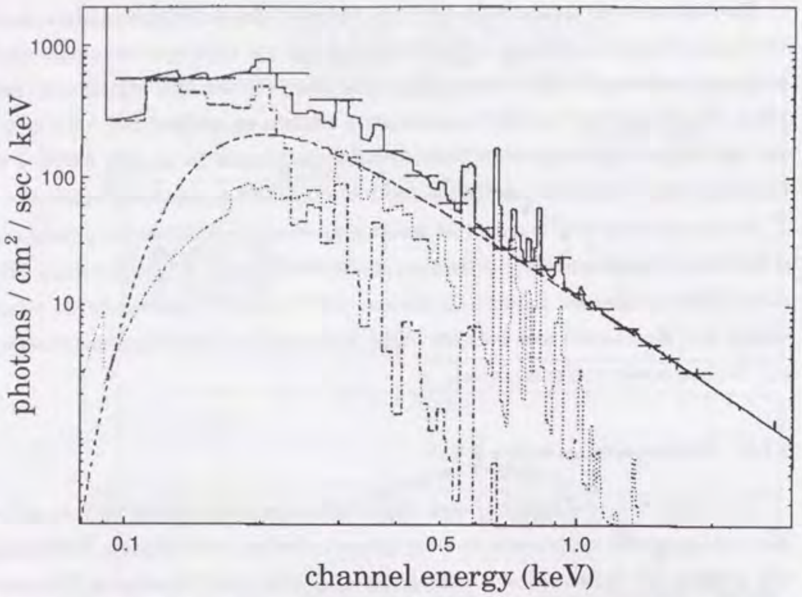

Figure 2.2: The 0.1–2 keV CXB spectrum observed with ROSAT PSPC, adopted from Hasinger (1992); three-component fit to the total background in the HZ43P field: a 10^6 K thermal plasma, a 2–3 × 10^6 K thermal plasma, and a power-law of $\Gamma \sim 2.2$ for the higher energies.

there is yet another CXB component revealed by ROSAT (figure 2.2; Shanks et al. 1991; Hasinger et al. 1993); as mentioned in §1.1, it is seen as an excess above the hard component in a relatively narrow energy range around 1 keV, where the Galactic components and the hard component cross over. It has a steeper ($\Gamma \sim 2.1$) slope, yet it may be quite isotropic. We have at least four different and mutaually non-exclusive explanations for this enigmatic intermediate component in the CXB, and at present, we can either prove or disprove none of these possibilities:

1. It may be an intrinsic feature of the hard CXB component, produced by the same population of cosmological objects. The soft excess of AGNs is one such possibility.
2. It may be a cosmological phenomenon, but produced by objects of different population (e.g. clusters of galaxies, normal galaxies, etc.) than those responsible for the hard CXB component.
3. It may be a Galactic component (e.g. a thermal halo associated with the Milky Way) with a very large scale height.

4. It may be thermal emission from a hypothesized plasma halo gravitationally bound by the potential of Local Group (a poor galaxy group including our own Galaxy, M31, M33, and so on). This has been conjectured by Makishima (1995, a private communication) and evaluated by Suto et al. (1996).

2.2 Brightness distribution of the CXB

2.2.1 Small-scale fluctuations

The CXB brightness above 2 keV is highly isotropic. However, the CXB is at least partially made up of discrete sources, and each "blank sky" field in fact includes a number of X-ray sources which are individually too faint to be *detected* or *resolved*. Since the number of these faint discrete sources in the f.o.v. statistically fluctuates, a certain level of field-to-field fluctuation is always seen in the CXB intensity when many "blank sky" regions are observed with an X-ray instrument with a field of view Ω_e. Assuming that the source distribution is isotropic, we expect that the relative CXB fluctuation scales as $\Omega_e{}^{-0.5}\ S_c{}^{0.25}$, where S_c is the detection threshold of that particular instrument. Therefore, the narrower the field of view is, the larger the relative fluctuation becomes.

Using a 3° × 3° beam width of the HEAO-1 A2 experiment, Shafer (1983) derived a 3% upper limit on the beam-to-beam relative CXB fluctuation. Later, Hayashida (1990) employed the 1° × 2° beam of the Ginga LAC, and showed that the rms fluctuation in the CXB intensity is of order 5% in the 2–20 keV after excluding sources brighter than $\sim 1 \times 10^{-11}$ erg cm^{-2} s^{-1}.

Then, what can we learn from these fluctuation levels? If we assume that the CXB fluctuation is totally caused by the statistical fluctuation in the number of unresolved sources in the f.o.v., we can put constraints on the $\log N$-$\log S$ relation (see §2.3 for detail) of discrete sources towards flux levels lower than the detection threshold. Actually, Hamilton & Helfand (1987) analyzed the Einstein data from this point of view, and Shafer & Fabian (1983) analyzed HEAO-1 A2 data. Hayashida (1990) applied this technique to his Ginga data, and estimated the $\log N$-$\log S$ relation down to a flux level of $\sim 1 \times 10^{-13}$ erg cm^{-2} s^{-1} in the 2–10 keV energy band. His estimate has been directly confirmed to be correct by the subsequent ASCA observations (Ueda 1996; Ogasaka 1996), implying that the CXB fluctuation observed with Ginga was indeed caused by the statistics of faint source numbers.

If we can somehow have an *a priori* estimate of the $\log N$-$\log S$ relation below the detection threshold (e.g. by estrapolating the $\log N$-$\log S$ relation from the larger flux ranges, or using deeper observations with the same instrument, or utilizing information in

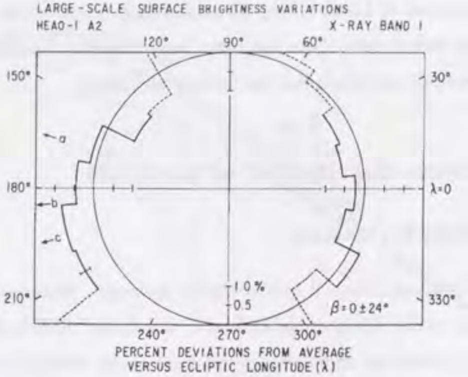

Figure 2.3: The dipole anisotropy of the CXB observed with HEAO-1 A2 all-sky survey, adopted from Boldt (1987); percentage deviations from isotropy (represented by the circle) for the average surface brightness near the ecliptic plane ($\beta = -24° \rightarrow +24°$) as a function of ecliptic longitude (λ). The 1σ error bar shown corresponds to photon counting statistics. Special directions indicated are for the CMB anisotropy results of (a) Smoot et al. (1977), (b) Cheng et al. (1979), and (c) the longitude where the supergalactic plane crosses the ecliptic equator. Surface brightness deviations for those ecliptic longitudes close to the galactic equator (i.e. near $\lambda = 89°$ and $\lambda = 269°$) are indicated with dashed lines.

other wavelengths), we can compare the observed field-to-field CXB fluctuation with what is predicted by the $\log N$-$\log S$ relation. If the observed fluctuation is much larger, we can infer that there is some sort of large-scale spatial structure in the CXB source (e.g. large-scale clustering of the quasars). On the contrary, if the fluctuation is significantly smaller than is expected, it is suggested that the CXB is contributed by something other than discrete celestial objects (e.g. hot plasmas with extremely low filling factor; see §2.1.2).

2.2.2 Global isotropy and dipole anisotropy

Except for the statistical fluctuation mentioned in the previous subsection, the CXB brightness is highly isotropic on the large scale. According to the HEAO-1 A2 result (figure G.2), the large-scale CXB anisotropy is less than 3%. Hayashida (1990) failed to detect any lareg-scale correlation in the Ginga fluctuation analysis.

However, a dipole anisotropy in the CXB brightness has been detected with the HEAO-1 A2 all-sky-survey (figure 2.3; Shafer 1983; Shafer & Fabian 1983). The dipole amplitude of ~ 0.5%, together with its direction, are roughly consistent with the dipole anisotropy in CMB (Smoot et al. 1977). Both these dipole effects are thought to arises from solar system's proper motion with respect to the Hubble flow.

Possible correlation of the CXB with any Galactic feature (e.g. Galactic quadrupole component, Galactic latitude dependence, and so on) is another subject of interest. For example, Koyama (1989), using the Tenma GSPC, suggested the presence of a $kT \sim 10$ keV diffuse thermal Galactic emission with an extremely low surface brightness, extending up to high galactic latitudes. Such components would show up in the CXB data. However Hayashida (1990) did not find any Galactic latitude dependence in the Ginga CXB intensity. At present, there is no evidence of the *real* CXB above ~ 2 keV correlating with any Galactic feature. This demonstrates the extra-Galactic nature of the CXB.

2.3 Contribution of known classes of discrete sources

2.3.1 Log$N$ - Log$S$ relations above 2 keV

So called $\log N$-$\log S$ relation describes the source number density as a function of source flux in a fixed energy range (in the observer frame). This gives one of the most straightforward way of testing the hypothesis that the CXB is a superposition of numerous discrete sources. Accordingly, the $\log N$-$\log S$ relation has been measured repeatedly with many X-ray experiments, both imaging and non-imaging.

The $\log N$-$\log S$ relation above 2 keV have so far been derived with non-imaging experiments, including UHURU (Schwartz 1979), Ariel V (Warwick & Pye 1978), HEAO-1 A1 (Wood et al. 1984), HEAO-1 A2 (Piccinotti et al. 1982; Shafer 1983), and Ginga LAC (Hayashida 1990; Kondo 1991). These results are summarized in figure 2.4, and they consistently indicates an apparently Euclidian $\log N$-$\log S$ relaion

$$n(S) = (2.2^{+0.3}_{-0.2}) \times 10^{-15}\, S^{-2.5}\ \mathrm{str}^{-1}, \tag{2.5}$$

(Piccinotti et al. 1983) where $n(S)$ is the differential source number density with the 2–10 keV flux S which is given in unit of erg cm^{-2} s^{-1}.

2.3.2 Log$N$ - Log$S$ relations below 2 keV

The $\log N$-$\log S$ relation below 2 keV was first derived with the Einstein observatory through Deep Survey (Giacconi et al. 1979; Primini et al. 1991), and Extended Medium Sensitivity Survey (EMSS; e.g. Gioia et al. 1990; Stocke et al. 1991). These results are shown in figure 2.5. The integral $\log N$-$\log S$ relation of the serendipitously discovered object in the EMSS survey can be expressed as

$$N(>S) = 2.68 \times 10^{-19}\, S^{-1.48\pm0.05}\ \mathrm{str}^{-1}, \tag{2.6}$$

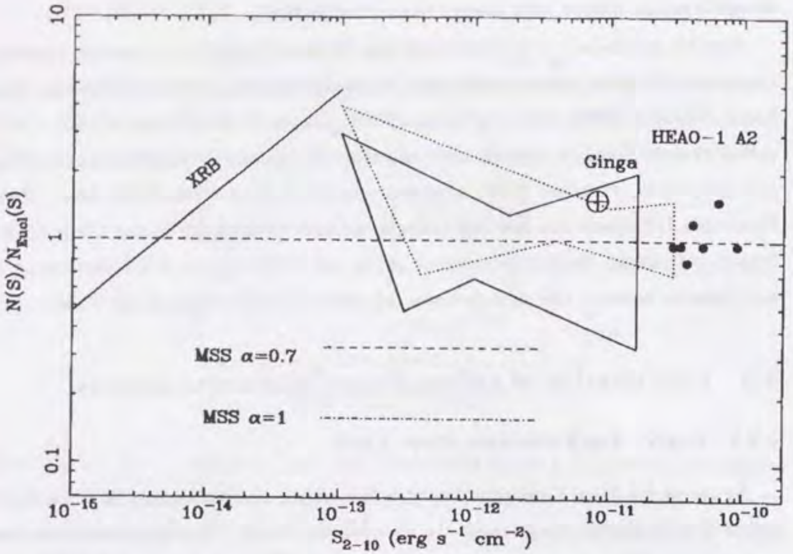

Figure 2.4: The integral $\log N$-$\log S$ relation in the 2–10 keV energy band normalized to that expected in a Euclidean universe, adopted from the review by Fabian & Barcons (1992). The filled circles are from the direct counts of Piccinotti et al. (1982). The dotted contour is the 1σ region from the HEAO-1 A2 fluctuation analysis (Shafer & Fabian 1983), the solid contour from the Ginga fluctuation analysis (Hayashida 1990). The lines marked MSS show the results from the Extended Medium Sensitivity Survey (Gioia et al. 1990) after converted into the 2–10 keV range assuming several spectral indices. The cross represents direct counts from Ginga scans (Kondo 1990). The solid line labeled XRB indicates the level at which 100% of the CXB brightness can be explained.

where S is the 0.3–3.5 keV flux in unit of erg cm^{-2} s^{-1}. At the flux limit of $\simeq 5\times10^{-14}$ erg cm^{-2} s^{-1} in the 0.3–3.5 keV band achieved with the Einstein Deep Survey, it was suggested that 16–25% of the CXB was resolved into discrete extragalactic objects (Primini et al. 1991).

Using a deep ROSAT exposure, Hasinger et al. (1993) derived a $\log N$-$\log S$ relation, as shown in figure 2.5, down to a flux limit of $\simeq 3\times10^{-15}$ erg cm^{-2} s^{-1} in 0.5–2 keV. At this level, nearly 50% of the 1–2 keV CXB has been resolved into discrete objects. Fluctuation analysis of the ROSAT data (Hasinger et al. 1993) implies nearly 75% of the CXB to be originate in the discrete sources. Also the $\log N$-$\log S$ relation is suggested to deviate from the Euclidian below $S\sim10^{-14}$ erg s^{-1} cm^{-2}.

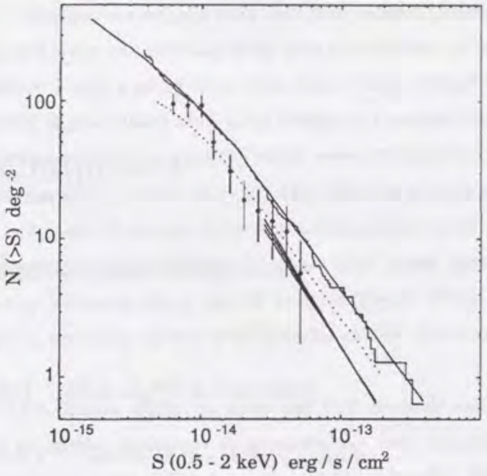

Figure 2.5: The integral $\log N$-$\log S$ relation in the 0.5–2 keV energy band, adopted from Hasinger (1992); ROSAT $\log N$-$\log S$ relation (histogram and solid line) compared to the EMSS (two crossing solid lines) and the data of Shanks et al. (filled circles). Note that the contribution of brighter fluxes has not been added to the latter data.

It has been a matter of considerabale controversy whether the $\log N$-$\log S$ relations derived above and below 2 keV are consistent or not. Since the energy ranges are different, we must assume the source spectrum (specifically the power-law spectral slope) when converting one to the other. When this conversion is done assuming $\Gamma = 1.7$ (figure 2.4), we see a hint of factor 2–3 discrepancy in the sense that the soft-band $\log N$-$\log S$ relation comes in short of the hard-band one, although almost consistent if $\Gamma = 1.4$. This is considered to be an evidence for a possible abundance of hard-spectrum (possibly highly abosrbed) objects. The issue is currently being investigated with ASCA by Ueda (1996) and Ogasaka (1996).

2.3.3 The spectral paradox

Here we review the issue of "spectral paradox" mentioned in §1.2. In the 2–20 keV energy band, type 1 Seyfert galaxies, which form a typical class of AGNs in the universe where redshift is $z \lesssim 0.1$, show an approximately power-law spectrum of $\Gamma = 1.7$ (e.g. Turner and Pounds 1989). Radio-loud and radio-quiet quasars, which represent more distant AGNs, have $\Gamma \sim 2.0$ and ~ 1.6, respectively (Williams et al. 1992). Furthermore, the AGN spectra below 2 keV are generally known to become steeper than those found at higher energies, and $\Gamma \sim 2.3$–2.5 are reported for quasars obtained by the ROSAT all sky survey (Schartel et al. 1994). All these AGN spectra are steeper than the CXB spectrum.

Other celestial objects, such as individual galaxies and clusters of galaxies, generally have still softer spectra because their emission is predominantly of thermal nature. Therefore, it is impossible to synthesize the CXB spectrum from these objects with steeper spectral slopes, and some population of sources with very hard spectra are required.

As mentioned in §1.2, one possible candidate for such hard-spectrum sources is heavily obscured AGNs, such as a type 2 Seyfert galaxy which is thought to be a type 1 Seyfert galaxy seen along the cold gas disk feeding the central balck hole (Antonucci & Miller 1985). In such objects, X-rays from the central power house exhibit a strong photoelectric absorption presumably by the gas disk, as revealed with Ginga observations (Koyama et al. 1989; Awaki et al. 1990; 1991). Since the absorption makes the spectra of these objects extremely hard in the 2–20 keV energy reange, they can be utilized efficiently to synthesize the CXB spectrum (Fabian et al. 1990). Therefoe, quest for the highly absorved qusars is an important issue to be explored with ASCA, although it is outside the scope of the present thesis.

One issue relevant to the present thesis is that the obscured AGNs usually exhibit very intense fluorescence Fe-K emission lines, sometimes with equivalent widths up to 2 keV (e.g. Fuakazawa et al. 1994). Therefore, if the obscured AGNs are a significant CXB constitutent, we expect to see a trace of Fe-K lines in the CXB spectrum, Although the Fe-K lines must be quite smeared out due to superposition of sources with different redshifts.

Another issue is that a heavily obscured AGN often shows a spectrum which is steeply cut-off below ~ 4–5 keV by absorption (figure 2.6). If such objects are at a redshift of $z = 1$–3, the cut-off feature will be shifted into an observer energy range of 1–2.5 keV. Therefore, the precise spectral measurement of the CXB in this energy range is extremely important to constrain various models which try to synthesize the CXB spectrum invoking obscured AGNs. Note that the CXB spectrum in this range has remained poorly understood, since previous non-imaging experiments did not have sufficient sensitivity, or sufficient energy resolution to clearly separate the Galactic component. Similarly, soft X-ray telescopes (Einstein, ROSAT) did not have sufficient sensitivity or spectral resolution to firmly fix the $\Gamma = 1.4$ hard component.

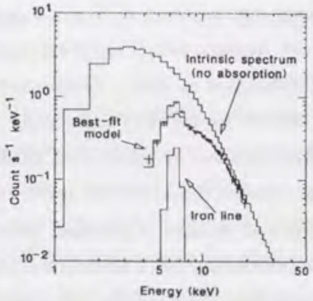

Figure 2.6: Type 2 Seyfert galaxy Mkn3 spectrum (crosses) observed with Ginga LAC, adopted from Awaki et al. (1990). The histograms show the best-fit model (absorbed power-law; $\Gamma = 1.3 \pm 0.3$, $N_{\rm H} = 6^{+3}_{-2} \times 10^{23}$ cm^{-2}, $L_{\rm X}^{2-10\,{\rm keV}} = 4 \times 10^{43}$ erg s^{-2} at a distance of 79 Mpc with $z = 0.0132$) and the intrinsic spectrum of Mkn3 without absorption.

Chapter 3

Instrumentation

3.1 The ASCA satellite

3.1.1 Launch of the ASCA satellite

The scientific satellite ASCA (Advance Satellite for Cosmology and Astrophysics), previously called ASTRO-D, is a project of the Institute of Space and Astronautical Science (ISAS), developed under a Japan-US collaboration (Tanaka et al. 1994). Following Hakucho (1979), Tenma (1983) and Ginga (1987), ASCA is the fourth Japanese satellite devoted to the cosmic X-ray investigations. ASCA has been launched successfully into orbit on 20 February 1993 at 11 a.m. JST, using the three-stage solid-propellant M-3SII-7 rocket, from Kagoshima Space Center (KSC) of ISAS at Uchinoura, Kagoshima. ASCA has achieved a near-circular orbit with a perigee of 520 km, an apogee of 625 km, and an inclination of 31°. ASCA makes about 15 revolutions per day around the Earth, five out of which pass over Japan.

Figure 3.1 shows the in-orbit configuration of ASCA. It weighs 420 kg, and has an octagonal-shaped body of a diameter 1.2 m where six solar panels are attached. The spacecraft has a nested double-cylinder structure, with the outer cylinder serving as the spacecraft body while the inner cylinder serving as an extendible optical bench (EOB). During the launch, the EOB is retracted inside the outer cylinder, and the solar panels are folded around it, so that the entire spacecraft is contained inside the nose fairing of the launch vehicle. Following the launch, the solar panels were successfully deployed on February 25, to ensure the electric power generation up to 490 W. Then the EOB was successfully extended on March 3. Further details of ASCA are given in Tanaka et al. (1994).

At the top of the EOB, four sets of identical imaging X-ray Telescopes (XRTs) are placed. They are all aligned along the satellite Z-axis with a common focal length of 3.5 m. Compared with X-ray telescopes of previous X-ray satellites, the ASCA XRT

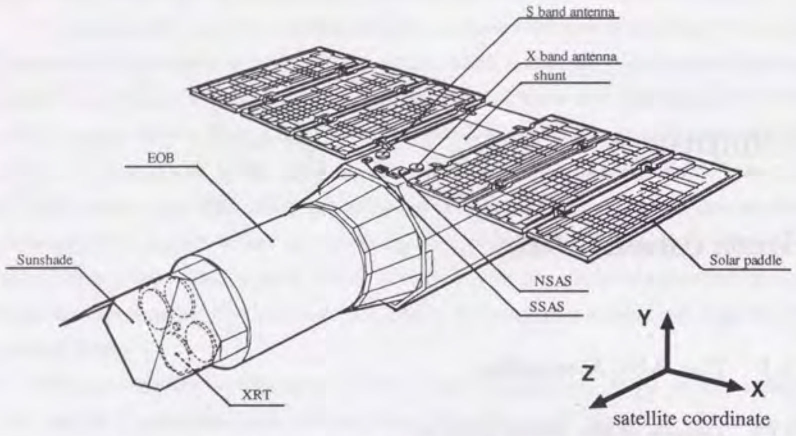

Figure 3.1: In orbit configration of the ASCA satellite

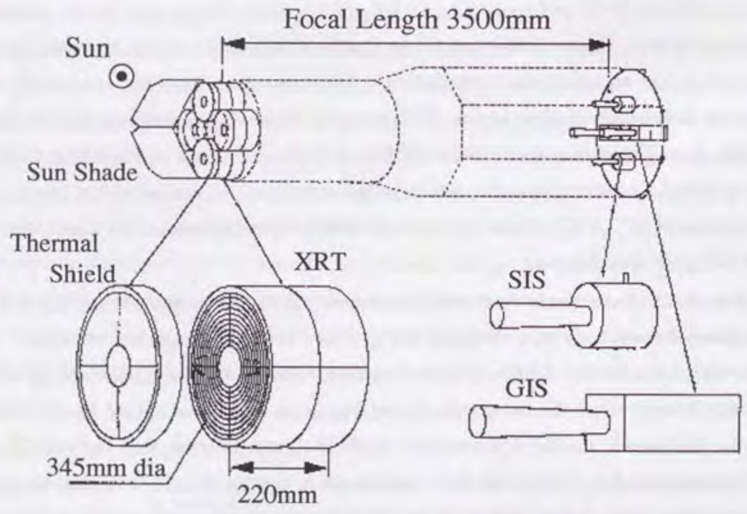

Figure 3.2: Onboard instruments of the ASCA satellite

has a much larger throughput and a drastically wider energy band up to 10 keV (see §3.2). As illustrated in figure 3.2, the focal planes of the XRTs are equipped with four position-sensitive X-ray detectors; two SIS (Solid-state Imaging Spectrometer) detectors called SIS0 and SIS1, and two GIS (Gas Imaging Spectrometer) detectors called GIS2 and GIS3. Each detector is coupled to a fixed XRT, and the four telescope-detector systems acquire data simultaneously for the same target. Both the GIS and the SIS have unprecedent spectral resolutions as well as adequate position resolutions. We describe the XRT, the SIS, and the GIS in §3.2, §3.3 and §3.4, respectively.

3.1.2 Attitude control and attitude determination system

During normal observations, the space craft Z-axis (ref. figure 3.1), along which the XRTs are aligned, is pointed at the target. This can be achieved by an onboard closed loop formed by attitude actuators, attitude sensors, and a CPU-based attitude control processor. The actuators consist of four bias momentum reaction wheels (RW) and three-axis magnetic torquers (MTQ). The attitude sensors include dual star trackers (STT), sun sensors (SSAS and NSAS), three-axis geomagnetic sensors (GAS), and five redundant gyros (IRU). The absolute pointing accuracy is typically 1 arcmin, and the attitude stability is of a similar order. Once the satellite data are transmitted to ground, off-line analysis of the signals from the attitude sensors affords an accurate *post factum* attitude solution up to an accuracy of ~ 1 arcmin.

Changes of the Z-axis pointing direction, called maneuvers, can be done in a semi-automated way, with a typical speed of 5 seconds per degree. ASCA can attain any attitude on condition that the Y-axis direction (ref. figure 3.1) remains within 30° from the Sun to ensure a sufficient power generation by the solar cells. To save the time loss during attitude changes, the maneuvers are performed with a typical frequency of once or twice a day. Therefore each target is observed typically for half a day to one day. However net exposure to the target remains only 50–70% of this gross pointing duration, because useable data cannot be accumulated during passages through regions of high particle background (especially the South Atlantic Anomaly, or SAA), or during the periods when the target is behind the Earth.

3.1.3 Satellite operation and data transfer

We can contact ASCA from KSC five times a day, each lasting for 10–12 minutes. All the necessary commanding must be done during these five contacts. The CPU-based onboard commanding unit keeps control of the satellite all the time, by handling a large number of commands with a given interval, according to the command program which is loaded to the spacecraft from the KSC. The program loading is done typically once a day.

The observed data (~ 75% scientific and ~ 25% house keeping) are stored in the onboard data recorder (BDR) using magnetic bubble memory of 128 Mbits capacity. The data acquisition rate is commandable at either 32 (high bit-rate), 4 (medium bit-rate), or 1 kbit/s (low bit-rate). Therefore the BDR becomes full in 1 h 8 m 16 s, 9 h 6 m 8 s, and 36 h 24 m 32 s, in high, medium, and low bit-rate, respectively. In order to continue observations, the stored data must therefore be transmitted to ground via down-link telemetry with a sufficient frequency. It takes 8 m 32 s, and this can be done during passes over the KSC, as well as the US NASA's Deep Space Network (DSN) stations at Canberra, Goldstone, Madrid, Wallaps, and Santiago. The BDR is "played back" typically 10 times a day, thus yielding a daily total of about 1 Gbits of data. Data received at KSC and the DSN stations are transfered to the Sagamihara Space Operation Center (SSOC) of ISAS and stored in a data base. The data is supplied to observers after the attitude determination of the satellite and converting the format into FITS files.

3.1.4 Early operations and observation program

Various common instruments onboard ASCA were turned on, one after another, during the first 2–3 weeks after the launch. In particular the attitude control system has been fully activated, and the spacecraft has achieved the three-axis-stabilized attitude. Spending almost the entire March of 1993, we gradually ran up the four focal plane instruments.

From late April 1993 ASCA entered PV (Performance Verification) phase, which has twofold objectives. One is to exercise various sort of observations to verify and further calibrate the performance of ASCA. The other is to explore scientific capability of ASCA by observing important and attractive objects. The PV-phase data are shared by the entire ASCA team for 1.5 years before they become open to public.

From October 1993, the first round of guest observation phase (GO-1) started; the observation is carried out based on scientific proposals, which are submitted from public to either Japan or US, to get evaluated and accepted by respective committees. After GO-2 (since June 1994) and GO-3 (since November 1994), the fourth GO-phase (GO-4) is going on from December 1995 for one year. In the GO phase, 60% of the total observing time is allotted to the "Japan only" plus "Japan-ESA (European Space Agency)" observations, 25% to the "joint Japan-US" observations, 10% to the "US only" observations, and the remaining 5% is reserved for maintenance and contingency.

For practical reasons, all the targets to be observed (during both PV- and GO-phases) are categorized into seven subfield. These are; stars (including cataclysmic variables), X-ray binaries, supernova remnants (SNRs), galaxies (including our Galaxy), clusters of galaxies, active galactic nuclei (AGNs), and cosmic X-ray background (CXB). Experience through the PV phase has demonstrated that ASCA is capable of innovating our knowledge in all these subfield.

3.2 X-ray telescope (XRT)

The X-Ray Telescope (XRT) onboard ASCA was developed jointly by NASA/GSFC, Nagoya University, and ISAS. It has for the first time enabled cosmic X-ray imaging studies above X-ray energies of a few keV up to about 10 keV (Selemitsos et al. 1995; Tsusaka et al. 1995).

3.2.1 Principle of X-ray telescopes

Soft X-rays are totally reflected off a smooth surface, when their incident angle measured from the surface is shallower than a certain critical value. This phenomenon is known as grazing-incidence reflection. The critical angle, typically of order 1 degree or so, is inversely proportional to the X-ray energy and increases with increasing free electron density of the reflecting material.

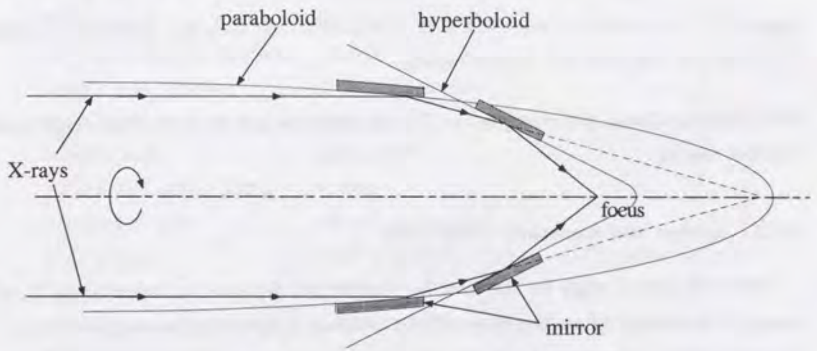

Figure 3.3: Walter type I optics

X-ray telescope mirrors use this mechanism usually in so called Wolter type I configuration (Fig.3.3), which employs paraboloid and hyperboloid surfaces as the primary and the secondary mirrors so as to remove the first-order abberation. The two mirrors have a common focus and reflect X-rays in series (double reflection). This Walter type I optics have been used for many X-ray astronomy satellites, including the X-ray telescope onboard the USA's Einstein Observatory (HEAO-B; 1978–1981), the Low-Energy Telescope onboard the European EXOSAT mission (1983–1986), the main and sub telescopes onboard the joint German/UK/US ROSAT mission (1991–), and the US-made Soft X-ray Telescope onboard the Japanese solar observatory Yohkoh (1991–).

These previous X-ray telescopes have all made the reflecting shells from highly polished glass or glass ceramic, on which heavy metal (Ni, Au, etc.) is evaporated to increase the reflectivity. The effective area is usually increased by having multiple nested set of mirrors

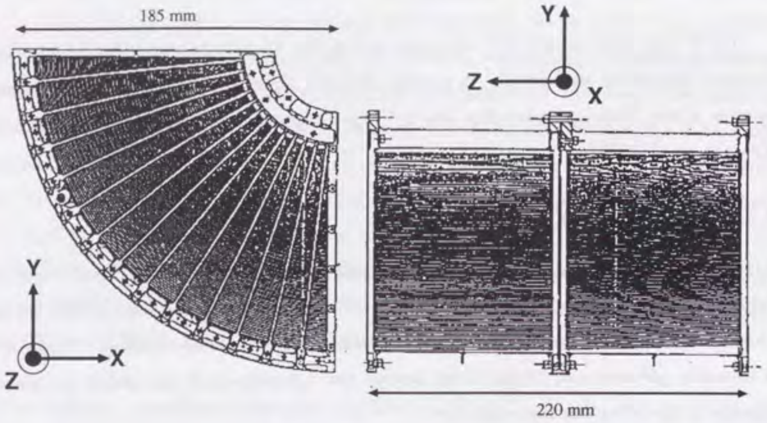

Figure 3.4: One quadrant of the ASCA XRT. The XRT is built up in four quadrants; 120 foils are ajusted by alignment bars running radially.

with a common focus. For example, the Einstein telescope and the ROSAT telescope both use four nesting.

3.2.2 Design and structure of the XRT

Since the critical angle for the total X-ray reflection decreases with increasing X-ray energy, it becomes progressively more difficult to reflect X-rays at higher energies. In order to ensure a high reflectivity for harder X-rays, we must operate the mirror shells under a very small incident angle, hence very small projected area. In order to achieve a large effective area up to higher energies, we must then increase the number of mirror nesting. This can be realized by a design called multiple thin-foil optics, a special version of the Wolter I optics. This design makes each shell extremely thin by using metal foils instead of polished glass, and drastically increase the number of nesting. However it is very difficult to shape a thin foil into a paraboloid or a hyperboloid. Thus, a conical surface is instead used as its approximation, which reduces the imaging quality. A prototype multiple thin-foil mirrors were used successfully in the BBXRT (Broad-Band X-Ray Telescope) experiment flown onboard Space Shuttle mission ASTRO-1 in December 1990. Then the technique has been applied to the ASCA XRT.

As shown in figure 3.4, the reflector shells of the ASCA XRT are all made of thin (127 μm) aluminium foils, bent in a conical form to approximate paraboloid or hyperboloid. The bent foils are $\sim$ 10 μm lacquer-coated to improve the surface smoothness, and then $\sim$ 50 nm gold-evaporated to increase the reflectivity. 120 of these foils are closely packed together in an onion-ring configuration with a typical spacing of 1 mm, to cover a large fraction of the mirror aperture. The innermost and the outermost shells have diameters of 120 mm and 345 mm, respectively. In practice, the foils are produced and packed in four quadrants, and aligned by 13 alignment bars into 14 sectors. The first and the last sector is masked because shape error is severe. Four quadrants make up the "paraboloid" section of 100 mm long, and another set of four quadrants make up the "hyperboloid" section. One XRT unit thus fabricated weighs about 9.8 kg. Design parameters and performance of the XRT are shown in table 3.1.

Table 3.1: Design parameters and performance of the ASCA XRT.

Mirror substrate	Aluminum foil (127 μm)
Mirror surface	Acrylic lacquer (10 μm) + Au (50 nm)
Mirror length	100 mm
Number of foils per quadrant	120 foils
Inner / outer diameter	120 mm / 345 mm
Focal length	3500 mm
Incident angle	0.24° - 0.7°
Total weight of four XRTs	$\sim$ 40 kg
Geometrical area	558 cm^2 / telescope
Field of view	$\sim 24'$ (FWHM at 1 keV) / $\sim 16'$ (FWHM at 7 keV)
Energy range	$\lesssim$ 10 keV
Effective area of four XRTs	$\sim$ 1300 cm^2 (1 keV) / $\sim$ 600 cm^2 (7 keV)
Half power diameter	$\sim$ 3 arcmin

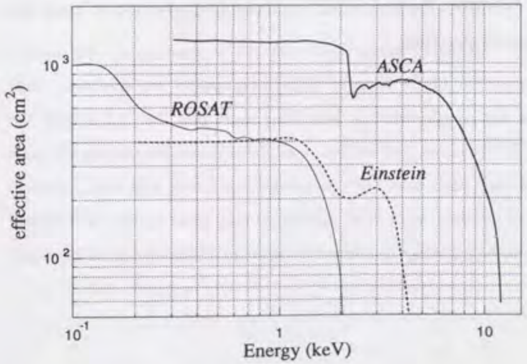

Figure 3.5: Effective area of the ASCA XRT (4 XRTs summed up, on-axis) compared with that of polished mirrors used in previous missions.

The XRT has successfully achieved a very large effective area and a wide energy range, as shown in figure 3.5. When the four units are summed up, the effective area reaches ~ 1100 cm^2 below ~ 2 keV, almost by a factor of 6 and 2 larger than those of Einstein and ROSAT respectively. A sudden drop in the reflectivity at 2.2 keV is caused by the M-edge of the gold used as reflective coating. The XRT maintains a very large reflecting area towards higher energies, e.g. ~ 600 cm^2 at 7 keV, with the upper energy bound as high as ~ 10 keV. X-ray imagery above 3–4 keV has never been achieved by polished mirrors used in previous missions. More detailed performance of the XRT will be discussed in chapter 4.

3.2.3 Alignments of four XRTs to each focal plane detector

The effective area of the XRT for X-ray reflection depends on the direction of incident X-ray, and this effect is called vignetting (see §4.2.2 for further detail). The optical axis of an XRT is defined as a line passing through the mechanical XRT center, along which the effective area is maximized. Due to possible tilt of the XRT mounting onto the satellite, the optical axes of the four XRTs point to slightly different directions. Also, centers of the four focal plane detectors (two SIS and two GIS) correspond to slight different positions on the sky due to positional displacements between an XRT and the corresponding detector. These effects give different vignetting functions to different detectors. Relationships between these positions are measured by instrument teams for the XRT, the SIS, and the GIS. These sets of information are very important for building the instrumental response, and the results are compiled as a telescope definition file (teldef file) of each detector which is registered in the calibration data base (ref. §4.2). In figure 3.6, we summarize measured positions of the detector centers in reference to that of SIS0, together with the optical axis positions projected on the focal plane. The figure also shows "nominal positions" for various observation modes, where the target source of an observation is planned to be placed. In the 1CCD mode, for example, the spacecraft attitude is controlled so that the target centers on the 1CCD nominal position.

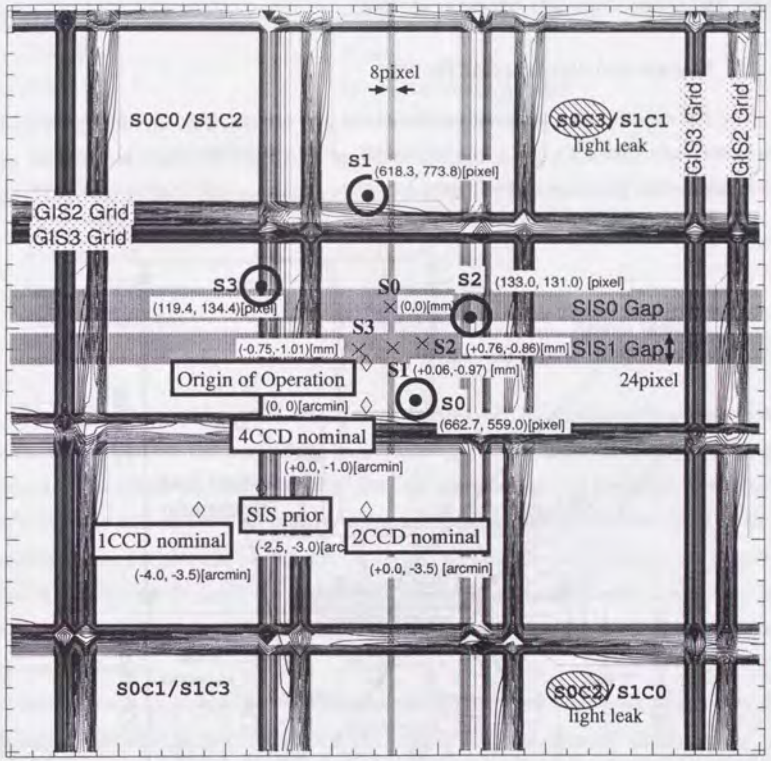
8pixel
S0C0/S1C2
S0C3/S1C1
light leak
GIS3 Grid
GIS2 Grid
S1
(618.3, 773.8)[pixel]
GIS2 Grid
GIS3 Grid
S3
(119.4, 134.4)[pixel]
S0
×(0,0)[mm]
S2
(133.0, 131.0) [pixel]
SIS0 Gap
S3
(-0.75,-1.01)[mm]
×S2
(+0.76,-0.86)[mm]
SIS1 Gap
S1 (+0.06,-0.97) [mm]
24pixel
Origin of Operation
(0, 0)[arcmin]
S0
(662.7, 559.0)[pixel]
4CCD nominal
(+0.0, -1.0)[arcmin]
SIS prior
1CCD nominal
(-2.5, -3.0)[arc
2CCD nominal
(-4.0, -3.5)[arcmin]
(+0.0, -3.5) [arcmin]
S0C1/S1C3
S0C2/S1C0
light leak

Figure 3.6: Alignment of the four focal plane detectors. Optical axes are shown by "⊙" and their positions are expressed in unit of pixel of the corresponding detectors. Detector centers are shown by "×" and their positions in reference to the center of SIS0 are given in unit of mm. Nominal positions for various observation modes (1CCD nominal, 2CCD nominal, 4CCD nominal, and SIS prior) are shown by "◇" and their positions in reference to the "Origin of Operation" are given in unit of arcmin. The gaps between the CCD chips of SIS0 and SIS1, and the support grids on the entrance windows of GIS2 and GIS3, are also superposed.

3.3 Solid-state Imaging Spectrometer (SIS)

The Solid State Spectrometer (SIS) experiment is the first X-ray detector in orbit that utilizes CCDs (charge coupled devices) in the photon counting mode. It was jointly developed by Massachusetts institute of Technology (MIT), Pennsylvania State University, ISAS, and Osaka University (Burke et al. 1991).

3.3.1 Design and structure of the SIS

The SIS experiment consists of two detectors (SIS camera; SIS0 and SIS1), an analog electronics unit (SIS-AE), and a digital processing unit (SIS-DE) which is combined with the satellite data processor (DP). Figure 3.7 shows a cross section view of the SIS camera.

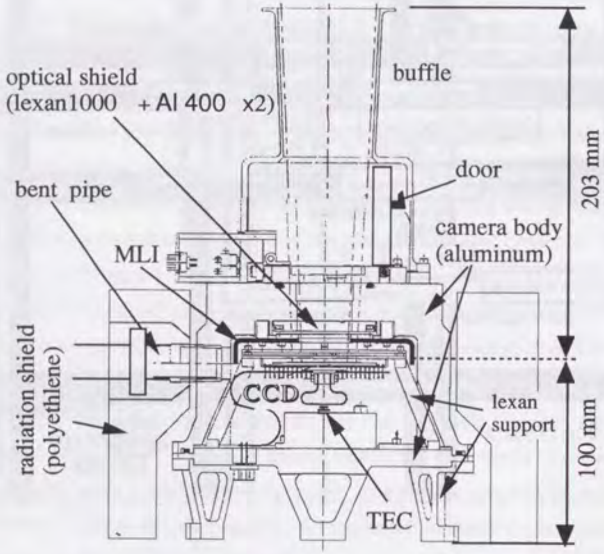

Figure 3.7: Cross section view of the SIS camera

Each SIS detector is made up of four CCD chips of 11 mm square each developed in the MIT Lincoln laboratory, to achieve a 22 mm × 22 mm square area for X-ray detection. The four CCD chips are aligned in square with narrow gaps shown in figure 3.6, to cover about $20' \times 20'$ square region on the sky. Each chip has 4096 by 4096 pixels of 27 μm square each, and a depletion layer of about 40 μm thick which ensures an improved efficiency for harder X-rays than conventional CCDs. Design parameters and performance of the SIS are summarized in table 3.2.

Table 3.2: Design parameters and performance of the SIS

Irradiation Method	Front irradiation
Charge Transfer Method	Frame Transfer
Clock	3-phase drive
Number of pixels in Image Region	420 pixels × 422 lines per chip
Pixel Size	27 μm
Area	11×11 mm square per chip
Field of View	11×11 arcmin square per chip
Thickness of Depletion Layer	$\sim$ 40 μm
Optical Blocking Filter	100 nm Lexan film coated with 40 nm aluminium
Drive temperature	~ -62 °C
Energy Band	0.4–12 keV
Quantum Efficiency	$\sim$ 80% at 5.9 keV
Energy Resolution	2% at 5.9 keV (FWHM)

The CCD chip used for the SIS is a frame transfer type CCD and has the same structure as an optical CCD of the same type. Its detection part is made of an Si semiconductor of p-type and n-type connected each other through p-n junction. An insulator layer made of SiO_2 are attached on the front surface of the n-type Si, and electrodes are built on it. By supplying specific patterns of voltages on the electrodes charges in a pixel are transfered from a pixel to a next pixel. An electrode is also attached on the back. A depletion layer is developed in the device by supplying a bias voltage between the electrodes on the front and on the back.

The aperture is covered by an optical blocking filter (100 nm Lexan film coated with 40 nm aluminium) in front of the CCD chips, in order to prevent visible lights. The whole CCDs are supported by Lexan supports and shielded from charged particles by poly-ethylene of 4 cm thick and aluminum of 1.9 cm thick at the side, aluminum plate of 3.5 cm thick at the bottom, and aluminum of 2.1 cm thickness at the top except for the aperture. A baffle is attached to shield stray light and high energy X-rays as a background.

Electric signals from the SIS camera are fed into SIS-AE and their pulse height are converted into digital signals with analog-to-digital converters. SIS-AE also generates driving clocks for the CCD chips, and monitors and controls temperature of the CCD chips. SIS-DE picks up X-ray events in the digital signals from SIS-AE with two digital signal processor (DSP) and sends them to the satellite data processor (DP), which commonly processes data from the SIS and the GIS and edits them into a telemetry format.

Figure 3.8a illustrates the quantum efficiency of the SIS as a function of incoming X-ray energy. Thus the SIS sensitivity covers approximately 0.4–10 keV. The CCD chips and preamplifiers are cooled down to −60 °C with a thermo-electric cooler (TEC) from the backside of the chips in order to reduce thermal noise down to $N \sim 5$ electrons level. Thus the SIS achieves an energy resolution of about 150 eV FWHM over the whole energy range (figure 3.8b); this is the best energy resolution ever achieved by non-dispersive X-ray spectrometers so far put into orbit.

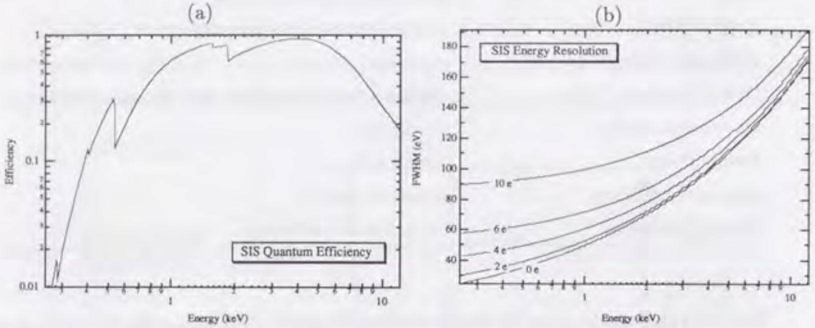

Figure 3.8: (a) Detection efficiency of the SIS as a function of incoming X-ray energy. K-edges of O (0.53keV), Al (1.56keV), and Si (1.84keV) are clearly seen in the figure. This efficiency does not includes optical blocking filter. (b) Energy resolutions of the SIS as a function of incoming X-ray energy for the single event. Energy resolutions with different read-out noise N are plotted ($N \sim 5$ for the SIS). The read-out noise levels are given as the equivalent number of electrons.

3.3.2 Data processing of the SIS

In order to perform proper photon-counting spectroscopy, the CCD frame must be scanned and read out fast enough so that event pile up (i.e. one pixel receiving more than one X-rays) is virtually negligible. Since the read out cycle is usually limited by the telemetry capacity, the SIS performs an extensive onboard CPU processing to compress the information. Instead of sending data from all the pixels to ground, the SIS basically picks up only those pixels in which the charge exceeds a certain threshold, and sends out their positions and pulse-heights. Moreover, to handle targets with different X-ray intensities and angular sizes under different telemetry rates, the SIS uses four different clocking modes; 1CCD, 2CCD and 4CCD modes. In the nCCD mode ($n = 1, 2, 4$), data from n chips for each detector are read out. In the 1CCD mode, e.g., the useable field of view becomes limited to a quarter of the detector, but the event pile up becomes least severe so that we can use slower telemetry rates and observe brighter sources than in other clocking modes.

The electrons produced in the depletion layer by an X-ray photon may be split into several adjacent pixels. The pattern of charge splitting over 3 × 3 pixels is called "event grade". When the charge is spread over more than 3 × 3 pixels, the event is rejected by the onboard CPU as a background event. In order to cope with the splitting of normal X-ray events, the SIS incorporates several data selection modes. For example, in so called "faint mode", pulse-height of a certain pixel with event detection is always accompanied with pulse-heights of the eight surrounding pixels. We can then examine the event grade on ground, and restore the total pulse-height if necessary. In so called "bright mode", the onboard CPU recognizes the charge splitting pattern, and sends only the total pulse-height for events with specified grades. The faint mode requires a larger telemetry capacity, but provides more information than the bright mode. Actually we can convert the faint mode data into the bright mode data on ground, but the reverse is impossible.

After the launch, several additional complications have been recognized with the SIS. One is so called "hot pixels", i.e. particular pixels (though not necessarily fixed ones) which report false event detections too frequently. We must carefully remove these hot pixels in data analysis. When the hot pixels become too many, the SIS data suffer from significant telemetry deadtime. The hot pixels are increasing, and it has become almost impossible to utilize 4CCD mode with the faint mode. Another problem is the light leakage, particularly in chip 2 and chip 3 of SIS0 (S0C2 and S0C3, respectively), presumably caused by a damage in the optical blocking filter. This makes the observation with S0C2 and S0C3 almost impossible when the day Earth is within ~ 25° from the target. It also affects the dark current of the whole CCDs in the daytime, and causes a subtle change in the energy to pulse-height relation. Furthermore the SIS background varies in a complicated way, depending on the SIS operation condition (clocking mode, data mode, split threshold, etc.), as well as the particle environment. There also exists a serious long-term degrading of the SIS performance due to the accumulated radiation damage (Yamashita 1995; Dotani 1995 in ASCA News No.3). These effects make the SIS observations of extended sources quite difficult. Because of these reasons, and also because of the smaller f.o.v. of the SIS, we mainly use the data from the GIS rather than the SIS in this thesis.

3.4 Gas Imaging Spectrometer (GIS)

The Gas Imaging Spectrometer (GIS) has been developed mainly by the University of Tokyo, ISAS, Tokyo Metropolitan University, Meisei Electric Co.Ltd., and Japan Radio Corporation Co.Ltd., with collaborators at Institute of Physical and Chemical Researches (RIKEN), Kyoto University (Department of Physics), NASA/Goddard Space Flight Center (GSFC), and so on (Ohashi et al. 1996; Makishima et al. 1996). The GIS design is mainly based on the GSPC experiment (Koyma et al. 1984) onboard Tenma (Tanaka et al. 1984) which was operating for 1983–1984.

3.4.1 Design and structure of the GIS

The GIS is a general-purpose X-ray imaging spectroscopy system. It consists of the two detector assemblies (GIS-S), namely GIS2 and GIS3 serving as X-ray detectors, and the main electronics called GIS-E. GIS2 and GIS3 are almost identical except that there is a Radiation Belt Monitor (RBM), a small PIN-diode particle monitor, attached to the bottom of GIS2. GIS2 and GIS3 are coupled to two of the four XRTs, and measure pulse-heights and positions of X-rays reflected by the XRTs, photon-by-photon basis. Design parameters and performance of the GIS are summarized in table 3.2.

Table 3.3: Design parameters and performance of the GIS

Energy Band	0.7–15 keV
Energy Resolution	8% at 5.9 keV (FWHM)
Effective Area	50 mm diameter
Entrance Window	10 μm beryllium
Absorption Material	Xe (96%) + He (4%), 10 mm depth, 1.2 atm at 0 °C
Positional Resolution	0.5 mm (FWHM)
Time Resolution	$\sim$ 61 μsec (Minimum in PH Mode)
	1.95 msec (Minimum in MPC Mode)

Sensor assemblies

We show the structure of GIS2 in figure 3.9. GIS2 and GIS3 are weighing 4.30 kg and 4.16 kg respectively. The small difference of the weight is because of RBM. Each sensor consists of a detector assembly and a high-voltage supply unit. Each detector assembly in turn consists of a gas cell, an imaging photo-multiplier tube (IPMT) and front-end electronics, all of which are placed in a housing made of coated magnesium-alloy with a maximum diameter 150 mm and a length of 520 mm (without RBM). We have covered the housing with tin of 0.2–0.5 mm thick and molybdenum foil of 0.1 mm thick as a shield for hard X-ray background. The top section is a hood, which limits the field of view of the GIS into the XRT direction. In order to prevent ionospheric plasmas from entering into the gas cell section, an aluminized mylar film of 540 nm thick with 37 nm of aluminum (plasma shield) is placed inside. The middle section accommodates the gas cell and the phototube, and the bottom section holds the front-end electronics.

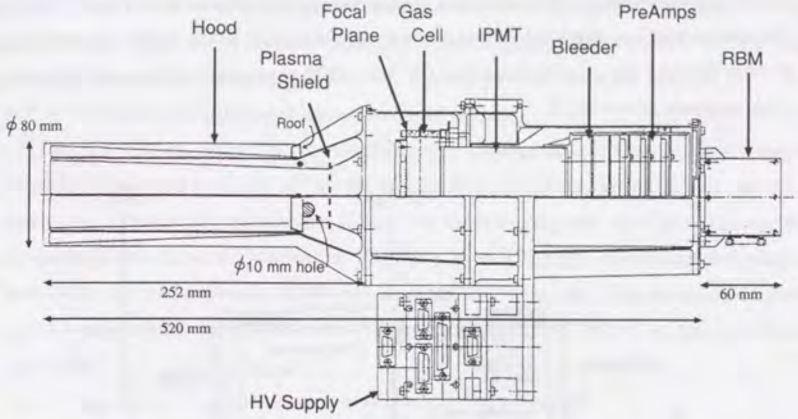

Figure 3.9: Cross section view of the GIS sensor

Gas cell as a detection part

We have developped the gas cell together with Japan Radio Corporation Co.Ltd. It is made of ceramic tube (25 mm high and 92 mm inner diameter) with a berylium entrance window and a quartz exit window, filled with a mixture of 96% xenon and 4% helium of 1.2 atm at 0 °C. Inclusion of helium is mainly to help detection of small leak with helium leak detectors. The gas is continuously purified with a small built-in getter (SAES ST172). The gas volume is divided by a mesh electrode made of molybdenum into two parts, the drift region in the top 10 mm and the scintillation region in the bottom 15 mm.

Figure 3.10 shows a schematic view of the GIS sensor system. X-rays reflected by the XRT enter through the window, whose electric potential is held at −6000 V, and are absorbed in the drift region. Through photo-ionization, primary electrons are generated on average at the rate of one electron per 21.5 eV. The electron cloud thus created slowly drifts to the intermediate mesh (−5300 keV), and then the cloud is accelerated due to the strong field toward the ground mesh which is placed in front of the quartz window. In this process, the electrons excite Xe and produce a large number of UV photons of

~ 170 nm wavelength. The excitation energy for one UV photon is ~ 10 eV. Through the quartz window, these UV photons are collected by the IPMT which measures light distribution and the overall intensity of UV flux, which is proportional to the X-ray energy with accuracy of several %.

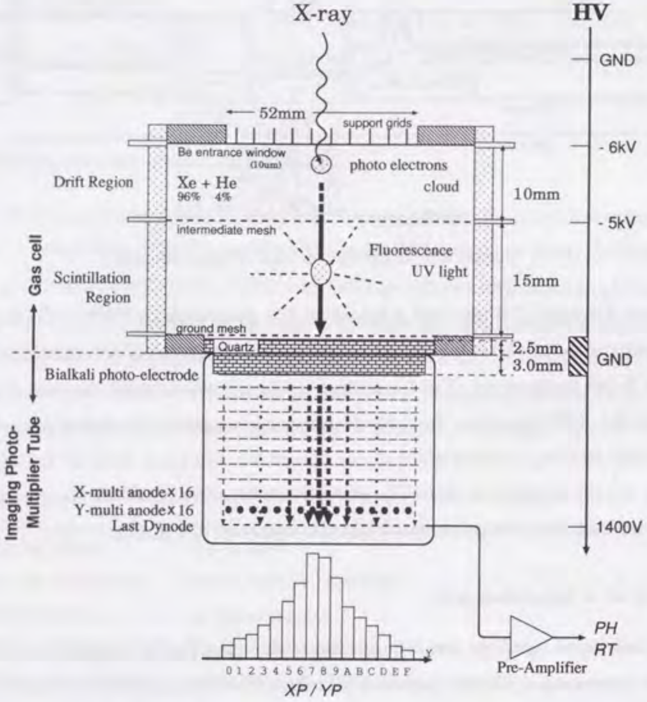

Figure 3.10: Schematic view of the GIS sensor system

We have drastically improved the soft X-ray sensitivity of the GIS as compared with previous gas counters, by using the X-ray entrance window made of vacuum tight 10 μm thick berylium foil. This has newly been developed by Yamaha Corporation, which is employed for the first time in space. The window has a 10% transmission at 0.7 keV, and the opening area is 52 mm in diameter. The foil material has a diameter of 66 mm and bonded to a cupro-nickel flange with high temperature epoxy. The window support is made of a thin molybdenum grid plated with copper, and a stainless steel mesh coated with tin is placed between the grid and the berylium foil to provide a fine support. The molybdenum grid has a height of 3.5 mm and a thickness of 0.1 mm and runs at 5 mm pitch. The grid itself can stand against several atmospheric pressure. The shadow of the grid onto the X-ray image is not a major problem since the wall thickness is thinner than the point spread function of the XRT. The fine-supporting mesh has 1.2 mm pitch and 84% transmission with a wire thickness of about 80 μm.

The exit window, with 2.5 mm thickness and a diameter of 72 mm quartz plate, is bonded to the Kovar flange using pressed indium and a small amount of high temperature epoxy resin as an additional sealant. Quartz has short-wavelength cutoff of ~ 150 nm and a relatively high transmission for the UV lights ($\lambda \sim 170$ nm). Kovar has been chosen because its thermal expansion coefficient matches that of quartz. The sealing has turned out to be successful over a temperature range from -25 °C to 110 °C against a pressure of 1.5 atm.

Imaging photo-multiplier tube (IPMT)

We employ Hamamatsu Photonics type R4268 IPMT, which is equipped with a quartz window and 10-stage dynodes. The anode has a cross-wire configuration with 16 wires running in each X and Y direction at an interval of 3.75 mm. We obtain the position information from the anode signals, and derive the pulse-height (PH) and the rise-time (RT) information from the last dynode. A pencil-beam light input to the IPMT shows a distribution of the output charge of about 7 ± 1 mm FWHM and the intrinsic position resolution of the phototube to be about 0.1 mm FWHM. To avoid hitting the gas cell by the pohotocathode during the launch, a kapton ring is inserted along the edge of the quartz surface to create a gap of ~ 0.1 mm.

Radiation belt monitor (RBM) and high voltage supplys (HV-H and HV-L)

In order to monitor the radiation environment, a radiation belt monitor (RBM) is equipped to GIS2. Its purpose is to generate an alarm signal (RBM-flag) for the high radiation flux based on the count rate. This RBM flag automatically turns down the high voltages of the GIS. The RBM sensor is made of a small PIN diode of 1 cm × 1 cm size with a thickness of the Si 100 μm. The entranse window is 15 μm thick Al. The field of view has a solid angle of 1.8 str, and its direction is opposite to the GIS entranse direction.

We use two types of high voltage units for the GIS. One produces about +1000 V for the IPMT, and the other provides negative potential down to -8000 V to the gas cell. The former is called HV-L and the latter is HV-H. In the orbit, we keep the entrance window of the gas cell at -6000 V and the mesh at -5300 V. An automatic control of the high voltage for both HV-H and HV-L is carried out in orbit by the RBM-flag.

3.4.2 Onboard data processing of the GIS

We outline the signal processing in the GIS system in figure 3.11. The front-end processing is carried out within the GIS sensor part (GIS-S), and it is followed by a detailed handling in the main electronics section (GIS-E). The front-end electronics attached to the IPMT accommodates 33 charge-sensitive preamplifiers, one for the last dynode, and the other for the 32 anode wires (16 X-anode + 16 Y-anode). The time constant of the each preamplifier is 110 μsec.

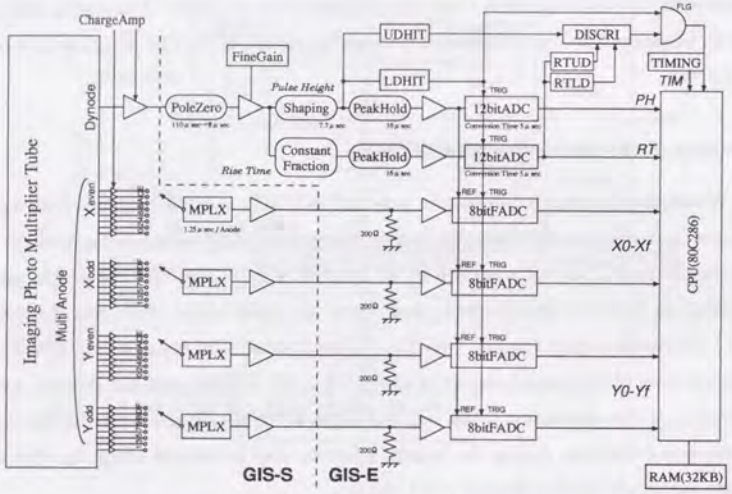

Figure 3.11: Data flow chart of the GIS electronics

The signal from the last dynode goes through fine-gain adjustment, upper (UD) and lower discriminators (LD), and then to pulse-height and rise-time ADCs. The pulse-height ADC converts the pulse-height of the signal into 12 bit value of PH. The rise-time ADC converts the rise-time of the signal into 8 bit value of RT. For the rise-time measurement, we employs the same logic as established for the Tenma GSPC (Koyama et al. 1984). The upper and the lower RT discriminators (RTLD and RTUD, respectively) operate on the digitized RT after the rise-time ADC. The arrival time of the signal is measured by clock, and is converted into 10 bit value of TIM. The 32 anode signals are treated by 4 flash ADCs incorporating analog multiplexer, and their pulse-heights are converted into 8 bit values of $X0$–Xf and $Y0$–Yf in reference to the dynoe pulse-height. If the event satisfies the condition that LD $\leq PH \leq$ UD and RTLD $\leq RT \leq$ RTUD, all these data (PH, RT, TIM, $X0$–Xf, $Y0$–Yf) are sent to the onboard CPU (80C286) and subjected to further data processing.

The main tasks of the onboard CPU are: (1) calculating the event position, (2) rejecting background with spread discriminator (SPD), (3) formating event data and sending it to the satellite data processor (DP).

The two-dimensional position of an X-ray event ($RAWX$, $RAWY$) is calculated by onboard CPU using offset- and gain-compensated values of $X0$–Xf and $Y0$–Yf. The standard calculation algorithm employs a linearized fitting to one-dimensional Lorenzian distribution (FLF). The time for the position calculation is $\sim$ 8.5 ms/event. The alternative algorithm calculates the center of gravity for square of the anode pulse-heights. This requires the calculation time of only $\sim$ 2 ms/event but results in a image distortion toward the edge. The CPU calculates the width of the distribution together with the event position, which is called spread (SP). The CPU performs a background rejection with ($RAWX$, $RAWY$) and SP.

In PH mode, digital signals collected or calculated by the onboard CPU are formated into 32 bit data per event. The 32 bit data usually consits of sensor ID (1 bit), PH (10 bit), $RAWX$ (8 bit), $RAWY$ (8 bit), and RT (5 bit). We can change this bit assignment by a command, in such case as timing observations. These 32 bit data are sent to the telemetry in every 3.9 ms interval in high bit-rate.

3.4.3 Background rejection of the GIS

One of the major design goals of the GIS is to achieve a very low level of non X-ray background (NXB). For this purpose, the GIS employs both hard-wired and software-based rejection. The hard-wired part performs usual PH and RT discrimination similar to that used for Tenma. We can control the RT window (RTLD–RTUD) by commands. When X-rays are properly absorbed in the drift region, all the signal should exhibit a RT of about 3 μsec which corresponds to the drift time of electrons in the scintillation region (see §3.4.1). On the other hand, particle events creating a long electron track in the drift region exhibit longer RT. Compton scattered electrons by γ-rays in the ceramic wall also produce signals with rather long RT because the electric field near the wall is weak. If Compton scattering of γ-rays or ionization by a particle are reacted only in the scintillation region, a signal with shorter RT is observed. Using the RT discrimination employing hard-wire electronics, we can efficiently remove NXB.

However, the RT distribution broadens significantly for lower values of PH, because the signal to noise ratio gets worse. Therefore we set the RT window rather large in orbit. We can further reduce NXB by applying a PH dependent RT mask on ground. Although pre-launch and in-orbit calibration revealed the position dependence of RT (degraded by $\sim$ 4% near the rim of the detector), the measured RT can be converted to a position independent value (rise-time invariant; *RTI*) to allow the strict background rejection using this post-observation *RT* mask. Figure 3.12 and figure 3.13 demonstrates the background rejection with the strict *RT* mask on ground.

Besides the *RT* discrimination (RTD), we utilize another background rejection logic called *SP* discrimination (SPD). As described in §3.4.2, *SP* means the width of the light

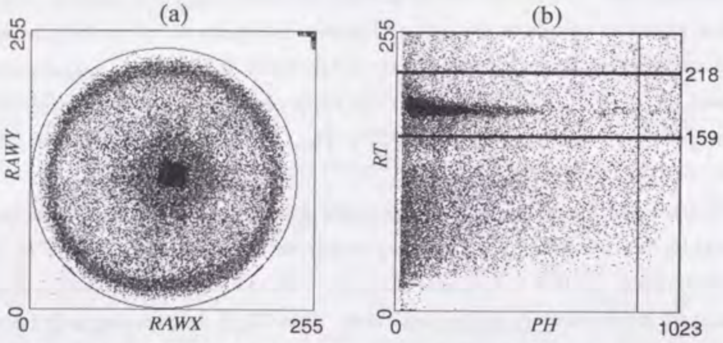

Figure 3.12: (a) An example of *RAWX-RAWY* image of a celestial X-ray point source, obtained with GIS2 in a very early observation (in fact, this is the first light target for the GIS). No background rejection was applied, except the pulse-height UD. An event concentration near the detector rim is partly due to the background enhancement, and partly due to the position non-linearity. (b) The X-ray events contained in the image of panel (a), displayed on the plane of *PH* vs. *RT*. Two horizontal lines represent the standard onboard RTD window (RTLD–RTUD).

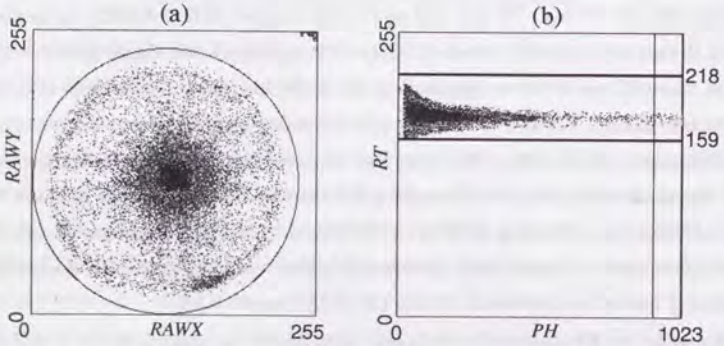

Figure 3.13: (a) Almost the same as figure 3.12a except strict *RT* mask applied. A bright spot near the center is the target source, while another spot to the lower right is the ^{55}Fe calibration isotope. (b) The X-ray events contained in the image of panel (a), displayed on the plane of *PH* vs. *RTI*.

distribution, and the onboard CPU performs SPD. SPD is sensitive to the direction of a charge track perpendicular to the electric field. If an ionizing particle runs in parallel to the window plane, RTD does not work efficiently. We can reject these events by SPD, which have much larger *SP* than those for the X-ray events. As shown in figure 3.14, *SP* is usually plotted against the squared radius from the detector center. Figure 3.14 also indicates the thresholds of SPD employed in orbit. We enabled SPD on 28 May 1993, and we have kept SPD in the same setting since then, except for a few observations conducted during 11 to 13 June 1993 in order to verify the function of SPD.

In the data analysis performed on ground, we can further reduce NXB by the strict *RT* mask mentioned above, and by discarding events near the detector edge, which also eliminates the ^{55}Fe calibration isotope events. The combined use of these discriminations gives the GIS detector a similar performance to that of the multi-cell proportional counters, such as LAC onboard Ginga, with respect to the background performance. Table 3.4 summarize the background rejection mechanisms of the GIS and background rate at each stage. In §4.4, we describe in-orbit performance of the GIS background rejection scheme.

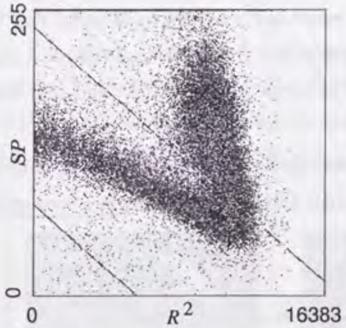

Figure 3.14: A scatter plot of events of a blank sky displayed on the plane of squared radial distance from the center in *RAWX-RAWY* image vs. *SP*. A nearly horizontal branch is formed by signal X-rays of the CXB, while a nearly vertical branch, which means a large scatter in the spread of UV light, originates from background near the detector wall. Two slant lines indicate the standard SPD window.

Table 3.4: NXB count rate of the GIS in the 0.17–11 keV range under various rejection conditions

Condition	Radius (mm)	Rate (c s^{-1} sensor^{-1})	Remark
Raw NXB	whole detector	23–78*	*LDHIT*†
+ Hard-wired rejection (RTD)	whole detector	1.7–4.7*	*L1*†
+ onboard CPU rejection (SPD)	whole detector	0.7–1.2*	*CPUOUT*†
+ Radius cut	≤ 17	0.059–0.11	
+ strict *RT* mask	≤ 17	0.044–0.086	Final value‡

* Including ~ 0.3 c s^{-1} from the calibration isotope.
† Monitor items in telemetry. See §3.4.4.
‡ Final NXB level (RNXB), corresponding to (5-9) × 10^{-4} c s^{-1} cm^{-2} keV^{-1}.

3.4.4 Monitor counts and house keeping (HK) data of the GIS

To estimate the NXB rate and the dead time, processed event rates at various stages in GIS-E are read out as the GIS monitor counts. Table 3.5 shows a list of the GIS monitor counts. All monitor counts are counted by 8 bit non-reset counter, and read out to be edited into the telemetry format. RBM events are also counted with 16 bit non-reset counter and sent to the telemetry. These event numbers except $CPUIN$ and $CPUOUT$ are processed by hard-wire electronics to avoid the dead time from CPU calculation. Distributions projected on X or Y axes are also provided for quick look or to inform spatial distribution of the X-ray image even if some regions of the GIS f.o.v. are masked by commands. Figure 3.11 also displays sampling points of the monitor counts.

We can correct the GIS data for the dead time using these monitor counts, as

$$dead\ time\ fraction = \frac{TLMOUT}{CPUOUT} \cdot \frac{CPUIN}{L1} \cdot (1 - LDHIT \cdot \tau_{PH}). \tag{3.1}$$

Here $TLMOUT$ is the number of events which appeared to the telemetry. A constant factor τ_{PH} means the hard-wired dead time per event and was confirmed to be $\tau_{PH} \sim 25\ \mu s$ in PH mode. The factors $\frac{TLMOUT}{CPUOUT}$, $\frac{CPUIN}{L1}$, and $(1 - LDHIT \cdot \tau_{PH})$ represent the dead time due to the telemetry saturation, that due to the onboard CPU, and that due to the hard-wire electronics, respectively.

As for the house keeping (HK) monitor items, voltage of both HV-H and HV-L, output current of HV-H, and temperatures of the IPMT heads and the RBM sensor are converted into 8 bit values and sent to the telemetry.

Table 3.5: Summary of the GIS monitor counts

Name	Remark
$LDHIT$	counts of (LD $\leq PH$)
$L0$	counts of (LD $\leq PH \leq$ UD *and* $RT <$ RTLD)
$L1$	counts of (LD $\leq PH \leq$ UD *and* RTLD $\leq RT \leq$ RTUD)
$L2$	counts of (LD $\leq PH \leq$ UD *and* RTUD $< RT$)
$H0$	counts of (UD $< PH$ *and* $RT <$ RTLD)
$H1$	counts of (UD $< PH$ *and* RTLD $\leq RT \leq$ RTUD)
$H2$	counts of (UD $< PH$ *and* RTUD $< RT$)
$CPUIN$	counts taken in by the onboard CPU
$CPUOUT$	counts output by the onboard CPU

3.4.5 Basic event conversion for the GIS

The raw GIS outputs for an event are PH, RT, and calculated position ($RAWX$, $RAWY$), as mentioned in §3.4.2. However, these value are subject to various non-ideal instrumental properties of the GIS. Therefore, we convert them into linearlized quantities: PI, RTI, and ($DETX$, $DETY$), respectively. We useually use PI and ($DETX$, $DETY$) for scientific analyses. RTI is utilized to apply the strict RT mask described in §3.4.3. The procedure of converting ($RAWX$, $RAWY$) into ($DETX$, $DETY$) is called "position linearlization", and that of PH into PI is called "gain correction". We explain these procedure in the following.

Position linearization

Raw X-ray images obtained with the GIS are somewhat distorted toward the detector rim, by the non-linearity in the position response. Figure 3.15 shows an image of the sunlit earth, where solar X-rays scattered off the atmosphere provides an X-ray source of uniform brightness. Slightly deformed lattice of shadows are cast by the rectilinear window support grids.

Pre-launch calibrations, including scanning measurements with collimated X-ray beams, provided look-up tables for conversion from raw position outputs ($RAWX$, $RAWY$) to the *linearized* detector coordinates ($DETX$, $DETY$). Rotation (0° for GIS2 and −90° for GIS3) and Y-flip of the coordinates are also applied in the course of this

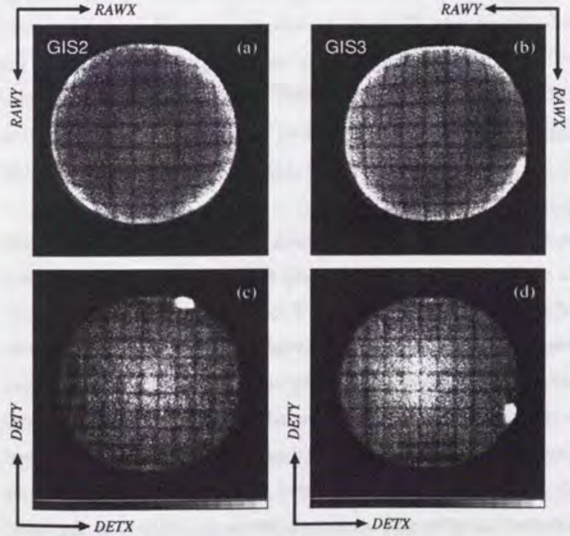

Figure 3.15: X-ray images of the sunlit earth in the 1–3 keV energy band from GIS2 (panel a) and GIS3 (panel b), presented in the $RAWX$-$RAWY$ coordinates. Images are rotated and Y-fliped so that the coordinates match the direction of the $DETX$-$DETY$ coordinates. Panels (c) and (d) are the same images from GIS2 and GIS3 respectively, after converted to the $DETX$-$DETY$ coordinates.

conversion (see figure 3.15). Figure 3.16 illustrates how the conversion tables look. The tables have been confirmed in orbit in reference to the window support girds. In the linearized $DETX$-$DETY$ image of figure 3.15, the grid lattice appears quite rectilinear.

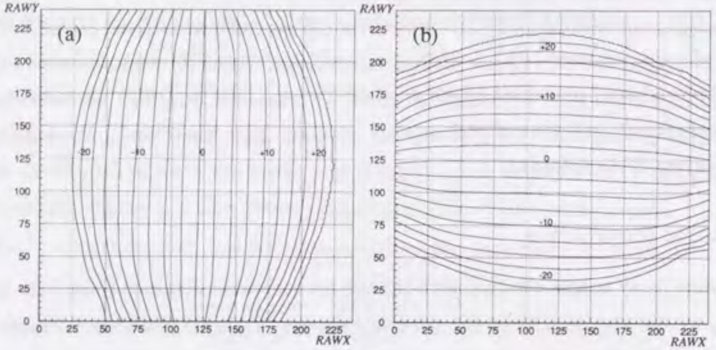

Figure 3.16: The position linearlization maps in $RAWX$-$RAWY$ coordinates for GIS2. (a) ($RAWX$, $RAWY$) to $DETX$, and (b) ($RAWX$, $RAWY$) to $DETY$. Contour levels are -22.5–25 mm in 2.5 mm step. The map versions are `xflf_s2.table` and `yflf_s2.table`.

Gain correction

When accumulating X-ray photons into an X-ray spectrum, we usually convert PH (pulse-height) of each detected event into PI (pulse-invariant) so that X-rays of the same energy give the same PI value (except the finite energy resolution) independently of the position, the temperature of phototube or the observation period. The conversion factor from PH to PI is called gain. The gain depends on four factors: (1) detected position of the incoming X-rays, (2) the temperature of the GIS, (3) the long-term gain drift, and (4) the signal count rate of the GIS.

The GIS gain is position dependent by $\sim \pm 10\%$ peak-to-peak due to non-uniformity in the IPMT gain. Calibration of this effect involves a look-up table called "gain map", which summarizes relative gains of each detector as a function of the position of event occurrence. Preliminary gain maps were generated based on the pre-launch calibration. In order to compensate for possible gain changes at the launch, and to increase the reliability, we have updated the gain maps several times in orbit. This procedure utilized the instrumental Cu-K line seen in the NXB spectrum (§4.19) after a long data integration. We also utilized intense Fe-K lines from celestial sources (largely extended objects, or those observed at different positions), e.g. clusters of galaxies and supernova remnants (SNRs). In the latest version of gain maps as of May 1995 (figure 3.17), the reliability has been improved to within $\pm 1\%$ and $\pm 2\%$ for the regions of radius < 15 mm and 15–20 mm, respectively, for both detectors.

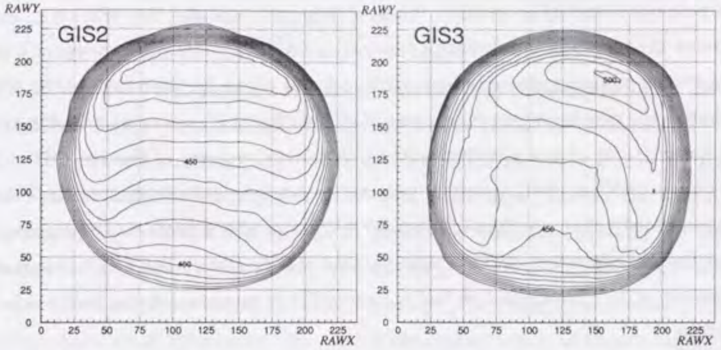

Figure 3.17: The gain maps in ($RAWX$,$RAWY$) coordinates for GIS2 (left panel) and GIS3 (right panel). Contour levels are every 10 step from 350. The gain map versions are `phfl_s2_v3.table` and `phfl_s3_v3.table` for GIS2 and GIS3, respectively.

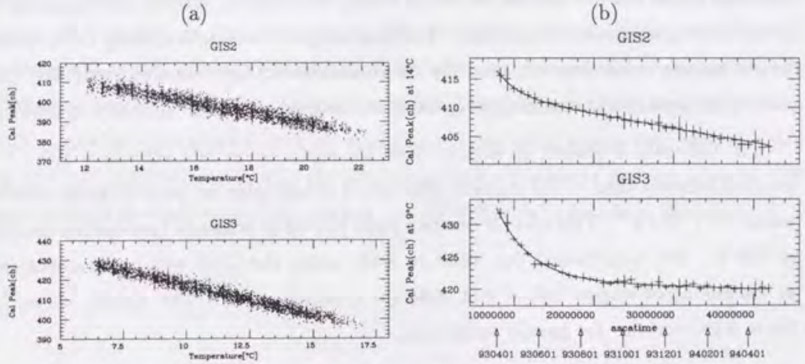

Figure 3.18: (a) Peak PH channels of the ^{55}Fe calibration isotope, plotted against the detector temperature measured in orbit on the side wall of IPMT. (b) Long-term gain history since the launch till April 1994, expressed in terms of the temperature-corrected ^{55}Fe PH. Upper and lower panels are for GIS2 and GIS3, respectively.

The GIS gain depends significantly on the temperature, because of the temperature dependence in the IPMT and gas cell. The GIS gain is monitored continuously in orbit in reference to the built-in ^{55}Fe isotope, and so is the IPMT temperature. We show in figure 3.18a, the gain vs. temperature relation thus calibrated in orbit, which reconfirms the behavior observed on ground. We have frequently updated this relation to take into account the long-term gain change (see next paragraph), and use it to correct the GIS gain for the temperature dependence. This relation of the temperature and the GIS gain, including the long-term gain change, is called "gain history", and summarized in the FITS file format table of `gis_temp2gain.fits`. The temperatures of the two GIS detectors vary by ~ 10 °C in orbit, mainly in response to satellite attitude changes. It is therefore recommended not to use the GIS data for 2–3 hours after a large attitude maneuvering, until the GIS detectors attain a new thermal steady state. The GIS2 temperature is higher by ~ 5 °C than that of GIS3, since GIS2 is mounted on the sunlit side of the satellite.

Figure 3.18b shows the long-term GIS gain history in reference to the ^{55}Fe isotope, after correction for the temperature variation. Thus, the gain of both detectors decreased by 2–3% for the first several months in orbit, but the trend has gradually flattened. This slow gain decrease is possibly due to a slow degradation in the UV transmission of quartz windows of the gas cell and the IPMT, through, for example, gradual developments of cosmic-ray induced crystalline defects. This gradual gain decrease is unlikely to be caused by out-gassing in the detector, since the RT characteristics have remained constant. The temperature coefficient and long-term trend are both reliable to an accuracy of $\pm 0.4\%$.

The GIS gain is pushed up slightly when the signal count rate exceeds ~ 100 c s^{-1} (sources brighter than ~ 100 mCrab), although it is negligible for extra-Galactic objects which are $\lesssim 50$ c s^{-1}. This effect is due to a pulse pile-up in pole-zero cancellation circuits of GIS-E. We re-calibrated this effect in orbit, using the Crab nebula data obtained at various offset angles (hence with different counting rates). The results, shown in figure 3.19, confirms the ground calibration.

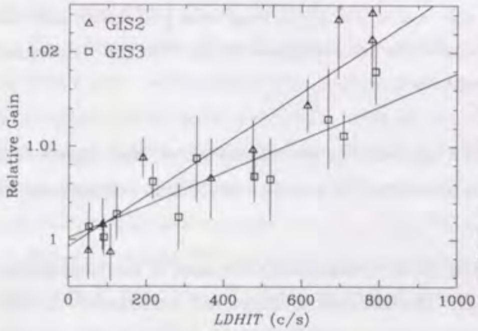

Figure 3.19: Relative GIS gains plotted as a function of the incident source count rate ($LDHIT$). A slight gain increase is seen in high counting rates. Two lines superposed on the data points show the the best line of

$$\begin{cases} y = 0.9993 + 0.27438 \times 10^{-4} LDHIT \\ y = 1.0002 + 0.17559 \times 10^{-4} LDHIT \end{cases}$$

for GIS2 and GIS3, respectively.

Thus, the formula to convert PH to PI is:

$$PI = \frac{norm \times PH}{gainmap(RAWX, RAWY)\ gainhistory(t, T)\ f(LDHIT)} \tag{3.2}$$

where t, T, and $f(LDHIT)$ are the arrival time of the event, the temperature of the GIS, and the $LDHIT$-gain relation of figure 3.19, respectively. The factor $norm$ determines the *absolute* GIS gain scale. Although this was well established once in pre-launch calibration, an independent in-orbit determination is of vital importance because the IPMT gain can change by up to several percent due to the launch vibration. However the built-in calibration isotope cannot provide a required accuracy, since it is attached at the detector edge where the gain map becomes the most uncertain. Accordingly, we have accumulated the instrumental Cu-K fluorescence line within the central region of 12 mm radius, for a long time utilizing night- and day-earth observations, with the temperature and gain-map corrections. We have used the resulting Cu-K line as a fiducial to determine the absolute energy scale.

We then cross calibrated the results of gain correction using the Au-M absorption edge structure produced by the gold plated surface of the XRT, seen in the spectra of bright sources such as the Crab nebula. For an additional confirmation, we also used collisionally-excited intense Fe-K emission lines from several celestial sources, particularly SNRs and clusters of galaxies. Although energies of these celestial Fe-K lines are intrinsically somewhat uncertain due to mixture of different ionization states, they have provided an accurate cross calibration with the SIS energy scale. We believe that the absolute GIS gain scales thus established is accurate to ~ 1.2% within ~ 15 mm from the center.

Chapter 4

In Orbit Calibration of the GIS

4.1 Overview

In the present thesis, we will perform a detailed investigation of the spectrum and brightness of the CXB. For this sort of quantitative ASCA data analysis, accurate knowledge of the instrumental response and the detector background is of essential importance. However, ASCA's response and background depend very much on the position and shape of the target source, so that a number of carefull calibrations have to be carried out in orbit. Some of these calibration results are compiled as a part of the calibration data base, in the form of FITS files, which are made publicly available. Response and background builder are also needed, which access those calibration results and generates specified responses or backgroud spectra/images at any positions/energy-bands on the detector. After the launch of ASCA, we have been conducting extensive efforts of in-orbit calibration using the GIS detector, and the results have been fed back efficiently to the response and background builder.

Since the CXB is extended all over the detector plane, importance of these calibration effort is much greater than is required in nominal point source analysis. In particular, stray light of the XRT causes a severe difficulty when we try to generate a response for the CXB spectrum. In this chapter, we will explain how the response is built in §4.2, effects of stray light for the CXB analysis in §4.3, and the non X-ray background (NXB) of the GIS in §4.4.

4.2 Response of the XRT+GIS system

4.2.1 Formulation of the ASCA response and an ARF builder

Here we formulate the response of the XRT+GIS system, with some definitions of the coordinates. Let $F(\theta, \phi, E)$ be a source X-ray distribution, where E is the X-ray energy and $(\theta,\ \phi)$ is the two-dimensional position on the sky. Angles of θ and ϕ are defined from

Table 4.1: Summary of the coordinates

Notation	Figure label	Unit	Comments
E	Energy	keV	Energy of the incident X-ray
PI	channel energy	ch	500 ch = 5.8942 keV, starts from 0 ch
θ	offset angle	arcmin	offset angle from the optical axis
ϕ	azimuth angle	degree	measured clock-wise from X-axis on detector plane
$DETX$	detector coordinates	mm	1 mm=4 ch=0.9822 arcmin, centered the detector
$DETY$		ch	center. (0, 0) mm corresponds to (128.5, 128.5) ch
$XRTX$	XRT coordinates	mm	1 mm=4 ch=0.9822 arcmin, centered the optical
$XRTY$		ch	axis. Y-axis filpped to the detector coordinate

the optical axis of the XRT (nearly parallel to the Z-axis of the satellite) as an offset-angle and an azimuth-angle, respectively. E, θ, and ϕ are usually expressed in unit of "keV", "arcmin", and "degree", respectively. Note that ϕ increases in the clock-wise direction from the X-axis on the detector plane, because it is defined in the satellite coordinates (look-down) while the detector coordinates is look-up. Also, let $D(DETX, DETY, PI)$ denote the observed data, i.e. distribution of detected X-ray photons with pulse-invariant PI (gain corrected pulse-height), and detected position $(DETX, DETY)$. PI is expressed in unit of "ch", which begins from 0 and is scaled so that 500 ch correspond to 5.8942 keV (energy of the Kα line from ^{55}Fe calibration source). $DETX$ and $DETY$ is measured in "mm" or "ch" which is defined so that $1\,\mathrm{mm} = 4\,\mathrm{ch}$ and the center of the detector $(0\,\mathrm{mm}, 0\,\mathrm{mm})$ corresponds to $(128.5\,\mathrm{ch}, 128.5\,\mathrm{ch})$ for the GIS. As the focal length of the XRT is 3500 mm, 1 mm on the detector coordinates correspond to $60 \times \tan^{-1}(1/3500) \times 180/\pi = 0.9822$ arcmin on the sky. There also is a coordinate called $(XRTX, XRTY)$, the scale of which is similar to $(DETX, DETY)$ but centered on the optical axis of the XRT and the Y-axis flipped. Table 4.1 is a summary of these coordinates.

$F(\theta, \phi, E)$ and $D(DETX, DETY, PI)$ are related as

$$\begin{aligned} & D(DETX, DETY, PI) && (4.1) \\ & \quad = \int dE\, R_{GIS}(E, PI) \\ & \quad \times \int dx\, dy\, P_{GIS}(E, x, y; DETX, DETY)\, A_{GIS}(E, x, y) \\ & \quad \times \int d\theta\, d\phi\, P_{XRT}(\theta, \phi, E; x, y)\, A_{XRT}(\theta, \phi, E) \\ & \quad \times A_{T.S.}(E) \\ & \quad \times F(\theta, \phi, E) \end{aligned}$$

Table 4.2: Summary of factors constituting the response function

Notation	Description
$A_{T.S.}(E)$	transmission of the thermal shield
$A_{XRT}(\theta, \phi, E)$	effective area of the XRT
$P_{XRT}(\theta, \phi, E; x, y)$	point spread function (PSF) of the XRT
$A_{GIS}(E, x, y)$	quantum efficiency of the GIS
$P_{GIS}(E, x, y; DETX, DETY)$	point spread function (PSF) of the GIS
$R_{GIS}(E, PI)$	energy redistribution matrix for the GIS

where (x,y) is the position on the entrance window of the GIS. This complicated integral transform, as a whole, is what is called the instrumental response. The meaning of each factor constituting the response is summarized in table 4.2. More detailed explanations for them are given in the following section. In particular, we usually integrate the data $D(DETX, DETY, PI)$ over a specified area Ω on the detector to obtain a spectrum $H(PI; \Omega)$, as

$$H(PI; \Omega) = \int_{\Omega} dDETX\, dDETY\; D(DETX, DETY, PI) \qquad (4.2)$$

The method of spectral fitting is a procedure of finding a set of parameters for $F(\theta, \phi, E)$ which give the most similar model spectrum $H(PI; \Omega)$ to the observed PI spectrum.

If the target is a point source or have a uniform spectrum in the effective integration region on the sky, $F(\theta, \phi, E)$ can be factorized as $F(\theta, \phi, E) = B(\theta, \phi)\, S(E)$, where $B(\theta, \phi)$ is a surface brightness profile and $S(E)$ is a spectrum. Then, equation (4.1) will have a simpler form of

$$H(PI) = \int dE\; R_{GIS}(E, PI)\; A_{XRT+GIS}(E)\; S(E) \qquad (4.3)$$

where:

$$\begin{aligned} A_{XRT+GIS}(E) &= \int_{\Omega} dDETX\, dDETY && (4.4) \\ & \times\; A_{T.S.}(E) \int dx\, dy\, P_{GIS}(E, x, y; DETX, DETY)\, A_{GIS}(E, x, y) && (4.5) \\ & \times \int d\theta\, d\phi\, P_{XRT}(\theta, \phi, E; x, y)\, A_{XRT}(\theta, \phi, E)\, B(\theta, \phi) && (4.6) \end{aligned}$$

$R_{GIS}(E, PI)$ is called an RMF (energy Redistribution Matrix File) and $A_{XRT+GIS}(E)$ is called an ARF (Auxiliary (or Ancillary) Response File). Note that the RMF is determined only by the elementary process of the detector, and that only one RMF for one detector is sufficient for all the analysis. We should rebuild only ARFs when changing the target position or the integration area. This is a great merit of saving time and disk

Table 4.3: Summary of the calibration files of XRT and GIS for jbldarf

Function	Calibration file
$A_{T.S.}(E)$	analytic
$A_{XRT}(\theta, \phi, E)$	`xrt_ea_110494.fits`
$P_{XRT}(\theta, \phi, E; x, y)$	`xrt_psf_v1.1.fits` (not in the caldb)
$A_{GIS}(E, x, y)$	`s2bev1.fits` / `s3bev1.fits` (Be window thickness)
	`s2gridv3.fits` / `s3gridv3.fits` (GIS grid transmission)
	analytic (others)
$P_{GIS}(E, x, y; DETX, DETY)$	analytic
XRT-GIS alignment	`gis2_ano_on_flf_180295.fits` /
	`gis3_ano_on_flf_180295.fits`

spaces to build/hold a response. To be accurate, the RMF of the GIS slightly depend on a position of incoming X-rays, but in most case it is negligible.

There is a spectral fitting package called **XSPEC**, which is commonly used for X-ray astronomy in the world. **XSPEC** needs four files to conduct a spectral fitting: (1) a spectrum file to be fitted, (2) a background spectrum file to be subtracted, (3) an RMF, and (4) an ARF. RMFs for GIS2 and GIS3, which **XSPEC** can read, are released and occasionally updated by the GIS team in FITS file format. The latest RMFs of GIS2 and GIS3 as of December 1995 are `gis2v4_0.rmf` and `gis2v4_0.rmf`, respectively, and registered in the calibration data base (here after caldb). An ARF, also an **XSPEC**-readable FITS file, is created by a program so called an ARF builder.

There are several kinds of ARF builders for ASCA. **jbldarf** (present version 2.10) is the most commonly used ARF builder in Japan, which has been developped by M. Hirayama and Y. Ishisaki. A user inputs the target position, integration area on the detector plane, and some other information such as detector ID or output file names, to **jbldarf**. Then, **jbldarf** conducts the integral calculation of equation (4.4) and create an ARF. To calculate the functions shown in table 4.2, **jbldarf** interpolates pre-calculated tables or utilize an analytic form of the function. Most of the pre-calculated tables are also registered in the caldb. Table 4.3 summarizes how these calculations are carried out.

In the following sections, we will explain ARF (§4.2.2, §4.2.3) and RMF (§4.2.4) for the XRT+GIS system. If the point spread function of the detector ($P_{GIS}(E, x, y; DETX, DETY)$) is approximated as a δ-function like in the SIS, ARF is furthermore splitted into the XRT part (equation (4.6)) and the detector part (equation (4.5)). Although this is not the case with the GIS, we describe the XRT part (§4.2.2) and the GIS part (§4.2.3) of the ARF separately, for convenience.

4.2.2 XRT part of ARF

Since the XRT does not change the energy of incident X-rays, its contributions can be confied to the ARF. An XRT response is usually expressed by two functions, an effective area $A_{XRT}(\theta, \phi, E)$ and a point spread function (PSF) $P_{XRT}(\theta, \phi, E; x, y)$. The XRT PSF is normalized so that the volume in $r \leq 6$ mm are equal to 1.0, and the effective area takes in charge of the normalization. The present XRT response is identical to all the four detectors, and have mirror symmetries with respect to the lines of $\phi = 0°$, $\pm 45°$, and $90°$.

Figure 4.1 shows energy- and θ/ϕ-dependence of the effective area. The big jump at 2.2 keV is the M-edge of Au, evaporated on the foil of the XRT. The effective area declines as θ gets larger, which is known as vignetting effect. When θ increases, e.g., along the direction of $\phi = 0°$, the projected geometrical area for mirror foils in the direction of $\phi = 0°$ (near-side) decreases, while for the foils in the direction of $\phi = 180°$ (far-side), reflectivity decreases because the grazing angle gets larger. These two effects cause the vignetting. Because of the reflectivity effect, vignetting is severer in higher energy bands. There is also ϕ-dependence by $\sim$ 20%, in such a way that the effective area becomes maximum at $\phi = 45°$, and becomes minimum at $\phi = 0°$.

Although the XRT has a large effective area up to $\sim$ 10 keV, it sacrifices the imaging quality. Due to waving (shape error) of the thin aluminium foils, as well as to the conical approximations of paraboloid (primary mirror) and hyperboloid (secondary mirror) surfaces, the PSF of the XRT has largely extended wings. Upper panels of figure 4.2 show exapmles of the XRT PSFs, taken by GIS2. Although the XRT PSF in fact has a more sharply peaked core, it is broadened to some extent in the image by the finite position resolution of the GIS. Thus the XRT PSF has four butterfly-like wings, which reflects the quadrant structure of the XRT, with significant flux extending almost over the whole GIS f.o.v. Horn like structures seen on the edges of the four wings are caused by the larger distortion of the conical shape at the outermost sector of each quadrant. As θ gets larger, the PSF shape is also distorted, as characterized by a squeezing into the radial direction and an increase in the fraction of wings. Moreover, these effects are all energy-dependent. Lower panels of figure 4.2 clearly show that the PSF has wider outskirts in the higher energy bands. This is mainly due to the scattering of incident X-rays by the micro-roughness of the foil surface, which generally increases with increasing X-ray energy.

All these properties of the XRT PSF complicate the analysis of extended X-ray sources. For example, they cause artificial temperature increase in the data of cluster of galaxies toward outer rings (Ikebe 1995). Energy dependence of the XRT PSF has been calibrated

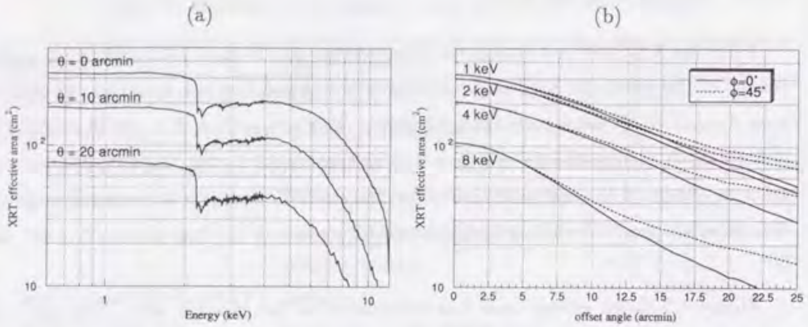

Figure 4.1: Properties of the XRT effective area. (a) Energy dependence at $\theta = 0$, 10, and 20 arcmin, for $\phi = 0°$. (b) θ-dependence (vignetting) at E =1, 2, 4, and 8 keV, for $\phi = 0°$ (solid lines) and 45° (dashes). The effective area shown here are based on the calibration data base file : `xrt_ea_110494.fits`.

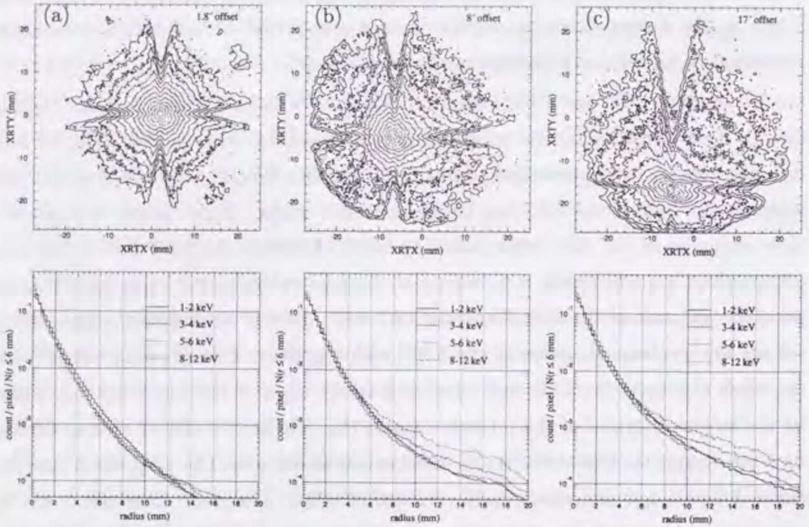

Figure 4.2: Examples of the XRT PSF taken by GIS2. (a) 1.8′ offset, (b) 8′ offset, and (c) 17′ offset Cyg X-1 images (upper panels) in the 0.5 - 12 keV band and the radial profiles (lower panels) in the 1–2 keV (solid lines), 3–4 keV (dashed), 5–6 keV (dotted), and 8–12 keV (dot-dashed) energy bands. For upper panel images, contour levels are every factor of 2, and origins of the coordinates are the optical axis of GIS2. All radial profiles in lower panels are scaled so that the volume in $r \leq 6$ mm are equal to 1.0.

with hard point-like X-ray sources, such as GRO-J1008 or Cyg X-1. It is comfirmed that the ray-tracing images agree with data within 20% level in radial profile (Furuzawa 1995, ASCA calibration meeting).

4.2.3 GIS part of ARF

Here we explain non-XRT factors for building the XRT+GIS ARF, described in equation (4.5). The quantum efficiency of the GIS ($A_{GIS}(E,x,y)$) depends on the window transmission and the absorption probability in the drift region (1 cm depth) of the gas cell, filled with 96% Xe and 4% He gas up to 1.2 atm at 0 °C. The entrance window of the GIS is made of thin belyllium foil with a mean thickness of 10.83 ± 0.02 / 10.5 ± 0.02 μm (GIS2 / GIS3, respectively). The Be window is supported by grids of 3.5 mm height, 0.1 mm thick and 5.0 mm pitch, and a mesh of 1.2 mm pitch and 84% transmission with a wire thickness of about 80 μm. The plasma shield, which locates 55 mm above the Be window, is made of aluminized myler of 37 nm (Al) + 540 nm ($C_{10}H_8O_4$) thick, supported by a mesh of 90% transmission. Thermal shield is placed just before the XRT and is almost identical to the plasma shield except that the mesh transmission is 94.2%.

Thus, the total quantum efficiency for the non-XRT factor is expressed as :

$$A_{T.S.}(E)\ A_{GIS}(E,x,y) = \qquad (4.7)$$
$$0.942\ T_{myl}(E) \cdot 0.90\ T_{myl}(E) \cdot 0.84\ T_{grid}(x,y) \cdot T_{Be}(E, t_{Be}(x,y)) \cdot (1 - T_{gas}(E))$$

where $T_{myl}(E)$, $T_{grid}(x,y)$, $T_{Be}(E,t(x,y))$, and $T_{gas}(E)$ are the transmissions of the aluminized myler, the support grid, the Be window, and the Xe + He gas, respectively. The function $t_{Be}(x,y)$ represents the thickness of the Be window at (x,y). Figure 4.3 shows the functions of $T_{myl}(E)$, $T_{Be}(E, 10.5\mu\mathrm{m})$, and the total quantum efficieny of equation (4.7) without the grid transmission. The Be window thickness map $t_{Be}(x,y)$ is measured on the ground and re-calibrated in orbit. Figure 4.4a shows the Be map for GIS2. The Be map for GIS3 is filled with a constant value of 10.5 μm. The grid transmission map of $T_{grid}(x,y)$ is measured in orbit utilizing the image of sunlit earth and summation of extended sources. Figure 4.4b shows the grid map for GIS2 smoothed by the position resolution of the GIS at 2.0 keV.

The point spread function of the GIS ($P_{GIS}(E,x,y;DETX,DETY)$) is expressed by a superposition of 1–6 Gaussians depending on the number of Xe-L escape lines, and the volume is normalized to 1.0. The reason why not a single Gaussian is used is that escape events of Xe-L exhibit a wider position scatter. The position resolution of the GIS is about 0.6 μm FWHM at 6 keV, and have an energy dependence of $\propto 1/E^{\sim 0.5}$ (thin line in figure 4.5). It also has a position dependence. It stays almost constant out to $r \sim 15$ mm, becomes worse at $r > 15$ mm, and is by 20–30% worse at $r = 20$ mm.

We basically utilize the position resolution measured on ground before launch. The overall position resolution of the XRT+GIS system is not a simple convolution of the GIS PSF with the XRT PSF, since there is an additional effect caused by the XRT+GIS combination: X-rays enters the GIS gas cell as a converging beam of ~ 2° from the XRT, while the gas cell has a finite depth of 1 cm for the X-ray absorption. These effects produce a parallax which adds to the overall position resolution. The parallax is expected to be significant for harder X-rays which has larger penetrating depths in the detector. The thick line in figure 4.5 shows the position resolution of the GIS with the effect of parallax.

It is not easy to verify the position resolution of the GIS alone in orbit, because it is usually combined with the XRT PSF. Unresolved attitude jittering of the satellite (typically ~ 1′) also contributes to the broadening of the PSF core. However, it is confirmed that the half power diameter of the combined PSF of the XRT+GIS is almost consistent with the observed one.

4.2.4 GIS part of RMF

The RMF of the GIS ($R_{GIS}(E, PI)$) is intrinsic to the gas process of the GIS, and independent of the position of the incoming X-rays. Even the difference between GIS2 and GIS3 is negligible, and completely identical tables (except sensor ID) are provided for GIS2 and GIS3. The GIS RMF is normalized as $\int R_{GIS}(E, PI)\, dPI = 1$, and the slice at $E = E_0$ gives a PI distribution for monochromatic X-rays of E_0 keV. Figure 4.6 shows a contour map of the GIS RMF and its slices at 1, 2, 4, and 8 keV. The GIS spectrum for monochromatic X-rays exhibits a Gaussan-like peak with a low energy tail which is due to the loss of some fraction of the electron cloud because of absorption by the Be window. This effect is modeled by a diffusion of electron clouds (Inoue et al. 1978), and the PI spectrum can be approximated by the formula:

$$F(PI) = \int_0^1 \frac{\kappa}{\sqrt{2\pi\sigma^2}} \exp\left(-\frac{(PI/\eta - PI_0)^2}{2\sigma^2}\right) \eta^{-1}(1-\eta)^{\kappa-1} d\eta \qquad (4.8)$$

where PI_0, σ, and κ represent peak channel, energy resolution, and tail fraction, respectively. The energy resolution of the GIS is about 8.0% FWHM at 6 keV, and have an energy-dependence of $\propto 1/E^{\sim 0.5}$ (figure 4.7). Escape lines appear above Xe-L edges (4.78 keV), where the small jump of PI-E relation is also seen.

When calculating $R_{GIS}(E, PI)$, we slightly modify equation (4.8) (enhance the tail at lower PI channels), and interpolate the parameters derived from the monochromatic or semi-monochromatic spectra obtained in the ground calibration. Fine tuning of the parameters, particularly in the low energy band, has been carried out in several times, in order to explain a spectrum of the Crab nebula as a standard candle (ref §4.2.5), or

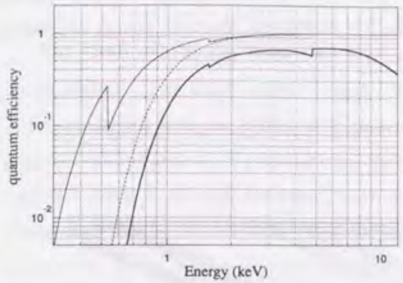

Figure 4.3: Energy dependence of the thermal shield transmission (thin solid line), 10.5 μm thick Be window transmission (dashed line), and total GIS quantum efficiency including thermal shield, plasma shield, Be window, and meshes (thick solid line). This plot is based on the version 4.0 GIS response.

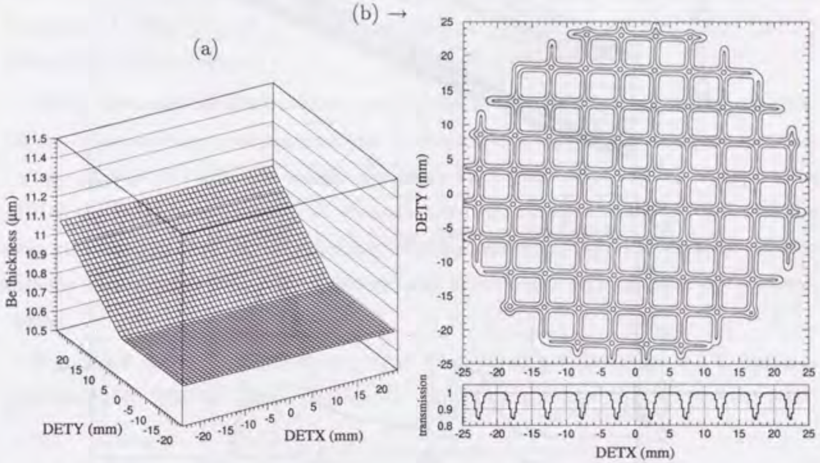

Figure 4.4: (a) Berylium thickness map for GIS2 on the detector coordinates based on the calibration data base file **s2bev1.fits**. (b) Upper panel shows a contour map of the GIS2 support grid transmission on the detector coordinates, based on the calibration data base file **s2gridv3.fits**, smoothed by the position resolution of GIS at 2.0 keV. Contour levels are 0.75, 0.85, and 0.95. Lower panel shows a cross section at $DETY = 0.0$.

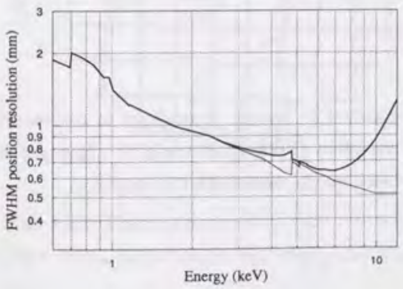

Figure 4.5: Energy dependence of the position resolution (FWHM) of the GIS with (thick line) and without (thin line) the effect of parallax. This plot is based on the version 4.0 GIS response.

strongly absorbed spectra such as EXO 2030+375 (for the low energy tail). For example, we have so far carried out modifications of the low energy tail function, energy dependence of κ and energy resolution, etc.

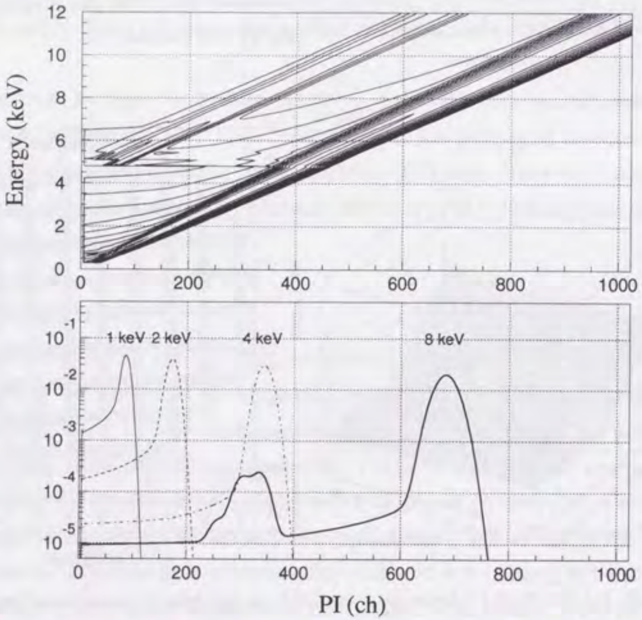

Figure 4.6: Upper panel shows a contour map of the GIS RMF `gis2v4_0.rmf`. Contour levels are every factor of 2. Lower panel shows the slices at 1 (thin solid line), 2 (dash), 4 (dot-dash), and 8 (thick solid line) keV.

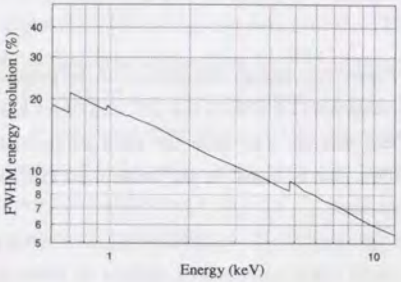

Figure 4.7: Energy dependence of the energy resolution (FWHM) of the GIS. This plot is based on the version 4.0 GIS response.

4.2.5 Verification of the XRT+GIS response for a point source

The Crab nebula has been used for an important calibration source as a standard X-ray object. The Crab is very bright (but too bright for the SIS) and have a stable X-ray emission, with an extent of $2'$ or less, which is effectively a point source for the spectral calibration. Its X-ray spectrum has been measured with a number of experiments, and is known to be well expressed with a power-law function modified by low energy absorption due to the Galactic inter stellar medium. The generally accepted values for the photon index, power-law normalization at 1 keV, and column density are 2.08–2.11, 9–11 c $\mathrm{s^{-1}}$ $\mathrm{cm^{-2}}$ $\mathrm{keV^{-1}}$, and $(2.7\text{–}3.3)\times10^{21}$ $\mathrm{cm^{-2}}$, respectively. Especially the values measured by Ginga are that $\Gamma = 2.083 \pm 0.014$ and Norm $= 11.2 \pm 0.4$ c $\mathrm{s^{-1}}$ $\mathrm{cm^{-2}}$ $\mathrm{keV^{-1}}$ (Ueda 1993, internal report).

ASCA observed the Crab nebula many times at various positions on the detector. Figure 4.8 shows these pointing positions. In particular, a very deep observation for 97 ks (becase of deadtime, effective exposure is much less) was carried out on 28 September 1994 at the 1CCD nominal position. We performed fine tunings of the GIS RMF with the deep pointing data (§4.2.4). Energy-independent normalization of ARF was also scaled so that the X-ray flux in the 2–10 keV energy band is consistent with the generally accepted value.

Figure 4.9 shows the GIS2+3 spectrum of the Crab nebula at the 1CCD nominal position, fitted with an absorbed power-law model convolved with the standard RMF

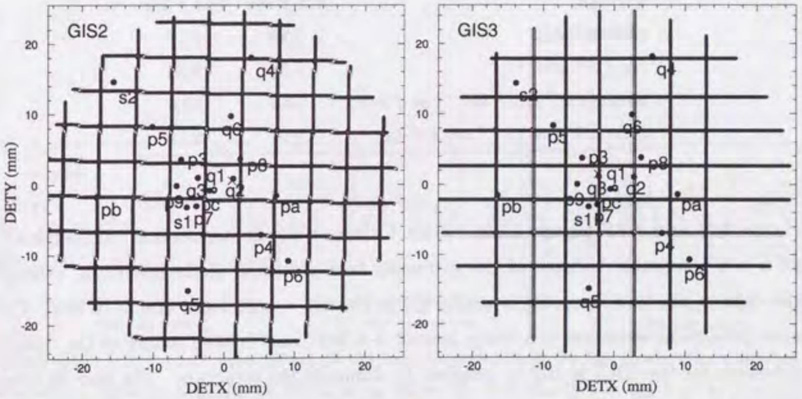

Figure 4.8: Pointing positions of the Crab nebula (●) overlayed on the grid maps of GIS2 and GIS3. Open circle labeled "q1" shows the 1CCD nominal position, and '×' shows the optical axis.

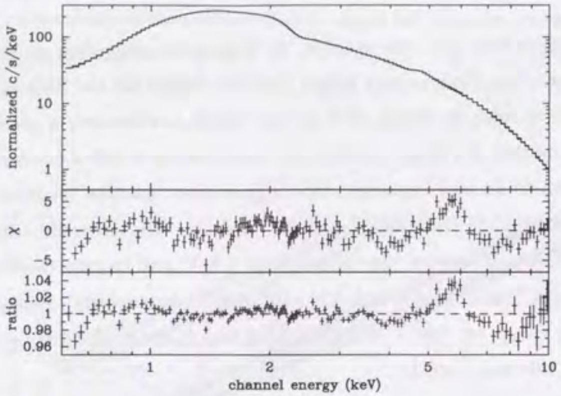

Figure 4.9: The Crab nebula spectrum fitted in the entire 0.6–10 keV energy band with an absorbed power-law model. The observation was conducted at the 1CCD nominal position on 28 Sep 1994. The spectrum is dead-time corrected and the CXB + NXB spectrum is subtracted. Deadtime corrected effective exposure is 14,466 s. The best fit parameters are shown in table 4.4. Upper panel shows the GIS2+3 spectrum (crosses) and the best fit model (solid line). Middle panel shows residuals plotted in unit of σ. Lower panel shows ratios of the data to the model.

Table 4.4: An absorbed power-law fits to the 0.6–10 keV spectrum of the Crab nebula

Sensor	GIS2	GIS3
χ^2/d.o.f	621 / 304	501 / 304
photon index	2.16	2.17
$N_{\rm H}$ (10^{22} cm^{-2})	0.32	0.34
norm (c s^{-1} cm^{-2} keV^{-1} at 1 keV)	10.3	10.8
2–10 keV flux (10^{-8} erg s^{-1} cm^{-2})	2.04	2.11

(figure 4.5) and ARF (figure 4.18). Table 4.4 shows the fitting results. Although the fit is not acceptable because of the extremely high statistics of the spectrum, ratio of the data to the best-fit model is within 5% in the full energy band of 0.6–10 keV. The most prominent structure is a hump around 5–6 keV, and further tuning of the optical constants for the XRT is still in progress to eliminate the structure. The best fit Crab parameters thus obtained are roughly consistent with the generally accepted values. The photon index shows somewhat steeper value of $\Gamma = 2.16$.

Utilizing the Crab observations, we also examined whether the position dependence of the XRT+GIS system has been adequately compensated by ARF. Figure 4.10 shows the Crab spectral parameters plotted versus offset angle θ. Since the Crab has a stable spectrum, the scatter seen there should originate in systematic errors that could not be compensated perfectly by the ARF builder. In the range of $\theta < 20'$, the derived Crab index scatters only by about ± 0.03, the absorbing column density by $\pm 0.3 \times 10^{21}$ cm^{-2}, and the inferred Crab flux by $\pm 8\%$. We can say that the spectral parameters are correct within the above uncertainties over the whole area of $\theta < 20'$. The reason why the flux scatters so much is thought to be an effect caused by the support grids on the GIS window. Furthermore, the flux appears to increase systematically and the spectrum appears to flatten, as offset angle gets larger. We discuss its possible influence upon the CXB analysis in §6.4.

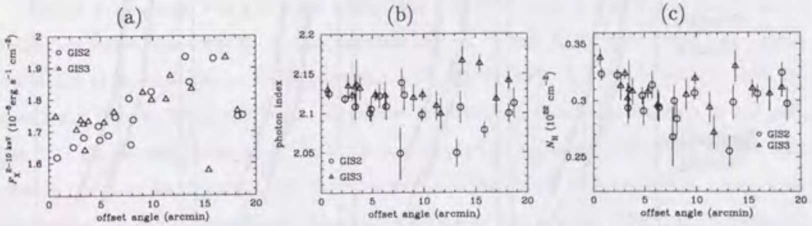

Figure 4.10: Offset angle dependence of the best fit parameters for the Crab nebula spectra, observed at different positions on the detector plane. (a) Absolute flux in the 2–10 keV energy band, (b) photon index, (c) column density. Open circles show GIS2, and triangles GIS3. Note that the results shown here are based on a slightly older version of the XRT response, which gives some inconsistensy with the value shown in table 4.4.

4.3 Stray light effect to the CXB analysis

4.3.1 What is stray light?

The XRT of ASCA allows some fraction of the X-rays, even outside of the f.o.v. from an offset angle $\theta > 30'$, to reach the focal plane detector. This phenomenon is somewhat different from the large outskirts of the XRT PSF, discussed in §4.2.2. The large outskirts of the XRT PSF are mainly due to the waving of the thin XRT foils, and those photons also undergo the normal sequence of two successive reflections on the primary and the secondary mirrors of the Wolter type I optics. Whereas most of the photons which come from outside of the f.o.v. have gone through abnormal paths, which are not on the assumption of the Wolter type I optics. These X-rays are called stray lights. The XRT configuration provides X-rays with four kinds of light paths, as shown in figure 4.11. The normal path is (a), and others are stray. For short, we call these paths (a) normal reflection, (b) primary only reflection, (c) secondary only reflection, and (d) multiple reflection. Multiple reflection is somewhat specific to the ASCA XRT (Tsusaka et al. 1995). Because both sides of the mirror foils of the XRT are coated with acrylic lacquer before Au is evaporated on the front sides, soft X-rays can reflect on the backside, too. The critical angle of the acrylic surface at 1.5 keV is $\sim 1°$.

Figure 4.12 shows an example of stray lights taken by GIS3. The Crab nebula is placed at the position of the filled circle, $60'$ offset from the optical axis in the direction of $\phi = 45° \ / \ 135° \ / \ 225°$. A shell-like image is seen spreading over the whole detector plane. The stripes represents the XRT sector structure divided by the alignment bars.

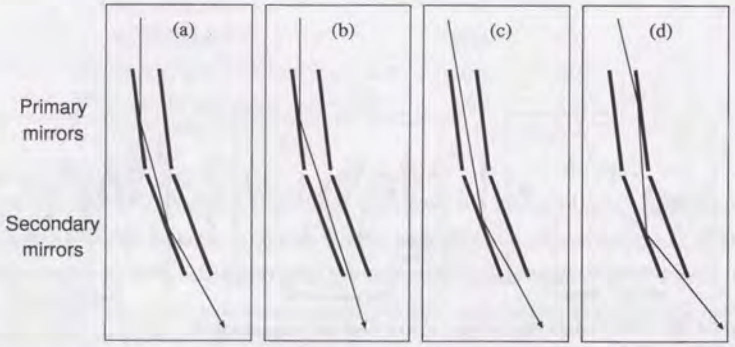

Figure 4.11: Four examples of XRT light paths: (a) normal path, (b) reflection only by primary mirrors, (c) reflection only by secondary mirrors, (d) multiple reflections by front and back surfaces of mirrors.

4.3.2 Evaluation of stray light effects by ray-tracing

Since the CXB is uniformly extending on the whole sky, we must fully take the stray light effect into account for the CXB analysis. Stray lights occupy a significant fraction of the CXB photons detected at outer rings on the detector, especially in lower energy bands (see text below). However, a stray light image has a complex shape as seen in figure 4.12, and it is not easy to express it in an analytic formula. It is also unrealistic to observe the Crab nebula in various offset and azimuth angles. There are observational time constraints and interpolation of observed patterns is also a problem. One solution is to utilize the ray-tracing (Tsusaka et al. 1995). Fortunately, stray light pattarns are well determined by the foil structure of the XRT. Therefore the ray-tracing program with reliable XRT parameters is expected to reproduce the stray light effects pretty well. Figure 4.13 shows a ray-tracing image for $\theta = 60'$ and $\phi = 225°$, which well reproduces the lower right image of figure 4.12.

Then, using a ray-tracing program, we simulate the effects of stray lights for the CXB analysis. First of all, how far the CXB photons can come from? This is very important because the CXB is distributed all over the sky and it is time consuming to integrate over large sky area. Figure 4.14a shows how much fraction of photons is expected to come from the sky $\theta > \Theta$ into the integration area of $r < 20$ mm. This figure shows that we must take into account the photons up to $\theta_{max} = 100'$ at $E = 1.0$ keV in order to determin the CXB flux at 1.0% level. We have therefore adopted $\theta_{max} = 150'$ for the CXB analysis. Since the multiple reflection component disappears rapidly in the higher energy bands, the range of θ which we must consider gets smaller as energy increase. Figure 4.14b shows predicted spectral contributions of photons which come from rings of $\theta = 0$–$20'$, 20–$40'$, 40–$60'$, 60–$80'$, and 80–$150'$. Contributions from 20–$40'$, 40–$60'$, and 60–$80'$ rings are thus expected to be comparable, but the spectrum gets softer.

Figure 4.15 shows the predicted stray light contributions in the radial profile for a uniformly extending source. At the position of $r = 20$ mm from the optical axis, stray lights are thus expected to contribute about 60/50/40/20% at 1.0/2.0/4.0/8.0 keV, respectively. The multiple reflection component contribute a significant fraction at 1.0 keV, but it is almost negligible at 4.0 keV. It is because the backside reflectivity of the foils rapidly drops in hard bands. On the contrary, the secondary only reflection component is expected to contribute almost the same fraction to the normal reflection component. The primary only reflection component can be neglected.

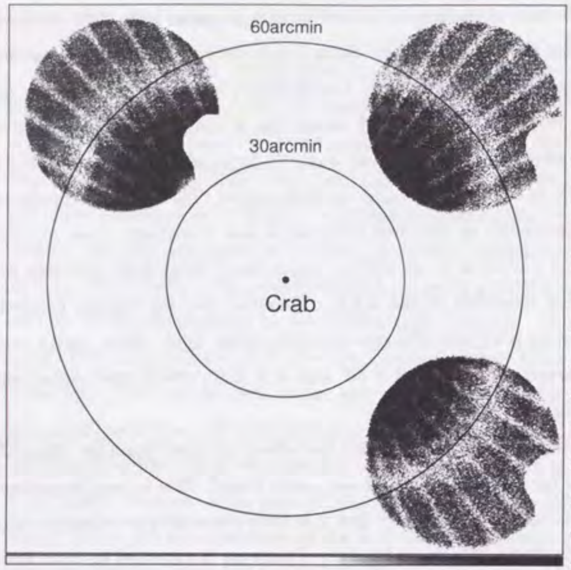

Figure 4.12: Three of the Crab stray light images taken by GIS3 in the 0.7–10 keV band, shifted and superposed on the detector plane so as to reproduce correct angular relations with respect to the Crab nebula. The location of the Crab is indicated with a filled circle, and the optical axis for each observation is offset by 60′ from the Crab.

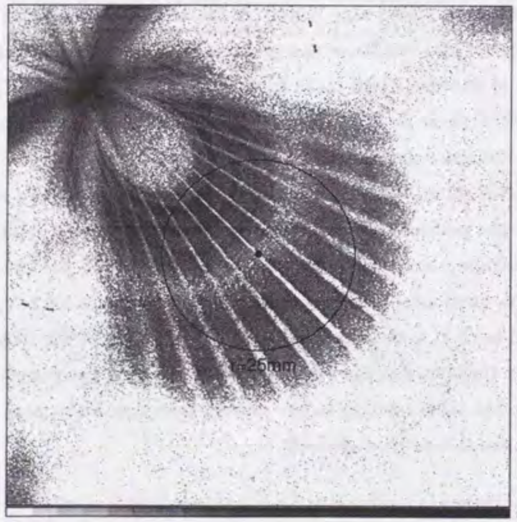

Figure 4.13: Ray-tracing image of the stray light pattern at 1 keV for the offset angle $\theta = 60'$ and the azimuthal angle $\phi = 225°$. A filled circle shows a position of the optical axis. A superposed circle of $r = 25$ mm on the image corresponds to the GIS f.o.v.

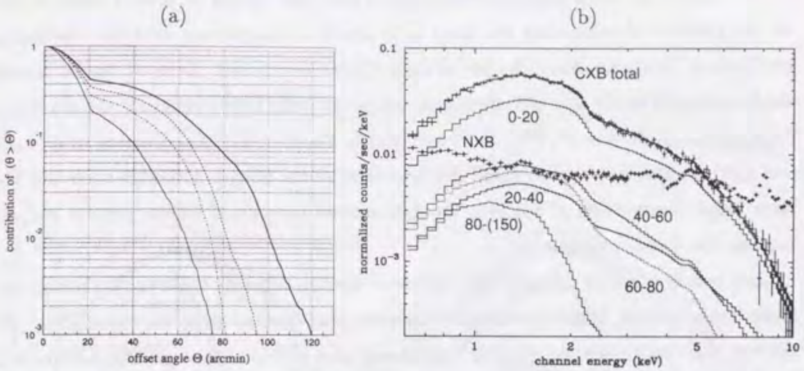

Figure 4.14: (a) Calculated ratios of the CXB photons which come from the offset angle $\theta > \Theta$, to the total CXB photons integrated within the radius of 20 mm from the optical axis, at 1 (thick solid line), 2 (dashed), 4 (dot-dashed), and 8 (thin solid line) keV. (b) The averaged CXB spectrum (crosses) and the NXB spectrum (filled circles), plotted with calculated contributions from θ = 0–20′, 20–40′, 40–60′, 60–80′, and 80–150′.

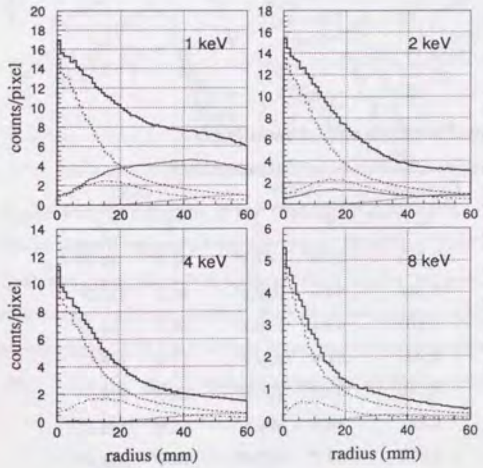

Figure 4.15: Azimuthally averaged radial profiles of the CXB image (thick solid lines) calculated by ray-tracing at the energies of 1, 2, 4, and 8 keV. Contributions of the normal reflection (dashed), the primary only reflection (dotted), the secondary only reflection (dot-dashed), and the multiple reflection (thin solid lines) are also plotted.

4.3.3 Comparison of ray-tracing with Crab stray obserbations

We carried out large offset observations of the Crab nebula at several offset angles, for the purpose of calibrating the stray light effects in comparison with the ray-tracing predictions. Table 4.5 shows the list of these Crab observations. Azimuth angles are basically arranged in the $\phi = 225°$ direction, where the stray light strength is the maximum (it is minimum at $\phi = 0°$, $90°$, $180°$, and $270°$). For $\theta = 60'$, the direction of $\phi = 45°$ and $135°$ are also observed to check the symmetry of the image. Although there are also large offset observations of Sco X-1, the data cannot be utilized for the present purpose because Sco X-1 is variable.

Left panels of figure 4.16 show the observed spectra taken by GIS2 (upper panel) and GIS3 (lower panel). Right panels show the simulated spectra using the ray-tracing. We can say that the simulation roughly reproduces the spectral shape and normalization in the range of as much as five orders of magnitude. Figure 4.17 compares the counting rate from the actual observations with those based on the simulation. There seems to exist a systematic difference between GIS2 and GIS3, although the reason is still unclear. However we are thus confident that the systematic error of the simulation is about -30%–$+10\%$ within $\theta \sim 80'$, where effective CXB photons come from. As can be seen in figure 4.12, the stray light pattern also has a good 90° symmetry within a deviation up to a few arcmin. From these investigations, we conclude that the current ray-tracing program has a sufficient accuracy and reliability in quantifying the stray light effects upon the CXB analysis.

Table 4.5: Log of the Crab stray observations

Date		Exposure	GIS2		GIS3	
yy/mm/dd	START – END	(sec)	θ	ϕ	θ	ϕ
93/04/06	07:38 – 00:55	13,261	57.6′	47.3°	61.5′	44.5°
95/09/29	17:57 – 21:31	5,346	64.0′	222.4°	60.0′	225.0°
95/09/29	03:36 – 06:44	5,462	63.1′	138.3°	60.1′	134.8°
95/09/30	02:11 – 06:30	2,206	21.4′	219.9°	17.0′	228.0°
95/09/28	22:51 – 03:34	8,110	33.8′	220.0°	29.8′	224.9°
95/09/28	18:21 – 22:50	6,354	48.8′	221.1°	44.8′	224.5°
95/09/28	06:46 – 12:52	8,777	83.7′	223.0°	79.7′	224.9°
95/09/29	21:32 – 02:10	9,476	103.8′	223.3°	99.9′	224.9°

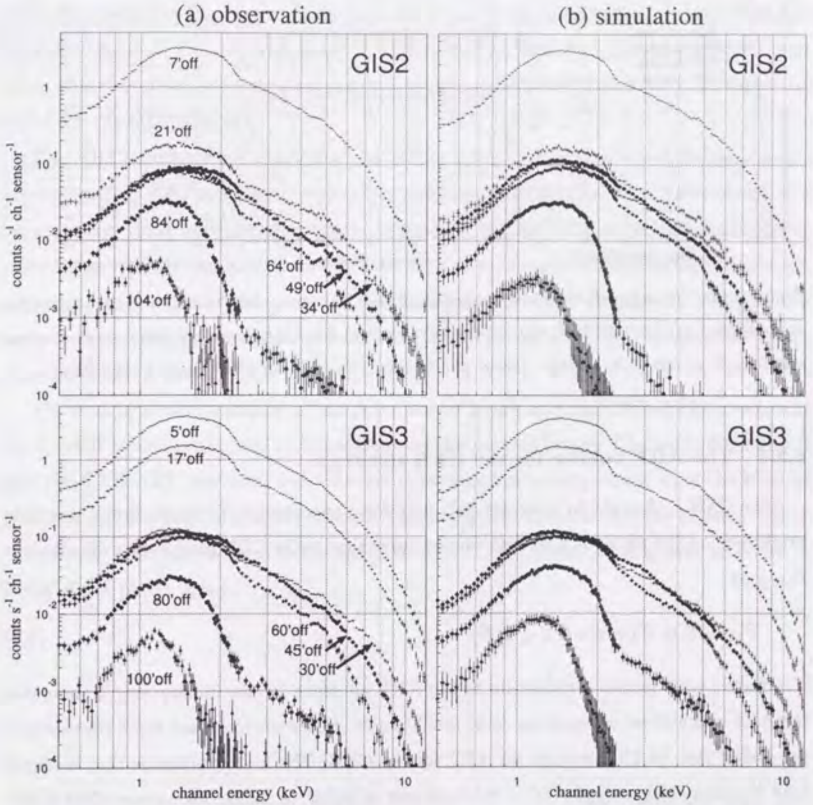

Figure 4.16: (a) Spectra of the Crab stray observations taken by GIS2 (upper panel) and GIS3 (lower panel) integrated in the radius of 20 mm from the optical axis of each sensor. The Crab has been placed at various offset angles as specified in the figure. The CXB+RNXB spectra are subtracted after dead time correction. (b) Simulated spectra of the Crab stray observations. The Crab nebula is assumed to have an absorbed power-law spectrum of $\Gamma = 2.10$, $N_{\rm H} = 3.0 \times 10^{21}$ cm^{-2}, and the power-law normalization of 9.7 c s^{-1} cm^{-2} keV^{-1} at 1.0 keV.

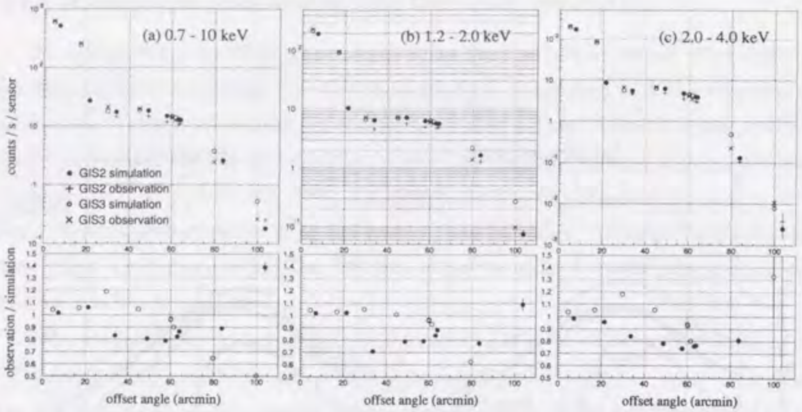

Figure 4.17: Upper panels show counting rates of the Crab stray observations and the ray-tracing simulations in (a) 0.7–10 keV, (b) 1.2–2.0 keV, and (c) 2.0–4.0 keV energy band, plotted versus offset angle of the Crab nebula. Lower panels show the ratios of observation to simulation.

4.3.4 The ARF builder for the CXB spectrum

The CXB is thought to have not only a uniform spectrum but also an almost constant brightness on the whole sky, so that we can approximate the CXB photon flux distribution F_{CXB} as

$$F_{CXB}(\theta, \phi, E) = \cos\theta \; S_{CXB}(E). \tag{4.9}$$

The factor $\cos\theta$ means a reduction of the XRT aperture by the inclination. This makes the ARF calculation of equation (4.6) much easier. However, there are some problems to use jbldarf (ref. §4.2.1) to make an ARF for the CXB. The first problem is that we must take the stray light effects (§4.3) into account in order to make the correct CXB ARF. However the pre-calculated XRT tables for the effective area and the PSF are both defined only in the range of $\theta < 20'$, i.e. within the nominal f.o.v., which is totally insufficient to consider the stray lights. The second problem is that, even if there were tables covering $\theta > 20'$, it would take unrealistically huge time or CPU power to integrate over the whole sky where effective CXB photons come from.

To solve these issues, we make use of an ASCA simulator called SimASCA, developped mainly by M. Hirayama, Y. Ogasaka, T. Kotani, and Y. Ishisaki. Instead of conducting the numerical integration of equation (4.4), we generate a number of Monte-Carlo photons of energy E, according to the surface brightness distribution $B(\theta, \phi)$, we run XRT+GIS simulator, and we count how many photons come into the integration area on the detector plane. Here, we denote the number of the Monte-Carlo photons which has been generated N_{gen}, the number of photons detected N_{detect}, and the geometrical aperture of the XRT D_{XRT}. Then, $D_{XRT} \times \frac{N_{detect}}{N_{gen}}$ gives the expected value of $A_{XRT+GIS}(E)$ in equation (4.4). The Monte-Carlo error Δ of this value is expected to be $\frac{\Delta}{A_{XRT+GIS}(E)} = \sqrt{\frac{N_{gen} - N_{detect}}{N_{gen} \cdot N_{detect}}}$. We continue generating the Monte-Carlo photons of energy E, until this error ratio becomes typically less than 2%. M. Hirayama, H. Honda and R. Shibata have developped a code doing this procedure, and they named it SimARF. The SimARF has been modified and tuned for the CXB analysis.

The XRT simulator is the key module for the CXB ARF. We selected the ray-tracing program as the XRT simulator, which can take into account the stray light effects in a natural way. This ray-tracing program is released by the XRT team and also used to make the pre-calculated XRT tables for the effective area and the PSF shown in table 4.3, although the version of the program is somewhat different. As seen in the previous section, the ray-tracing program has sufficient accuracy and reliability in quantifying the stray light effects on the CXB analysis.

Figure 4.18 shows examples of the point source ARFs and the CXB ARFs created by the SimARF which is adopted in the analysis of the present thesis. The main difference is that the CXB ARF has much less effective area in higher energy bands than the ARF at 1CCD nominal position, because of both vignetting and the soft spectra of stray lights. About 40% difference is seen in the range of 0.6–10 keV, which corresponds to ~ 0.2 in terms of the phton index.

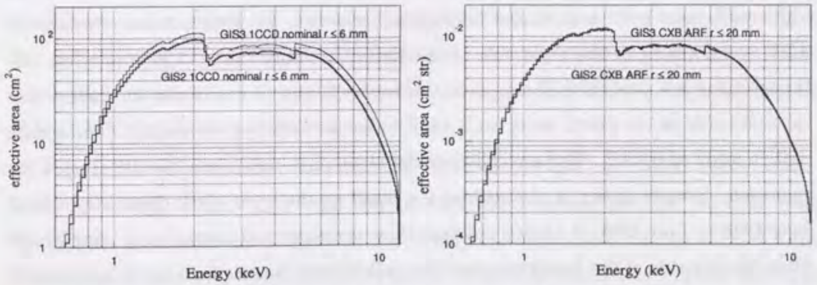

Figure 4.18: Plot of the ARFs for GIS2 (thick line) and GIS3 (thin line). Left panel shows the point source ARFs at 1CCD nominal position with integration radius 6 mm. Right panel shows the CXB ARFs with integration radius 20 mm from the optical axis.

4.4 Residual non X-ray background (RNXB) of the GIS

4.4.1 Importance of RNXB in the CXB analyses

To begin with, we define RNXB (residual non X-ray background) to mean false events of non X-ray origin (mainly charged particles and γ-rays), which survived standard background rejection process described in §3.4.3, and appear in the GIS main data. All data shown in this section are already cleaned with *RT* discrimination (RTD), *SP* discrimination, and strict *RT* mask.

In the usual analysis of a point source data, we subtract CXB+RNXB as a background, whereas only RNXB should be subtracted in the analysis of the CXB itself. Therefore, more carefull RNXB estimation is required for the CXB analyses. Particularly, we need to make full use of the detector area to get a CXB spectrum of good statistics. As a result, fraction of the RNXB counts also increases. When we choose an integration radius of 20 mm, the RNXB counts are abount 32% of the pure CXB counts in the 0.6–10 keV energy band. Furthermore, as seen in figure 4.14b, the RNXB counts exceeds the CXB counts above $\sim$ 5 keV.

As described in §3.4.3, the GIS is equipped with various mechanims to reject background events efficiently, and the GIS thus has realized very low background level of 0.044–0.086 c s^{-1} $sensor^{-1}$ (table 3.4). Properties of RNXB is also well investigated so far (Kubo 1993; Kubo et al. 1994 in ASCA News No.2). We briefly introduce the results in §4.4.2, explain how to restrain/monitor the time variation of RNXB in §4.4.3, and test the RNXB reproducibility in §4.4.4.

4.4.2 Rough properties of RNXB

We cannot distinguish RNXB from the real X-ray events. Therefore, we utilize the night-earth data surviving the full background rejection, i.e. events obtained when the XRT was pointing to the night-side of the Earth, to study the RNXB properties. Although there is a possibility of oxygen line or harder X-rays from auroras, we assume that the night-side of the Earth emits no X-rays; hence we believe that the night-earth data consist solely of RNXB. We have collected the night-earth data since the GIS started the operation. Results shown in this section are based on the night-earth observations from June 1993 to June 1995. It turned out that there are some contamination of solar X-rays when the day-side of the Earth are partially visible from the satellite even if it is outside the GIS f.o.v. Therefore, we adopted the selection condition that

target elevation from the rim of the Earth $\leq -5°$

.AND.

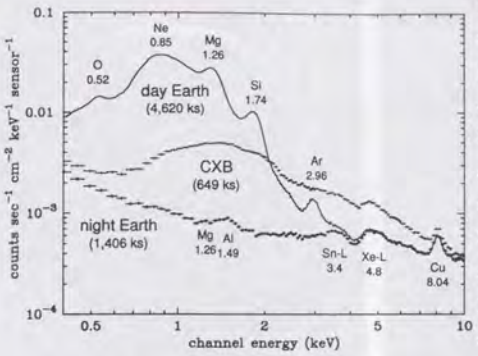

Figure 4.19: Integrated spectra of the day-earth (smooth line), the CXB (crosses), and the night-earth (filled circles) observations taken by the GIS2+3 on the whole detector area as shown in figure 4.20. Each of exposure time is given in the parentheses. The CXB and the day-earth spectra contains RNXB. Possible origin of the line feature with the energy in keV are also given in the figure. The flare-cut (table 4.6) is NOT applied.

sun height from the rim of the Earth $\leq -5°$.

Integration time of the resultant data amounts to 1,400 ks.

Figure 4.19 shows the average night-earth spectrum, presented together with the day-earth and the CXB spectra. The unit of cm^2 in the count rate unit refers to the detector area, not to the XRT area. Thus the in orbit RNXB level is about 1×10^{-3} c s^{-1} cm^{-2} keV^{-1} below 1 keV, and $(4\text{–}7)\times 10^{-4}$ c s^{-1} cm^{-2} keV^{-1} above 1.5 keV. This is 2-3 times larger than that measured on ground. The night-earth spectrum exhibits several instrumental features, including Cu-K line (from copper-plated molybdenum support grid; 8.04 keV), a hump around 5 keV due to Xe-L eges (from the detection gas; 4.78 keV, etc), Sn-L line (from the tin-plated stainless support mesh; 3.44 keV), a possible blend of Mg-K (from the GIS case made of Mg-alloy; 1.26 keV) and Al-K (not yet determined; 1.49 keV) lines. All these lines and edges arise from materials used in the GIS. The day-earth spectrum consist of RNXB and solar X-rays scattered off the atomosphere. Error bars are omitted because of the extensively high statistics. Mg-K and Si-K lines are of solar origin (ionized species), while the Ar-K line (neutral) is due to atomspheric fluorescence. A close agreement of the night-earth and the day-earth spectra above 5 keV visualizes the RNXB stability.

Figure 4.20 shows images for GIS2 and GIS3 during the night-earth observations. There are several regions where the residual night-earth counts are high, such as lower rim of GIS2 and upper rim of GIS3. It is probably due to to the incompleteness of SPD. There is also a little spill of the calibration source around the masked-out regions, although its level is negligible. Except such local inhomogeneities, the residual night-earth counts increase at the outer region of the detector in general. This trend is more significant below 1 keV, as shown in figure 4.21. However, inside about 10 mm from the detector center,

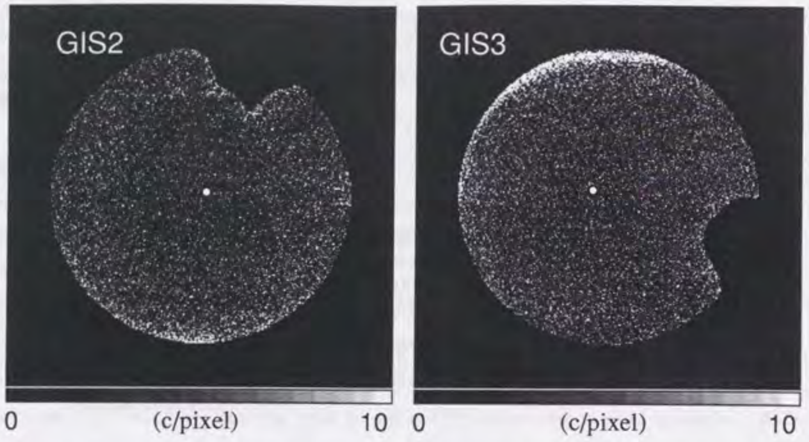

Figure 4.20: Integrated images taken by GIS2 (left panel) and GIS3 (right panel) for the entire night-earth observations with exposure time of 1,202 ks in the 0.6–10 keV energy band. The white spot in the figure shows the optical axis of each detector. Both images are masked by the standard image masking, i.e. selection of $r \leq 25$ mm from the detector center and elimination of the calibration isotope. The flare-cut (table 4.6) is applied.

the residual night-earth data show fairly constant spectra and intensity as a function of the detector position. Therefore, we may presume that there are approximately two RNXB components; (1) a "hard component", which has a flat spectral shape and an almost constant intensity over the whole detector area, and (2) a "soft component", which rises below 1 keV and significantly increases towards the detector rim. In contrast, the CXB intensity is the strongest at the optical axis of the XRT because of the vignetting effect. The CXB intensity at $\theta = 20'$ is roughly half the on-axis CXB intensity. Therefore influence of RNXB gets much severer towards the detector rim, because of both vignetting and the RNXB profile, as shown in figure 4.22. Irregularities of $\sim$ 5 mm step seen in the CXB counts are shadows of the window support grids.

Time variation of RNXB is predominantly correlated with geomagnetic cutoff regidity (COR) for cosmic rays along the satellite orbit. COR defines the minimum momentum of charged particles that can penetrate against electro-magnetic force due to terrestrial magnetism. When cosmic rays (charged particles) run across the Xe gas, gas creates long electron track along the path. Most of these events can be rejected by RTD. Electrons ejected from the ceramic wall of the gas cell struck by cosmic rays are also a candidate of background events. It is probably the origin of the *soft* component of RNXB, and these events can be rejected by RTD or SPD for the most part. Cosmic rays also generate high energy γ-rays reacting with the satellite body or the atmosphere. Compton-scattered electrons by γ-rays especially in the drift region of the gas cell is rather hard to eliminate. Figure 4.23 shows a correlation between COR and $LDHIT$ during the night-earth observations. $LDHIT$ increases as COR gets lower. Especially, the correlation gets steeper below $COR \sim 6$ GeV/c. There is also a branch in the $LDHIT$-COR correlation for $COR \leq 10$ GeV/c, as well as a large scatter around $COR \sim$ 11–12 GeV/c. These two phenomena will be discussed in §4.4.3.

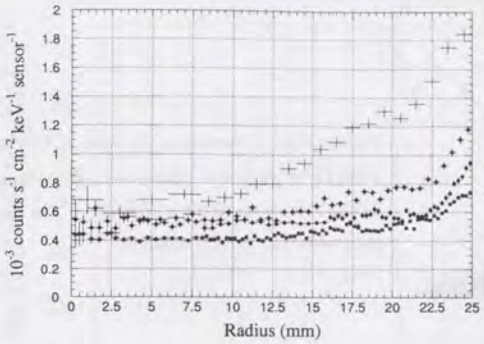

Figure 4.21: Energy sorted radial profiles of the GIS counts during the night-earth observations. GIS2 and GIS3 data are summed up. The mark of '+' shows 0.6–1.0 keV, 'o' 1.0–2.0 keV, '•' 2.0–4.0 keV, and '×' 4.0–8.0 keV. The flare-cut (table 4.6) is applied.

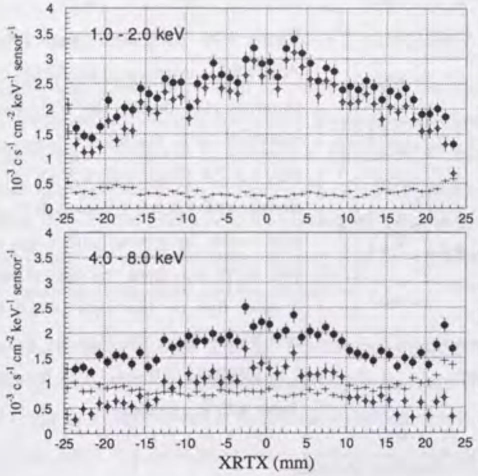

Figure 4.22: Band profiles during the CXB and night-earth observations in -5 mm $\leq$ XRTY $\leq$ $+5$ mm for GIS2. Upper panel shows a profile in the 1–2 keV energy band, and lower panel 4–8 keV. The origin of the coordinates for $XRTX$-$XRTY$ is the optical axis. Filled circles, crosses, and diamonds represents the raw CXB including RNXB, the residual night-earth, and the CXB after subtracting the residual night-earth, respectively. The flare-cut (table 4.6) is applied for both the CXB and the residual night-earth data.

A long-term RNXB increase by $\sim$ 10% in two years has been seen, as shown in figure 4.24. Although the spectral shape has not changed significantly, it is probably caused by a slight build-up of long-term decay elements.

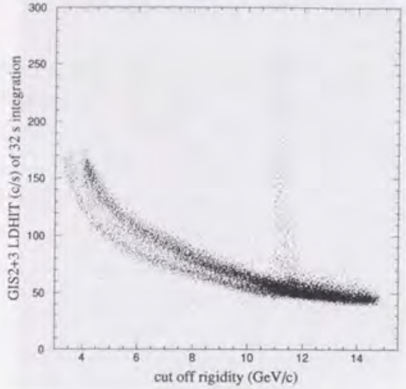

Figure 4.23: Correlation between *COR* and *LDHIT* during the night-earth observations. *LDHIT* is integrated for every 32 s. The flare-cut (table 4.6) is NOT applied

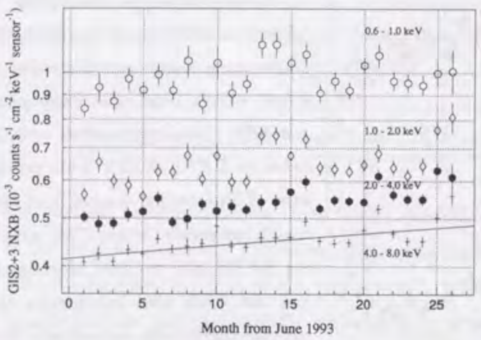

Figure 4.24: Long term (June 1993 – June 1995) variations of the GIS2+GIS3 counting rate during the night-earth observations in the 0.6–1.0 (open circle), 1.0–2.0 (diamond), 2.0–4.0 (filled circle), and 4.0–8.0 (crosses) keV energy bands, integrated within the radius of 20 mm from the optical axis. A solid line on the data of 4.0–8.0 keV band shows the best fit line of $y = 0.00257x + 0.414$. The flare-cut (table 4.6) is applied.

4.4.3 Flare events and the GIS monitor counts

Although *COR* is a good indicator of RNXB, there exists a secondary branch below $COR \sim 10$ GeV/c on the *COR* vs. *LDHIT* correlation, as shown in figure 4.23. This is probably due to a slight inaccuracy of the *COR*-map. If we plot the satellite positions on the Earth, those periods which fall on the secondary branch appear only at the north east region of the map above the north Atlantic Ocean (dots in figure 4.25). Since the *COR*-map which we use does not refer to the satellite height, this discrepancy may change in future when the satellite altitude decreases. Moreover, *COR* is merely one of many factors that affect RNXB.

Therefore, we have decided to utilize the GIS monitor counts to estimate RNXB. Among nine GIS monitor counts described in §3.4.4, we selected $H0$ and $H2$ as the RNXB indicator, because they are almost free from signal X-rays in the f.o.v., even during the on-source observations. $H0$ and $H2$ have adequate statistics of 10–30 c s^{-1} $sensor^{-1}$ when they are summed up. Since GIS2 and GIS3 show similar variations, we also sum the counts of GIS2 and GIS3 in order to reduce statistical errors. Hereafter, we call this summed up counts $H02$. Figure 4.26 shows a correlation between *COR* and $H02$, which has almost the same distribution as *COR* vs. *LDHIT* (figure 4.23). As shown in figure 4.27, $H02$ and *COR* also correlate well to the residual night-earth counts within $r = 17$ mm (here after *RNTE*). However, there are two more issues on these correlations.

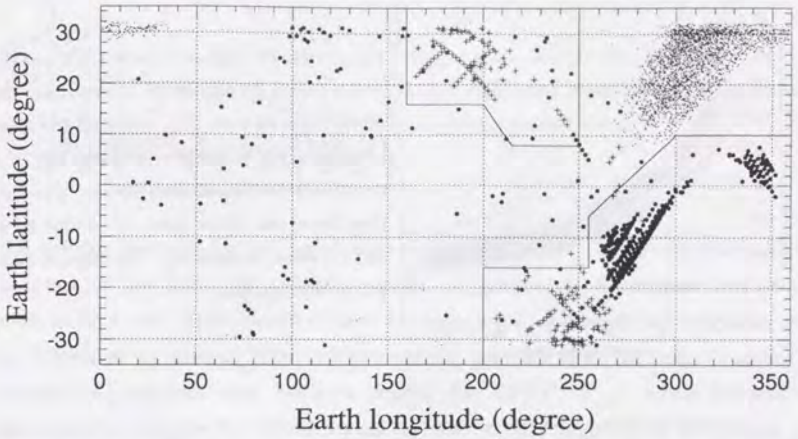

Figure 4.25: Distribution map for three types of phenomena on the Earth surface. The mark "·" represents a position when $H02$ is less than the lower solid line in figure 4.26, where the *COR*-map is thought to be inaccurate. The mark "•" represents a position when $H02$ is greater than the upper solid line in figure 4.26 (the hard-flares). The mark "+" represents a position when $H02 < 1000$ c/32 s = 31.25 c/s and $RNTE > 15$ c/32 s = 0.46875 c/s in figure 4.27a (the soft-flares). Two regions surrounded by solid lines define the dangerous areas where we should be cautious of the hard- and the soft-flares.

The first problem is a large scatter around $COR \sim 11$–20 GeV/c in the *COR* vs. $H02$ plot, which is also seen in *COR* vs. *RNTE* (figure 4.27b). We call the phenomanon which causes the scatter "hard-flares". If we plot the satellite positions on the Earth, the hard-flare periods are concentrated in the region peripheral to the south Atlantic anomaly (SAA) (filled circles in figure 4.25). SAA is a *hole* in the geomagnetic field which allows particles trapped in the magnetosphere to come down than usual. It is located up in the sky around Brazil, where protons of $E < 100$ MeV are confined by terrestrial magnetic fields. The particle background in SAA is extremely high, so that the high voltage of the GIS is turned off in SAA. The hard-flares are probably caused

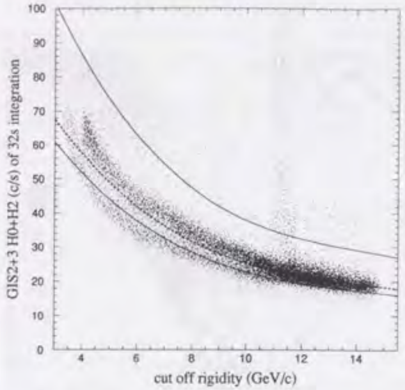

Figure 4.26: Correlation between COR and $H02$ counts during the night-earth observations. $H02$ is integrated for every 32 s. A dashed line means a function $f(x) = (109.3 - 17.05x + 1.127x^2 - 0.02627x^3)/32$ derived from fitting. Two solid lines below and above show $f(x)$ scaled by 0.9 and 1.5 times, respectively. The flare-cut (table 4.6) is NOT applied.

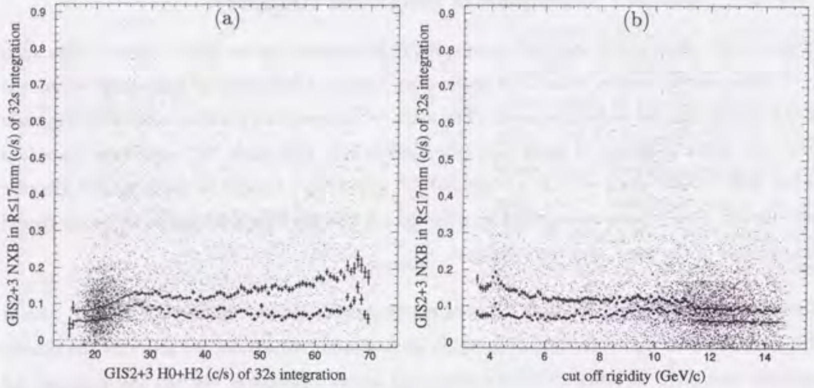

Figure 4.27: (a) A correlation between $H02$ and $RNTE$, and (b) a correlation between COR and $RNTE$. $H02$ and $RNTE$ are integrated for every 32 s. $RNTE$ is integrated in $r \leq 17$ mm in the 0.3–11 keV energy band. Crosses superposed on the figure show averages (upper) and standard deviations (lower) in each $H02$ or COR bins. The flare-cut (table 4.6) is NOT applied.

by particles trapped in SAA. These events can be eliminated by rejecting time intervals when $H02 > 1.5 \times f(COR)$ in figure 4.26.

After eliminating the hard-flares, does $RNTE$ well correlate with $H02$? In fact, there is the second issue, i.e. the component which scatters upwards around $H02 \sim 20$–40 in figure 4.27a. We call the phenomenon which cause the scatter "soft-flares". During the soft-flares, the RNXB counts increase without an increase of $H02$. They are more dangerous than the hard-flares, because they cause mis-estimation of the RNXB counts, and furthermore, the spectrum during the soft-flares show acutually harder profile than

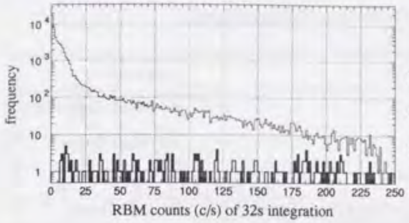

Figure 4.28: $RBMCNT$ distribution for the entire night-earth observations (thin solid line) and during the soft-flares.

the average spectrum for the entire night-earth observations. If we plot the satellite positions on the Earth, the soft-flare periods concentrated in two regions: the south west to SAA and above Hawaii (crosses in figure 4.25). Although the soft-flares can be eliminated by masking these regions, masking area is a little too large to ignore a decrease of integration time. We have founded that $RBMCNT$, i.e. a counting rate of the radiation belt monitor (RBM; ref. §3.4.1), can reject the soft-flares efficiently. As shown in figure 4.28, $RBMCNT$ distribution during the soft-flares (thick line) is almost flat, in contrast to the distribution for the entire night-earth observations (thin line) which is concentrating towards $RBMCNT < 25$ c/s. Therefore we reject the time intervals when $RBMCNT > 300$ c/16 s $= 18.75$ c/s everywhere, and especially $RBMCNT > 100$ c/16 s $= 6.25$ c/s in the dangerous areas (solid line in figure 4.25). The frequency of the soft-flares have a slight correlation with the angle θ_{mag} of the terrestrial magnetic field to the XRT direction. The soft-flares seem to happen more frequently when $\theta_{mag} \sim 60$–120°. It is possible that the physical origin of the soft-flares is electrons which come into the GIS from the direction of the XRT.

From these investigations, we have arrived at the conditions to reject the hard- and soft-flares as summarized in table 4.6. To avoid high RNXB periods, we usually restrict $H02$ in the range of 15–45 c/s, too. We call the procedure to apply these conditions "flare-cut". Correlations between $H02$ vs. $RNTE$ and between COR vs. $RNTE$ after the full flare-cut are shown in figure 4.29. Compared with figure 4.27, the humps around $H02 \sim 20$–40 and $COR \sim 10$–12 have almost disappeared. The standard deviation of $RNTE$ in each bin are approximately equal to the square root of the average $RNTE$ of that bin, which means the Poisson statistics. Note that we must multiply 32 s to convert counting rate (c/s) to the original counts. This means that the RNXB counts can be successfully estimated by $H02$.

4.4.4 RNXB reproducibility by H02-sorting method

To generate an RNXB spectrum or image to be subtracted from the raw CXB data which includes RNXB, we integrate the night-earth data which are screened on the same

Table 4.6: Summary of the flare-cut conditions

Condition	Reason
15 c/s $\leq$ H02 $\leq$ 45 c/s	to avoid high NXB
H02 $\leq 1.5 \times f(\mathrm{COR})^{\dagger}$ c/s	for hard flares
RBM $\leq$ 300 c/16 s = 18.75 c/s everywhere	for soft flares
RBM $\leq$ 100 c/16 s = 6.25 c/s in the dangerous areas (figure 4.25)	for soft flares

† $f(x) = 0.5(109.3 - 17.05x + 1.127x^2 - 0.02627x^3)$ c/ 16 s.

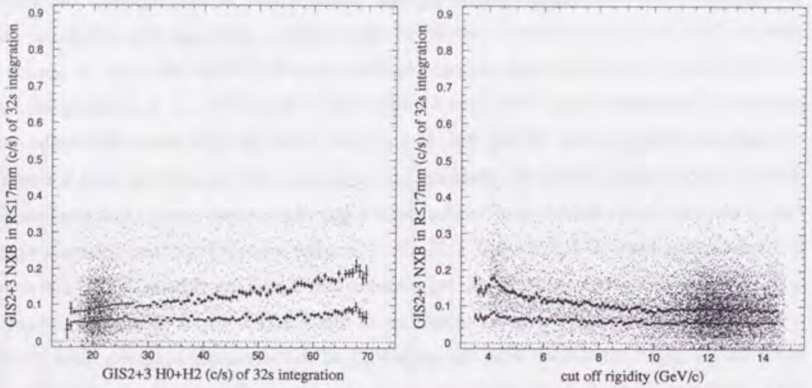

Figure 4.29: Almost the same as figure 4.27 except that the flare-cut (table 4.6) is applied.

conditions as the raw CXB events, at the same detector region (for a spectrum) or in the same energy band (for an image). However, the RNXB counts can vary by ~ 40% in the range of $COR > 6$ GeV/c (figure 4.29). If the exposure time is long, this variation is averaged to a reasonable level of ~ 10% depending on the length of the observation, but it will be better to take into account the RNXB variation by some methods. As seen in §4.4.3, $H02$ can be a good indicator of RNXB. Thus we choose $H02$ to predict the RNXB variation. In the next paragraph, we explain how to generate the expected RNXB spectrum for a specified on-source observation.

We sort the residual night-earth data by $H02$ in every 5 c/s step, i.e. 15–20 c/s, 20–25 c/s, 25–30 c/s, etc. $H02$ is counted in the 16 s time interval including the arrival time when the corresponding event is detected. Figure 4.30 shows the residual night-earth spectra and radial profiles corresponding to five $H02$ intervals. As $H02$ increases, the spectrum gets softer and the slope of the radial profile gets steeper towards the detector rim. It is probably due to the increase of the *soft* component of RNXB described in §4.4.2. We usually restrict $H02$ to the range of 15–45 c/s, where the influence of the *soft* component is not severe. Figure 4.31 shows exposure time out of the entire night-earth observations when $H02$ is in the range of each X-axis bin. We denote each exposure time T_i^{NTE}, and each spectrum $H_i^{NTE}(PI)$, both of which are counted or created on the same condition and in the same detector region as the on-source observations. When T_i^{OBS} is the exposure time in the i-th $H02$ bin during the on-source observation, the RNXB spectrum contained in the on-source data is estimated as:

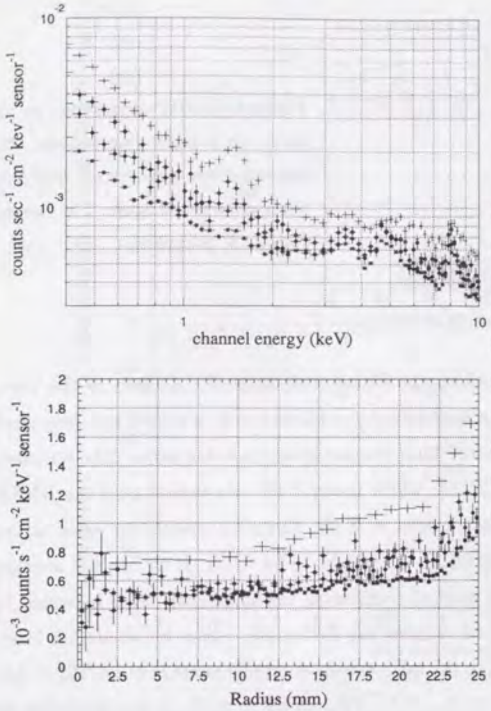

Figure 4.30: $H02$ sorted spectra (upper panel) and radial profiles (lower panel) of the GIS counts during the night-earth observations in the 0.6–7.0 keV energy band. The mark '+' represents the data when $H02$ is in the range 50–80 c/s, 'o' 40–45 c/s, '•' 30–35 c/s, and '×' 20–25 c/s. $H02$ are integrated for every 16 s. The flare-cut (table 4.6) is applied.

$$H(PI) = \sum_i H_i^{NTE}(PI)\,\frac{T_i^{OBS}}{T_i^{NTE}}. \tag{4.10}$$

We call this method "H02-sorting method".

To check the reproducibility of RNXB by the H02-sorting method, we splitted the entire night-earth data into 122 × 10 ks intervals. Then we compared the counting rate of each interval with that estimated by H02-sorting method using the entire night-earth data. The results are shown in figure 4.32. Crosses in the upper panel show the actual counting rate of each interval, and the histogram show the prediction. It seems that 10 ks-integrated $RNTE$ varies more than the prediction. There is a general trend of increasing counting rate with time, which means that the long-term RNXB increase which is seen

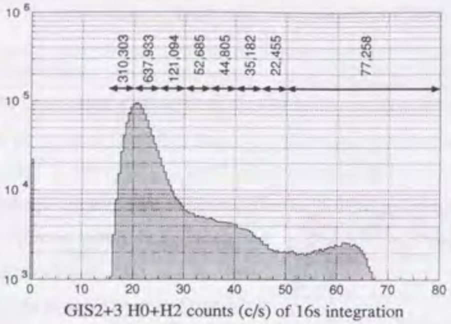

Figure 4.31: *H*02 distribution for the entire night-earth observations. Net exposure time (sec) in each *H*02 5 c/s bin is given in the figure. The flare-cut (table 4.6) is applied.

in figure 4.24 cannot be reproduced by the H02-sorting mothod. As seen in the lower panel of figure 4.32, the mean value of observed / predicted ratio is 0.9983 and very close to 1.0, which is rather natural because their mother groups are the same. The standard deviation of the distribution is 0.07429, which mean 7.4% rms variation of the RNXB counts. This value includes a Poission error of 3.4%; therefore, systematic error of the H02-sorting method for 10 ks observation is thought to be 6.7%. If we use the average $RNTE$ instead of the H02-sorting method prediction, the systematic error increases to 7.8%. Thus the H02-sorting method reduces the systematic errors by about 1% level. Since the χ^2/d.o.f of the line fitted to the ratio shown in middle panel is $412.4/121 = 3.4$, the systematic error will be reduced to $\sqrt{3.4 - 1.0} \times 3.4\% = 5.2\%$, if the prediction of H02-sorting method are corrected for the long-term trend.

This long-term RNXB increase of ~ 15% in two years can be a serious problem in the CXB analyses. No compensation of this long-term trend results in the ~ 0.1 difference of the CXB photon index between two observations at intervals of two years (ref. §6.4.1). We, therefore, decided to adjust the normalization of the RNXB image or spectrum estimated by the H02-sorting method with the formula:

$$scaling\ factor = 0.9983 + 2.1255 \times 10^{-9} \cdot (ascatime - 45878400) \tag{4.11}$$

where *ascatime* represents the time in second from 00:00:00 (UT) on 1 January 1993, and is calculated from the mean observation time.

The systematic errors described above are summarized in table 4.7. We conclude that we can achieve a ~ 3.5% rms reproducibility in RNXB, by a combined use of the standard background rejection, the flare-cut procedure, the H02-sorting method, and the long-term RNXB trend correction. In the following, we quote 3.5% (rms) as a typical systematic uncertainty associated with the RNXB estimation.

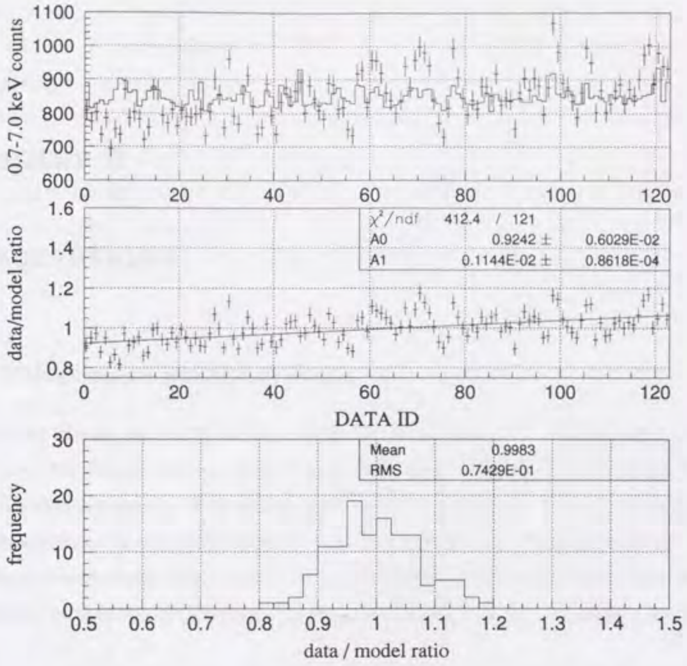

Figure 4.32: Figures to check the RNXB reproducibility by H02-sorting method. Upper panel shows the actual $RNTE$ (crosses) and the H02-sorting method prediction (solid line), in the 0.7–7.0 keV energy band, for every 10 ks exposure. Middle panel shows ratios of the $RNTE$ to the prediction. The solid line shows the best fit line, and fitting results are indicated in the figure inset. Lower panel shows a distribution of the ratios. The mean value and the standard deviation for the distribution are indicated in the inset.

Table 4.7: Systematic errors of the RNXB counts in the 0.7–7.0 keV energy band

data screening condition	RNXB generating method	0.7–7 keV† counting rate (c s^{-1} cm^{-2} keV^{-1})	drop‡ of data	Exposure time 10 ks	Exposure time 40 ks
$COR \geq 6$ GeV/c	average $RNTE$	4.01×10^{-4}	92%	16%	14%
flare-cut	average $RNTE$	3.59×10^{-4}	74%	7.8%	5.6%
flare-cut	H02-sorting method	3.59×10^{-4}	74%	6.7%	5.3%
flare-cut	+ long-term correction	3.59×10^{-4}	74%	5.3%	3.4%

† Average $RNTE$ in the 0.7–7 keV energy band within the radius of 20 mm from the optical axis

‡ Reduction rate of exposure time to the entire night-earth observations